The causes and consequences of large scale ash aggregation

Sebastian Müller

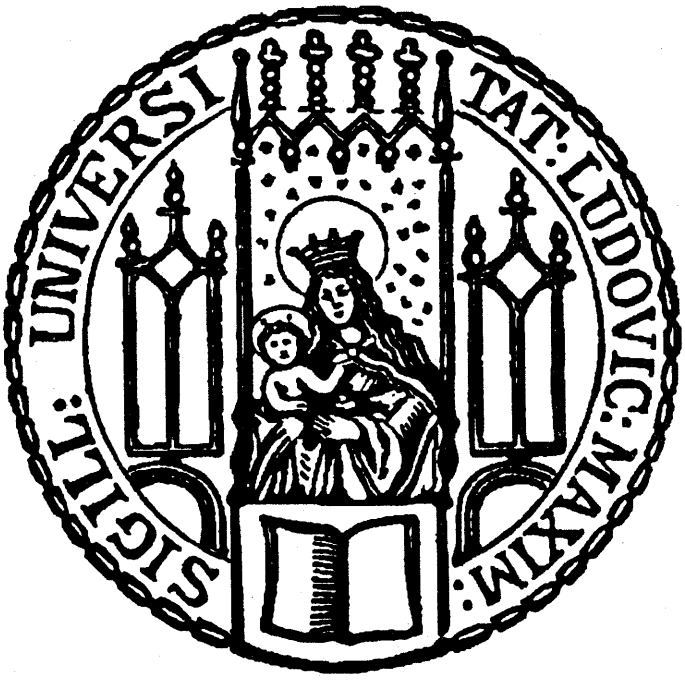

München, 2017

The causes and consequences of large scale ash aggregation

Sebastian Müller

Dissertation zur Erlangung des Doktorgrades

an der Fakultät für Geowissenschaften

der Ludwig-Maximilians-Universität

München

vorgelegt von

Sebastian Müller

aus München (Deutschland)

München, den 07.02.2017

Erstgutachter: Prof. Dr. Donald B. Dingwell

Zweitgutachter: Dr. Jonathan Merrison

Berichterstatter: Prof. Guntram Jordan

Antrag auf Zulassung zum Promotionsverfahren gestellt: 07.02.2017

Tag der mündlichen Prüfung: 17.05.2017

It is not about the time in your life – it is about the life in your time!

Bruce Springsteen

Kurzfassung

Die Oberfläche unseres Planeten Erde wird, ähnlich wie bei anderen terrestrischen Planeten unseres Sonnensystems, zu einem signifikanten Teil durch vulkanische Prozesse geformt. Aufsteigende Gesteinsschmelze (Magma), gebildet im Bereich des oberen Erdmantels und der unteren Erdkruste (Tiefe von bis zu wenigen 100 km), dringt aufgrund ihrer geringeren spezifischen Dichte an die Erdoberfläche und mündet in einem Vulkanausbruch. Hierbei lassen sich zwei grundlegend verschiedene Ausbruchsarten unterscheiden: explosiv und effusiv. Entscheidende Parameter stellen hierbei vor allem die chemische Zusammensetzung des Magmas dar (Gasgehalt, Viskosität und Feststoffanteil wie Kristalle). Diese kennzeichnenden Eigenschaften entscheiden, wie schnell Magma sich verformen, d.h. auf externen und internen Druck reagieren kann. Bei zu starker Deformationsrate fragmentiert Magma und kommt als pyroklastisches Auswurfsmaterial zu Tage (explosiv). Pyroklasten unterteilt man je nach Korngröße in Asche (< 2 mm), Lapilli (2-64 mm) und Bomben (> 64 mm).

Vulkanasche hat atmosphärische Verweilzeiten, die von Tagen bis Monaten reichen, und kann sich durch Windzirkulationssysteme kontinental oder auch global ausbreiten. Insbesondere vulkanische Asche birgt aufgrund ihrer physikalischen, chemischen und mechanischen Eigenschaften mehrere potenzielle Gefahren für Mensch und Umwelt. Dies sind beispielsweise: (1) Aschepartikel können in die Atemwege eindringen und diese beschädigen, (2) toxische Elemente wie Fluor oder Chlor können von der Ascheoberfläche gelöst werden und in die Wasserversorgung eintreten, (3) kritische Infrastrukturobjekte wie Stromleitungen können unter der Last der abgelagerten Asche zusammenbrechen oder (4) Asche kann in Flugzeugturbinen eindringen und diese zum Überhitzen und Totalausfall bringen. Um humanitäre und finanzielle Schäden möglichst gering zu halten oder gar zu verhindern, gibt es mehrere Strategien. Eine ist das das Modellieren der Verbreitung von Aschewolken in der Atmosphäre nach einem explosiven Vulkanausbruch. Anhand dieser Modelle lässt sich vorhersagen, wann und wo mit wie viel Vulkanasche gerechnet werden kann.

Ein Unsicherheitsfaktor bei der Modellierung von der Ausbreitung von Aschewolken liegt in der potenziellen Aggregation und Disaggregation von Vulkanasche. Einzelne Aschepartikel können sich in der Atmosphäre aufgrund von hydrostatischen oder elektrostatischen Kräften zu einem Verbund zusammenfinden (Aggregation), und fallen aufgrund geänderter aerodynamischer Eigenschaften (höhere Masse) schneller aus der Atmosphäre als einzelne, nicht aggregierte Partikel (Primärpartikel). Jedoch können Aggregate durch Kollisionen mit anderen Partikeln auch wieder aufbrechen (Disaggregation) und folglich die primären Einzelpartikel in der Atmosphäre verweilen. Ein Beispiel für die Schwierigkeiten bei der Vorhersage der Ausbreitung von Aschewolken, beeinflusst durch Aggregation, ist der

Ausbruch der Vulkangruppe Eyjafjallajökull auf Island im Frühjahr 2010. Die tatsächliche Aschebelastung des europäischen Luftraumes war flächenmäßig weitaus geringer als vorhergesagt wurde und der durch unnötige Luftraumsperrungen entstandene finanzielle Schaden für die Luftfahrtindustrie von rund 10 Mrd. € (Munich Re Versicherungsgruppe) hätte erheblich geringer ausfallen können. Hierbei (2010) war die Nichtberücksichtigung von Ascheaggregation ein wichtiger Faktor, der zu einer Fehlvorhersage der Ascheausbreitung führte.

Forschungsarbeiten über Ascheaggregation in den letzten Jahren, insbesondere seit dem Ausbruch des Eyjafjallajökull in 2010, führen zu einer stetigen Verbesserung der Vorhersagemodelle. Ein erstes, in weiten Ansätzen ganzheitliches numerisches Vorhersagemodell, welches Teilbereiche der Ascheaggregation miteinschließt, wurde im Jahr 2016 vorgestellt. Die Wissenschaftliche Grundlagenarbeit in der vorliegenden Dissertation dient dem Zweck, Ascheaggregation und Disaggregation besser zu verstehen und sie somit intensiver in Vorhersagemodelle einfließen zu lassen. Diese würden dadurch weiter verbessert und akkurater werden.

Experimentelle Studien sind Hauptbestandteil dieser Dissertation und beschäftigen sich mit der Fähigkeit von Partikeln, unter bestimmten Umwelteinflüssen zu aggregieren und somit beschleunigt aus der Atmosphäre auszufallen. Mittels industrieller Granulationstechnologie (Wirbelschichtverfahren) in Kooperation mit *Glatt Ingenieurtechnik GmbH*, Weimar, Deutschland, wird Ascheaggregation im Labor simuliert. Experimentelle Aggregate werden sowohl aus natürlicher Vulkanasche der Laacher See Eruption (Eifel, Deutschland) sowie Kalknatron-Glaskügelchen (Analogmaterial) hergestellt. Als flüssige Bindemittel zur Etablierung der interpartikulären, hydrostatischen Adhäsionskräfte dienen H_2O, HCl und H_2SO_4, welche gleichzeitig die drei am häufigsten auftretenden Gase während Vulkaneruptionen darstellen. Als zusätzliches Feststoffbindemittel werden $CaSO_4$ und NaCl verwendet. Dies sind chemische Verbindungen, die typischerweise auf Vulkanasche und auch in natürlichen Aggregaten nachgewiesen werden. Eine Abhängigkeit der Aggregationseffizienz von relativer Luftfeuchte, Korngröße, Kornmorphologie, Temperatur, Stokes Regime und Reynolds Zahl kann experimentell festgestellt werden. Des Weiteren lassen sich unterschiedliche strukturelle und texturelle Eigenschaften, welche in natürlichen Ascheaggregaten beobachtet werden, unter bestimmten Bedingungen im Labor nachstellen.

Experimentell hergestellte Aggregate werden mit Hilfe von optischen (Mikroskopie), chemischen (Oberflächenauslaugung) und elektronischen (Rasterelektronenmikroskop) Analysemethoden hinsichtlich ihrer chemischen und physikalischen Eigenschaften charakterisiert. Beispielsweise belegen die analytischen Ergebnisse die Fähigkeit von Säuren wie HCl, chemische Verbindungen wie Halite (z.B. NaCl), aber auch umweltschädliche Substanzen wie Fluor aus der Vulkanasche zu lösen und auf ihrer Oberfläche freizusetzen. Die durch chemische Reaktionen entstandenen Salze fungieren weiterhin als Zement für Aggregate und verleihen diesen ihre Stabilität. Salze und andere lösliche Verbindungen

werden in Gegenwart von einem Lösungsmittel wie Wasser als Salz-Wasser-Lösungen über Partikeloberflächen transportiert. Kapillarkräfte ziehen die Salz-Wasser-Lösungen zu den Partikel-Partikel-Kontaktpunkten, an denen sich während eines eventuellen Trocknungsprozesses stabile Salzbrücken bilden. Die Größe dieser Feststoffbrücken ist abhängig vom verfügbaren Salz und ist ausschlaggebend über die Stabilität der Aggregate.

Neben der grundsätzlichen Fragestellung, unter welchen Umständen Aschepartikel aggregieren, ist es auch wichtig, die Disaggregation zu betrachten. Momentan (2017) behandeln numerische Vorhersagemodelle aggregierte Aschepartikel als Material, welches zwangsläufig aus der Atmosphäre ausfällt und sich nicht weiter ausbreiten kann. Jedoch sind Ascheaggregate sehr instabil und können durch Kollisionen mit anderen Partikeln oder Aggregaten wieder in seine Einzelbestandteile (Primärpartikel) aufbrechen. Aufgrund ihrer viel geringeren Masse können die Primärpartikel weiterhin in der Atmosphäre verweilen und werden somit nicht (wie von numerischen Modellen angenommen) abgelagert. Hinsichtlich dieser Problematik wird in dieser Arbeit die Stabilität unterschiedlicher experimenteller Aggregate untersucht. Aggregate mit jeweils verschiedenen Kornmorphologien (irregulär geformte Vulkanasche und sphärische Glaskügelchen), Korngrößen und Salzkonzentrationen (Bindemittel) werden mittels Impaktversuchen zerstört, wobei jeweils die exakte Impaktenergie gemessen wird. Die Versuche zeigen, dass Aggregate mit hoher Salzkonzentration und Korngrößen bis zu 100 µm am stabilsten sind. Die Kornmorphologie zeigt keine signifikante Auswirkung auf die Aggregatstabilität.

Erarbeitete Ergebnisse der experimentellen Studien zu Aggregation und Disaggregation finden letztendlich Anwendung in einer Vergleichsarbeit zwischen vulkanischen, experimentellen und meteoritischen (entstanden durch Impaktereignisse) Aggregaten. Texturelle und strukturelle Gemeinsamkeiten und Unterschiede, deren Bedeutung hinsichtlich der Entstehungsprozesse in der vorliegenden Arbeit erläutert wurde, dienen vor allem der hypothetischen Betrachtung von Aggregation während Impaktereignissen, welche bis heute in der Natur noch nicht beobachtet werden konnten. Insgesamt gibt diese Arbeit den Lebenszyklus eines Ascheaggregates von seiner Entstehung bis hin zur potenziellen Ablagerung oder Zerstörung wieder. Dies erfolgt in experimentellen Maßstäben aber immer in Betrachtung seiner Relevanz zur Natur. Forschungsergebnisse dieser Arbeit stellen einen weiteren Baustein in der Verbesserung der numerischen Aschewolkenvorhersagemodelle dar, vor allem hinsichtlich der Effizienz einzelner Partikel zu aggregieren und der resultierenden Stabilität der Aggregate und ihrem Potenzial abgelagert zu werden.

Extended abstract

As on other terrestrial planets of our solar system, the surface of planet Earth is significantly shaped by volcanic processes. Molten rock (magma)—formed in the Earth's upper mantle and the lower crust (a depth of up to few 100 km)— ascends towards the surface of the Earth due to its lower specific density compared to surrounding rocks. If and when it reaches the surface, this molten rock is discharged by way of a volcanic eruption. Two majorly different eruption types can be distinguished: explosive and effusive. To a large extent, the propensity for one or other of these behaviors is controlled by the chemical composition of the magma (gas content, viscosity and fraction of solids, such as crystals). These characteristic properties control the ability of magma to deform, i.e. to react to internal and external stresses. If the strain rate (i.e. the rate of magma deformation) is sufficiently high, magma can break or fragments, to be erupted as pyroclastic ejecta material. Pyroclasts are subdivided according to their grain size into ash (< 2 mm), lapilli (2-64 mm) and bombs (> 64 mm).

The atmospheric residence times of volcanic ash can range from days to months, and can be distributed across continental or global scales as a consequence of prevailing wind systems. Due to its chemical, physical and mechanical properties, volcanic ash poses several particular threats to human health and the general environment. Volcanic ash hazards include: (1) fine ash particles entering and damaging respiration systems; (2) toxic elements like fluoride or chloride may be dissolved from the ash surface and enter water supply systems; (3) critical infrastructure, such as power lines, may collapse under the weight of the sedimented ash, and (4) ash particles may enter aircraft jet engines and cause failure through overheating. Several mitigation strategies exist in order to minimize or—preferably—avoid human and financial damage. One such strategy is dispersal modeling of ash plumes after an explosive eruption: these models allow the forecast of when and where given amounts of volcanic ash can be expected.

A critical uncertainty inherent in dispersal modeling of ash plumes lies within the potential aggregation and disaggregation of volcanic ash. Due to hydrostatic or electrostatic forces, single ash particles can cluster together to form compounds (aggregates) within the atmosphere; this drastically alters their aerodynamic properties (increased mass) which makes them fall out of the atmosphere faster than non-aggregated particles (primary particles). However, by colliding with other particles, aggregates can break up again (disaggregate) and hence remain in the atmosphere as single, primary particles. One example for the difficulty of forecasting ash plume dispersal, influenced through aggregation, is the spring 2010 Eyjafjallajökull eruption in Iceland. The actual ash concentration in the European airspace was much less than predicted, and financial loss caused to airline industries (10 billion €: Munich RE insurance group) through unnecessary airspace closures could have been much lower. Neglecting ash aggregation throughout this event was a major factor leading to errors in plume dispersal modeling.

In recent years–especially since the 2010 Eyjafjallajökull incident–improved scientific understanding of the parameters governing ash aggregation has led to significant improvement in forecasting models. Indeed, in 2016 a numerical forecasting model was released that represents the most extensive and comprehensive volcanic plume dispersal model to date. Nevertheless, the parameters accounted for by the model are not exhaustive, and it is acknowledged that there remains room for the integration of additional data, especially with respect to ash aggregation and disaggregation mechanisms. Accordingly, the fundamental research presented in this study is intended to provide a more complete understanding of ash aggregation and disaggregation, so as to incorporate these processes more explicitly into forecasting models, in turn improving the accuracy and utility of these models.

Experimental studies comprise the main part of this dissertation, investigating the capacity for particles to aggregate under certain environmental conditions and hence prematurely settle out of the atmosphere. By using industrial granulation technology (fluidized beds) in cooperation with *Glatt Ingenieurtechnik GmbH*, Weimar, Germany, ash aggregation is mimicked in the laboratory. Experimental aggregates are produced using both natural volcanic ash from the Laacher See eruption (Eifel Volcanic Field, Germany) and soda-lime glass beads (analogue material). H_2O, HCl and H_2SO_4— amongst the most prominent gases emitted during volcanic eruptions—serve as liquid binders for the establishment of inter-particle, hydrostatic attraction forces. As additional solid binder, $CaSO_4$ and NaCl are used. Both of these chemical compounds are typically found on volcanic ash surfaces and also in volcanic ash aggregates. A dependency of aggregation efficiency on relative air humidity, grain size, grain morphology, temperature, Stokes regime and Reynolds Number was experimentally proven. Further, the re-production of diverse textural and structural properties, present in natural ash aggregates, was possible.

In order to investigate their chemical and physical properties, experimentally-produced aggregates were analyzed through optical (microscopy), chemical (surface leaching) and electronical (Secondary Electron Microscopy) methods. Results show, for example, the capability of acids such as HCl to leach chemical compounds like halites (e.g. NaCl)—or environmentally hazardous elements like fluoride—out of volcanic ash, thereafter releasing them on the ash surfaces. Halites produced through these chemical reactions serve as a cementation agent for aggregates and grant them stability. Halites and other soluble compounds are transported as salt-water brines (in presence of a solubility agent such as water) along the particle surface. Capillary forces pull the salt-water solution to particle—particle contacts, at which points stable salt bridges establish during the drying processes. The size of these solid bridges is dependent on the available salt and comprises a controlling factor on the stability of aggregates.

Besides the fundamental problem under which circumstances ash particles aggregate, it is further important to investigate disaggregation processes. Currently (2017), numerical

plume forecasting models treat aggregated ash particles as matter which is forced to prematurely fall out from the atmosphere and not disperse any further. However, ash aggregates are highly unstable and may break up into their primary particles upon collisions with other particles or aggregates. Due to their lower mass, primary particles may then remain in the atmosphere and, contrary to the existing model assumptions, will not be sedimented. With respect to this problem, the stability of diverse experimental aggregates is studied in this dissertation. Through impact experiments, aggregates with differing grain morphologies (irregularly shaped ash grains and spherical glass beads), grain sizes, and salt concentrations (solid binder) are destroyed and the exact impact energy is measured. Experiments highlight that aggregates with high salt concentrations and coarse grain sizes of up to 100 µm tend to be the most stable. Grain morphology was not seen to exert significant influence on aggregate stability.

Experimental results on particle aggregation and disaggregation are finally applied in a multi-disciplinary, comparative study concerning volcanic, artificial, and meteorite impact-related particle aggregates. Textural and structural commonalities and differences between aggregates—the interpretations and implications of which are explained throughout this dissertation—afford a hypothetical view of aggregation processes arising during major impact events that have not, to date, been witnessed by humans. In total, this dissertation reflects the entire life cycle of an ash aggregate, from its generation to its potential sedimentation or destruction. While examining mechanisms on experimental scales, this thesis interrogates aggregation and disaggregation of volcanic ash with respect to the processes and scales encountered in nature. Scientific results of this study offer another component for the quantitative improvement of numerical ash plume forecasting models, especially concerning the propensity for particles to aggregate and their resulting stability and potential to sediment.

Preamble

Chapter I serves as a literature review about particle aggregation in different fields of science. Chapter II is published in Earth and Planetary Science Letters. Only slight modifications have been done in order to adapt formatting to overall dissertation design. Chapter III is published in Scientific Reports. Only slight modifications have been done in order to adapt formatting to overall dissertation design. Chapter IV is published in Scientific Reports. Only slight modifications have been done in order to adapt formatting to overall dissertation design. Chapter V is published in Bulletin of Volcanology. Only slight modifications have been done in order to adapt formatting to overall dissertation design. Chapter VI serves to re-capture significant findings of this thesis and gives an outlook about future work.

Mueller, S.B., Kueppers, U., Ayris, P.M., Jacob, M., Dingwell, D.B. (2016). Experimental volcanic ash aggregation: Internal structuring of accretionary lapilli and the role of liquid bonding. Earth and Planetary Science Letters 433:232-240.

Mueller, S.B., Ayris, P.M., Wadsworth, F.B., Kueppers, U., Casas, A.S., Delmelle, P., Taddeucci, J., Jacob, M., Dingwell, D.B. (2017). Ash aggregation enhanced by deposition and redistribution of salt on the surface of volcanic ash in eruption plumes. Scientific Reports 7:45762.

Mueller, S.B., Kueppers, U., Ametsbichler, J., Cimarelli, C., Merrison, J.P., Poret, M., Wadsworth, F.B., Dingwell, D.B. (2017). Stability controls of volcanic ash aggregates against break-up processes. Scientific Reports 7:7440.

Mueller, S.B., Kueppers, U., Huber, M., Hess, K.U., Poesges, G., Ruthensteiner, B., Dingwell, D.B. (2018). Aggregation in particle rich environments: a textural study of examples from deposits of volcanic eruptions, meteorite impacts and fluidized bed processing. Bulletin of Volcanology 80:32.

Author Contributions

Chapter I: Introduction

Written by S. Mueller

Chapter II: Experimental volcanic ash aggregation: internal structuring of accretionary lapilli and the role of liquid bonding.

S. Mueller, U. Kueppers and M. Jacob performed experiments at Glatt Ingenieurtechnik GmbH, Weimar. S. Mueller performed analysis of samples. All authors interpreted the data and contributed to the manuscript.

Chapter III: Ash aggregation enhanced by deposition and redistribution of salt on the surface of volcanic ash in eruption plumes

S. Mueller, M. Jacob and U. Kueppers performed the aggregation experiments, S. Mueller and P. Ayris leached the samples and compiled the first draft of the manuscript. A. S. Casas performed surface area determination. S. Mueller and J. Taddeucci performed the SEM measurements. S. Mueller and F. Wadsworth performed liquid spreading modelling and finalized the submitted manuscript. All authors interpreted the data and contributed to the manuscript.

Chapter IV: Stability of volcanic ash aggregates and break-up processes

S. Mueller and U. Kueppers produced artificial aggregates. S. Mueller, J. Ametsbichler, U. Kueppers and J.P. Merrison performed impact experiments. S. Mueller and C. Cimarelli carried out SEM analysis. All authors interpreted the data and worked on the finalization of the manuscript.

Chapter V: Aggregation in particle rich environments: a textural study of examples from volcanic eruptions, meteorite impacts and fluidized bed processing.

S. Mueller, U. Kueppers, M. Huber and G. Poesges sampled Nördlinger Ries Aggregates. S. Mueller and U. Kueppers sampled volcanic aggregates. S. Mueller and U. Kueppers generated artificial aggregates. K.U. Hess and B. Ruthensteiner performed x-ray CT analysis. S. Mueller performed structural and textural analysis of all samples. All authors interpreted the data and worked on the finalization of the manuscript.

Chapter VI: Conclusions

Written by S. Mueller

Acknowledgements

First I wish to thank Don and Ulli for letting me carry out my studies within their Volcanology research group in Munich. Despite their incredibly overloaded calendars, they always found time to sit down and discuss urgent topics. I have enjoyed every single day of my PhD over the last three years and was amazed by the great freedom afforded me under their supervision. The fact that the PhD topic was allowed to evolve after my own visions gave me the personal impression of being a real scientist rather than a typical PhD student. Thanks for this unique experience, I would always come back to you!

Vorrei poi dire grazie alla persona che è per me amica, compagna e moglie, Clara. Grazie per esser diventata una parte importante della mia vita durante questo dottorato. Il tuo carattere un po' siciliano, un po' francese e un po' caraibico (che può a volte evolvere in un mix esplosivo) è proprio quel pizzico di sale che rende la mia vita saporita! Da quando ti conosco, non c'è mai stato un giorno noioso e non solo tu sei la miglior distrazione nella mia quotidiana vita lavorativa (per esempio mentre scrivo una tesi di dottorato), ma sei la gioia più grande che avrei mai potuto desiderare! Grazie per esserci sempre quando ho bisogno di te!

Great thanks goes to the whole VERTIGO network, within which I carried out this PhD. Ulli, Diego, Greta – you kicked off a really cool program, that had everything to it a PhD student can wish for: fieldtrips, workshops, conferences, secondments in industry and research labs – fantastic. But the best network would be nothing without the right people in it! Tiger, Vale, Stefano, Andreas, Kathrin, Pablo, Joali (Tequila Tequila!), Lok, Antonio, Inga, Ines, Pierre-Yves – I made many new friendships with you guys and I will never forget the fantastic times we spent together in the last three years all over the world! And I hope for many more great days to come!

My further gratitude goes to Glatt Ingenieurtechnik in Weimar, without whom the whole PhD would not have been possible. Thank you, Michael Jacob, Katja, Uli, Melanie, Christian and all the rest of the Glatt team for your tremendous support during all the numerous stays I had in Weimar. Also thanks to Corinna Teubert who perfectly organized each and every period I had at Glatt.

Thanks to my former mentor Steve Lane, who settled my first contact with volcanic ash aggregation at Lancaster University – which also brought me to where I am now. Thank you, Steve, also for still being available and highly responsive on my emails and giving scientific advice.

Special thanks goes to Jamie who polished up the English of this Dissertation!

Un grand merci va à mon co-bureau Mathieu! Je suis très content de la super relation d'amitié qui s'est développée tout au long de cette thèse. Avec toi, l'expression «plaisir au travail» a atteint un niveau supérieur! Merci pour les nombreux après-midi au lac aux alentours de Munich, les soirées au bar, les innombrables pauses café-thé sur le balcon et vidéos youtube drôles. Tu me manqueras à Hawaii !! Klaxons forever !

Thanks to all the fantastic people I met and friendships I made throughout the last 8 years of studying Geology and Volcanoes: in Munich, in Lancaster and in many other parts of the world! My memories and feelings of this time wouldn't be half as good without you: Ale, Luigi, Mala, Buchners Max, Markus, Irving, Susi, Schorsch, Kotte, Tom, Daniel, Freddo, Jamie, Graeme, Magda, Fiona, Caroline, James, Jules, Dan, Klaus, Guilhem, Cristian, Paul, Fabian, Stefano, Ana, Michaela, Jonathan, Francisco, Laura, Daniele, Claudia, Helen, George, Anna, Jon, John, Hannah, Tom and many more.

Thanks to a fantastic international community of volcanologists in which I feel home by now. Especially thanks to Jacopo, Jon, Rich, Pierre, Hugh, Corrado, Betty, Kai, Nick, Paul, Costanza and Bruce.

Merci an meinen Tölzer Freundeskreis, unsere unzähligen Schafkopfabende, Kickerturniere, Tölz-unsicher-machen-Abende (Thoabm vs. Verkehrsschild), Bergtouren, LAN-Abende, durchzockte Counterstrike (Wuschl, befrei scho moi de Geiseln), Starcraft und Diablo Nächte (Deadman is usually dead), Grillabende (lang lebe der Weber vom Hansi), Alpamare Ausflüge (R.I.P.), Kirchseewochenenden, Rad- und Skiurlaube, Quadexpeditionen, Haus-Otto-Erforschungen, Wasserrutschenwettbewerbe, Vanillesoßen-Wettkampftrinken, Popcornfütterungen, Krapfengeschwindigkeitsessen, Kuba Befreiungen (des wird jetzt echt mal wieder Zeit), Sub und Kult-Abende, Fussballnachmittage, Colt-Härteteste (Mitsubishi forever), Schwaz Ausflüge und wahrscheinlich noch 1000 andere Sachen die mir grad nimmer einfallen – es war grandios! Thoabm, Hansi, Flori, Micha, Kranz, Wuschl, Matt, Judith, Bene, Fobi, Siegl, Gasti, Kellner – Spezl wia eich gibt's nur oamoi!

Zu guter Letzt, den wohl wichtigsten Dank an meine Familie. Danke für eure kontinuierliche Unterstützung in jeglicher Hinsicht während meines Studiums in den letzten acht Jahren. Vor allem wegen euch bin ich jetzt an der Ziellinie angekommen!

Table of contents

List of figures

List of tables

Chapter I Introduction

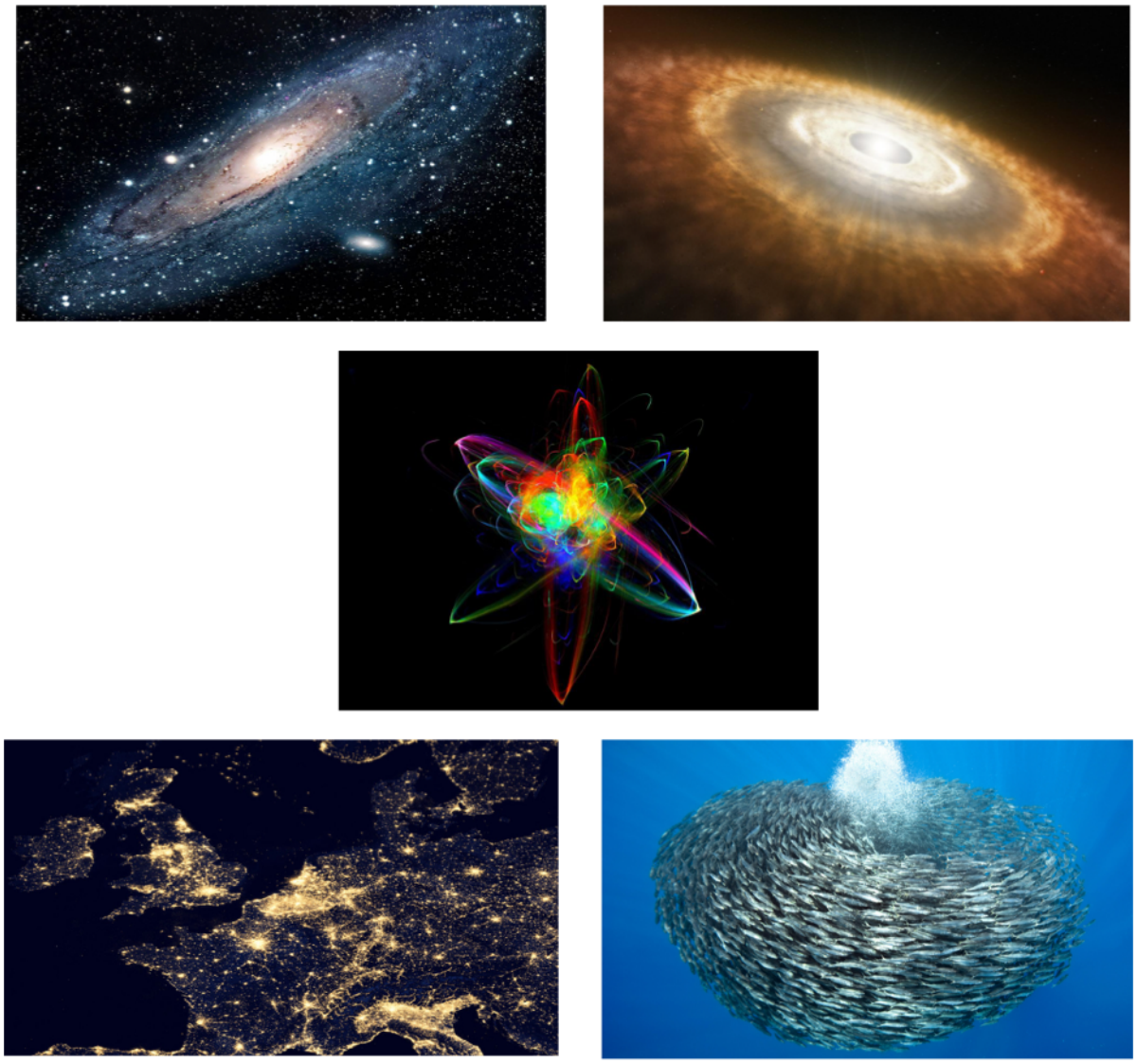

Figure I.1: Aggregation in different scales: upper left: aggregation of solar systems forming the Milky Way (*source: collective-evolution.com*); upper right: dust accretion forming our solar system (*source: universetoday.com*); center: artistic impression of an atom: aggregation of photons, electrons and neutrons – representing the ultimate component building up the entire universe (*source: fineartamerica.com*); lower left: accretion of populated areas in central Europe seen from space (*source: nasa.gov*); lower right: accretion of fish forming a shoal (*source: wired.com*).

I.1 Volcanic Ash Aggregation

Explosive volcanic eruptions are events capable of releasing volcanic material into the atmosphere (on the order of km^3 dense rock equivalent, DRE). Primary fragmentation processes during a given eruption reflect a combination of rapid magma decompression and bubble overpressure (Zheng, 1999; Melnik et al., 2004), explosive vesiculation (Sparks, 1978), and strain-induced fragmentation (Dingwell, 1996; Papale, 1999). During primary fragmentation, magma changes from being a continuous liquid containing gas bubbles (and crystals) to being a continuous body of gas containing droplets of the bubbly magma (pyroclasts). Pyroclasts smaller than 2 mm in diameter are referred to as volcanic ash (Fisher, 1961) and have the potential to remain in the atmosphere for days to weeks (Rose and Durant, 2009). Consequently, ash can be transported over continental or hemispherical scales following explosive volcanic eruptions, dependent on the details of atmospheric circulation. Volcanic ash poses hazards to the aviation industry by melting in jet turbines (Casadevall, 1994; Prata and Tupper, 2009; Bonadonna et al., 2012), to human health by entering respiration systems (Horwell and Baxter, 2006), to the environment (Ayris and Delmelle, 2012; Wardman et al., 2013) and agriculture (Wilson et al., 2010; Wilson et al., 2011), as well as to society in general by damaging infrastructure (Wilson et al., 2012). It is important here to note that most of the above described hazards are associated with human systems that have developed on volcanically short timescales. Volcanic ash clearly also may have positive effects for agriculture or ecosystems in general: life on Earth evolved in the presence of volcanism.

Under given conditions—in plumes or pyroclastic density currents (PDCs: collapsing and ground-hugging ash plumes)—ash particles can cluster together to form aggregates. Particle-particle contact is either established by crossing particle trajectory lines and coincidental collisions or up to three basic, primary attraction forces: hydrostatic or electrostatic attraction forces and Van der Waals forces (Salman et al., 2006). All three types of attraction forces are briefly presented below; the focus of the work presented in this dissertation however is on ash aggregation as a consequence of mainly hydrostatic attraction forces, causing liquid surface tension bonding between particles (wet aggregation).

A prerequisite for hydrostatic attraction and subsequent bonding of particles is the presence of liquid, such as H_2O, on their surfaces. Liquid bonding may establish between two colliding ash particles, which may stick together and dissipate rebound forces upon contact (Ennis et al., 1991). Hydrogen bonding of H_2O molecules occurs as an effect of the high electronegativity of oxygen relative to hydrogen atoms, which leads to an imbalance of the molecule's electron distribution. This imbalance creates positive and negative poles (polarized covalent binding) within the molecule (dipoles). Interaction between negative and positive dipole poles causes molecules to bridge together: a phenomenon referred to as hydrogen

bonding (Mortimer and Mueller, 2007). Hydrostatic attraction is constant in its force up to a particle separation distance of approximately 10 nm, where after attraction quickly decays to zero (Fig. I.2).

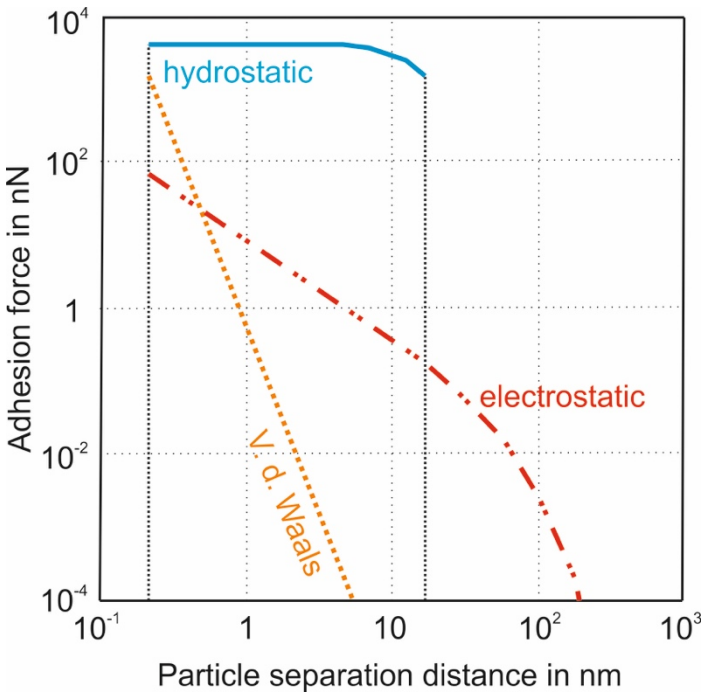

Figure I.2: adhesive forces of hydrostatic, electrostatic and Van der Waals forces depending on respective particle separation distances. Hydrostatic attraction forces are strong but only on short distances. Electrostatic and Van der Waals attraction forces are initially strong on short distances but decay quickly. Figure modified after Salman et al. (2006).

Electric charging of ash is achieved via fragmentation mechanisms, ash interactions with water or size dependent charge separation (Mather and Harrison, 2006). Charging through fragmentation has to be distinguished into 1) tribo-electrical or frictional charging and 2) fracto-emission or fracto-charging. In the first case, transfer of electric charges from one particle to the other may occur due to different work functions of the two particles (Matsusaka and Masuda, 2003; McCarty and Whitesides, 2008; Matsusaka et al., 2010; Alois et al., 2017); in the second case, particles such as electrons, positive and negative ions, and neutral atoms are emitted following rock fracture, in tandem with the emission of electromagnetic radiation. Separation of charge on a fracturing rock surface forms an electric field that liberates exoelectrons. The consequence is disequilibrium of electrons on fractured rock particles, resulting in them being positively or negatively charged (Dickinson et al., 1984, Mather and Harrison, 2006).

Electric charging of ash particles through water interactions was first indicated by Björnsson et al. (1967) through laboratory experiments, after Anderson et al. (1965) measured electrification of ash during the 1963 phreatic eruption of Surtsey off the coast of Iceland.

Electrical charging in this instance arises through the volatilization of sea salt particles by the hot rock, which serves to carry positive charge away. This concept can obviously also be applied on surficial ash salts produced by other mechanisms, such as diffusion driven precipitation during ash-acids interactions (Ayris et al., 2014).

Due to the non-existence of a conductive path to Earth within volcanic ash plumes, charges remain preserved on fractured particles. Electric charging of pyroclasts together with fall velocity differences of neighboring pyroclasts in the atmosphere are sufficient to lead to particle aggregation based on electrostatic attraction. Electrostatic attraction forces decay non-linearly ($1/d^2$ relationship) in their strength with increasing distance between two single particles (Fig. I.2). Electrostatically charged particles of a 100 µm diameter can attract particles in a range of up to three times their own diameter; this dimensionless range of attraction increases with decreasing particle diameter: 10 µm particles may attract other particles in a range of up to ten times their own diameter, and 1 µm diameter particles may attract other particles within a range of around 30 µm, i.e. thirty times its own diameter (Salman et al., 2006; Gilbert and Lane, 1994; Gilbert et al., 1991).

Van der Waals forces are weak but omnipresent attraction forces, describing the force between two dipoles of molecules or atoms (the sum of their attractive or repulsive interactions). They decrease with increasing particle separation distance and are only relevant for distances smaller than 100 nm (Fig. I.2, Mortimer and Mueller, 2007).

Numerous field, experimental and numerical studies were carried out in the past two decades in order to shed light on the various parameters controlling ash aggregation. Besides coincidental particle collisions through crossing particle trajectories, several studies suggest hydrogen attraction forces to be the second most important mechanism leading to first contact and subsequent bonding and aggregation of particles; this is proposed in both field studies concerning ash aggregates (Moore and Peck, 1962; Self and Sparks, 1978; Sorem, 1982; Hayakawa, 1990; Watanabe, 1999; Trusdell et al., 2005; Branney et al., 2008; Bonadonna et al., 2011) and in numerical aggregation models (Rosi, 1991; Iveson et al., 2001a,b; Veitch and Woods, 2001; Costa et al., 2010; Folch et al., 2010). Laboratory-based experiments provide proof that liquid bonding is a major player in ash aggregation efficiency (Gilbert and Lane, 1994; Schumacher and Schmincke, 1995; Telling and Dufek, 2012; Van Eaton et al., 2012; Telling et al., 2013). However, due to their much larger range of action, electrostatic forces also play an important role in attracting particles to each other (Brazier et al., 1982; Schumacher and Schmincke, 1995; Bonadonna et al., 2002). Since electric charging within volcanic plumes is a well-known phenomenon (Cimarelli et al., 2013), far-reaching electrostatic forces could be an important mechanism causing collision of particles that would

otherwise follow separated trajectories. Notably, the importance of Van der Waals attraction forces in the field of volcanic ash aggregation has not yet been reported.

Experiments have shown that particles bound by either electrostatic or hydrostatic bonding forces are not sufficiently strong enough to resist impact forces during sedimentation processes (e.g. James, 1999; James et al., 1998, 2000, 2002). As volcanic ash aggregates are a common occurrence in eruption deposits, stronger binding mechanisms—such as cementation—have been postulated to make aggregates survive high-energy volcanic environments or sedimentation processes. On ash surfaces, a variety of salts can precipitate, predominantly NaCl or $CaSO_4$ (Witham et al., 2004; Ayris et al., 2014), which will partially dissolve under the influence of external liquids. During evaporation of liquids, re-crystallization of dissolved salts can strengthen the ash aggregate. Cementation through surface salts has been described for several ash aggregates (Sheridan and Wohletz, 1983; Tomita et al., 1985; Gilbert and Lane, 1994; Brown et al., 2010; Scolamacchia and Dingwell, 2014).

In the event of successful particle aggregation, aggregates may be subsequently deposited during or after volcanic eruptions, thereafter to be collected and analyzed (Brown et al., 2012 and references therein). Aggregates range from µm to a few cm in diameter, with electrostatically bound aggregates rarely growing larger than 1 mm in diameter (Bonadonna et al., 2011). This manuscript adheres to an aggregate classification scheme proposed by Brown et al. (2012), Fig. I.3. It consists of two categories of ash aggregates, which further divide into five sub-categories: the two main categories are particle clusters (PC) and accretionary pellets (AP). PC aggregates are sub-divided into ash clusters (PC1) and coated particles (PC2). Ash clusters are fragile, irregular shaped and commonly disaggregate on deposition. Aggregate densities are generally less than 200 $kg.m^{-3}$ due to their loose compound structure. PC1 aggregates are in the range of a few mm in diameter. Coated particles are comprised of a crystal (fragment) or clast and are (partially) covered in ash particles. PC2 aggregates can significantly vary in size, from mm to several cm in diameter. The surrounding ash coating can be irregular in its thickness but usually never exceeds a few mm. Accretionary pellets, on the other hand, can be divided into poorly-structured pellets (AP1), accretionary pellets (AP2) and liquid pellets (AP3). AP1 aggregates have sub-spherical to spherical shapes; the aggregated particles are packed more densely than PC type aggregates, which ultimately results in higher aggregate densities (up to 1600 $kg.m^{-3}$). AP1 aggregates show size ranges of several mm and are rarely larger than 1 cm in diameter. AP2 compounds are sub-spherical to spherical and show complex internal structures with a massive or poorly-structured ash core, surrounded by one or more fine grained, concentric rims. AP2 aggregates range in size from several mm up to few cm in diameter. Sampling and analysis of ash

aggregates allows for the reconstruction of certain eruptive processes (see also chapter I.2), making them important telltale indicators.

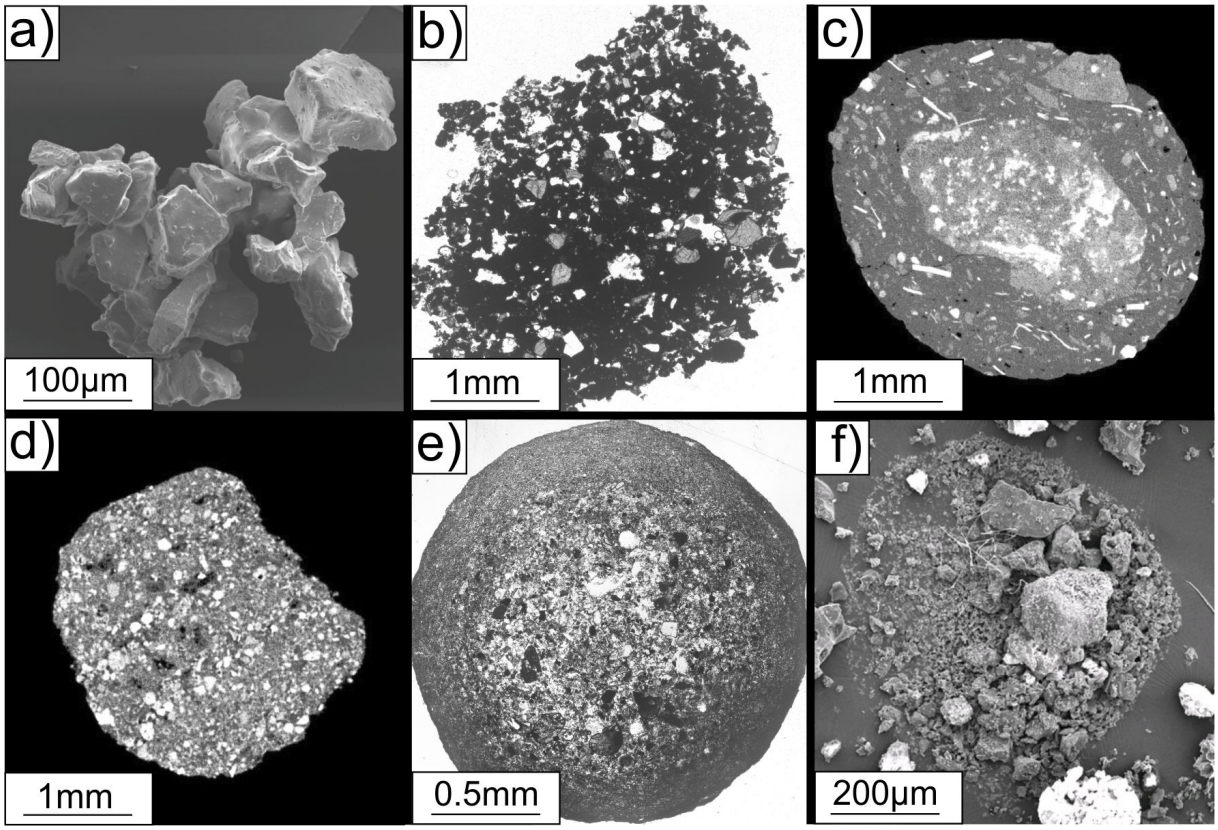

Figure I.3: overview of volcanic ash aggregate types, following the scheme of Brown et al. (2012). a) shows a SEM image of a loosely-bound, artificial ash cluster (PC1) with a few hundred µm in diameter. b) shows a thin section of an irregular, unstructured ash cluster (PC1) several mm in diameter from the Eifel Volcanic Field, Germany. c) shows a x-ray computed tomography (x-ray CT) of a coated particle (PC2), Sahand Volcano, Iran. d) shows a x-ray CT image of a poorly structured pellet: in comparison to b), it is denser, has a sub-spherical shape and a more confined particle size distribution (PSD). Sample is from the Astroni Crater, Italy. e) shows an accretionary pellet (AP2) which shows a spherical shape and an inner partitioning into a coarse-grained core and a fine grained, concentric outer rim. Pellet sampled from Stromboli, Italy. f) shows remnants of a liquid pellet (AP3). Pellet from the 2010 Eyjafjallajökull eruption, Iceland. Image f) given with the courtesy of Costanza Bonadonna.

Various formation mechanisms for the internal stratification of AP type aggregates have been proposed in the past. Gilbert and Lane (1994) present two possibilities based on recirculating wind tunnel experiments: (1) in-plume scavenging of particles through falling liquid drops: internal drop circulation within drops of a stable shape will assign differing mobility to different particle sizes, causing particle size dependent structuring of the growing aggregate; (2) growing aggregates traverse plume regions containing different grain size populations, which again causes the generation of concentric structures (a theory previously proposed but never proofed by various authors such as Moore and Peck, 1962; Reimer, 1983; Sheridan and Wohletz, 1983). A similar conclusion is drawn by Van Eaton et al. (2012):

following wet aggregation experiments with ash, they suggest concentric structuring to be generated when a pre-existing PC type aggregate is transported through a dominantly fine grained plume region, in order to amass a fine-grained rim. In a follow-up study, Van Eaton et al. (2015) suggest that aggregate growth is arrested once they reach the freezing isotherm (which may reach -70°C in the presence of sulphuric acid). In this case liquid bonding is precluded; however, falling, hailstone-like aggregates may be re-entrained into warm plume areas which could lead to additional stages of wet growth and layering. Ice nucleation and hydrometeor-enhanced tephra sedimentation has been proposed previously by Durant et al. (2009). The generation of internal structures in AP aggregates in combination with PDCs (Pyroclastic Density Currents) has been proposed by numerous field studies: during the 1957/1958 Capelinhos eruption (Azores), PDCs were observed to move through falling tephra and deposit accretionary lapilli afterwards. Contrastingly, fall deposits from this eruption only contain unstructured particle clusters. Cole et al. (2001) hypothesize that PDCs moving through ashfall columns can pick up particle clusters and rework them into accretionary lapilli. Similarly, Brown et al. (2010) describe the formation of accretionary pellets within the Bandas del Sur PDC deposits on Tenerife: structureless ash pellets, formed in co-ignimbrite ash clouds, fall into deep layers of an ongoing PDC and act as a nucleus or core; turbulence within the PDC then fosters accretion of fine-grained, concentric laminations around the ash pellet. The uppermost layers of the Bandas del Sur deposits, in contrast, only contain particle clusters without any concentric laminations. Similar field observations and accretionary pellet formation is described by Van Eaton and Wilson (2013) for Oruanui deposits, New Zealand. Finally, Schumacher and Schmincke (1995) suggest a change of binding forces from hydrogen to electrostatic bonding to be responsible for internal structuring of accretionary pellets.

I.2 Volcanic ash as a hazard and why aggregation matters

As briefly mentioned above, due to its physical and chemical attributes, volcanic ash may pose an abundance of hazards to human activities that have developed on timescales shorter than ash fall repeat times and therefore do not have ash resilience designed in. Several strategies for the mitigation of volcanic ash risks do exist and are continuously improved; they span from local to international organizations: co-operations of communities with national agencies such as the United States Geological Survey (USGS) or the Istituto Nazionale di Geofisica e Vulcanologia (INGV) in Italy offer training and public awareness schemes to inform population about natural risks, their potential consequences and how to behave in case of an emergency (e.g. Hill et al., 2002). Another tool to mitigate the risk of volcanic ashfall, achieved on national to international levels, is the forecasting of ash plume dispersal during ongoing eruptions. Early warnings of potentially affected areas or closures of airspace to air traffic can decrease economic losses due to ash impact and more importantly, protect human life (e.g.

Scollo et al., 2009, Bonadonna et al., 2012). Ash plume forecasting methods are improved, applied and communicated by universities and national and international organizations, such as the United Kingdom Meteorological Office (UK Met Office) or the globally-organized Volcanic Ash Advisory Centers (VAACs).

Though ash plume dispersal modeling provides a powerful tool for volcanic ash risk mitigation, it has to cope with many uncertainties. One of the most critical uncertainties is the process of ash aggregation: aggregated particles are heavier as a compound than their respective non-aggregated counterparts. This changes their aero-dynamical behavior and provokes premature fallout (Lane et al., 1993; Le Roux, 2014), which may significantly alter plume dispersal (an effect referred to as secondary thickening, Fig. I.4; see also Durant et al., 2009, Mastin et al., 2016). Plume dispersal is further dependent on various other factors, such as Eruption Source Parameters (ESP). These provide the crucial input for tephra dispersal models and have been studied in detail for several eruptions, e.g. the July 2013 eruption of Tungurahua (Parra et al., 2016) and the 6th May 2010 Eyjafjallajökull eruption (Gudmundsson et al., 2012; Bonadonna et al., 2011); a summary of ESPs for more than 30 eruptions over the past 30 years is provided by Mastin et al. (2009). Ash dispersal further depends on wind and weather conditions (e.g. Costa et al., 2010; Durant et al., 2009; Mastin et al., 2009). Of particular interest for ash plume forecasting models is the eruption mass composed of fine ash (particles with a diameter < 63 µm), e.g. Parra et al. (2016), which has the potential to stay in ash clouds for days to weeks. Numerical ash plume forecast models struggle with the implementation of particle aggregation, due to high uncertainties in how ESPs and atmospheric parameters affect aggregation efficiency. The first model to implement ash aggregation is provided by Folch et al. (2016), using the FPLUME-1.0, a steady-state 1-D (one-dimensional) cross-section-averaged eruption column model based on the buoyant plume theory (BPT: e.g. Costa et al., 2016 and references therein). FPLUME-1.0 incorporates ESPs such as eruption start time and duration, vent coordinates and elevation, conditions at the vent (exit velocity of pyroclasts, magma temperature, magmatic water mass fraction and total grain size distribution: TSG), mass eruption rate, and plume conditions (total column height, plume bending, entrainment of ambient moisture, the influence of water phase changes on the energy budget, particle fallout and re-entrainment by turbulent eddies, variable entrainment coefficients fitted from experiments). Particle aggregation is regarded in the presence of liquid water or ice that depends on plume dynamics as well as the amount of liquid water and ice existing in the plume. Wet particle aggregation is predicted to happen in plume regions where water vapor (of magmatic origin or entrained moist air) encounters condensation and deposition conditions (Costa et al., 2010; Folch et al., 2010). The implemented aggregation model is based on the work by Costa et al. (2010) and neglects dry aggregation or disaggregation processes. Further deductions had to be made in aggregation

modeling, such as water being the only liquid binding agent or aggregation only involving particles of a certain size class; these simplifications are due to a lack of quantitative data for further calibration. One of the fundamental aims of this study is to provide datasets that allow improved usage of ESPs in dispersion modeling by explicitly accounting for the mechanisms of ash aggregation and disaggregation.

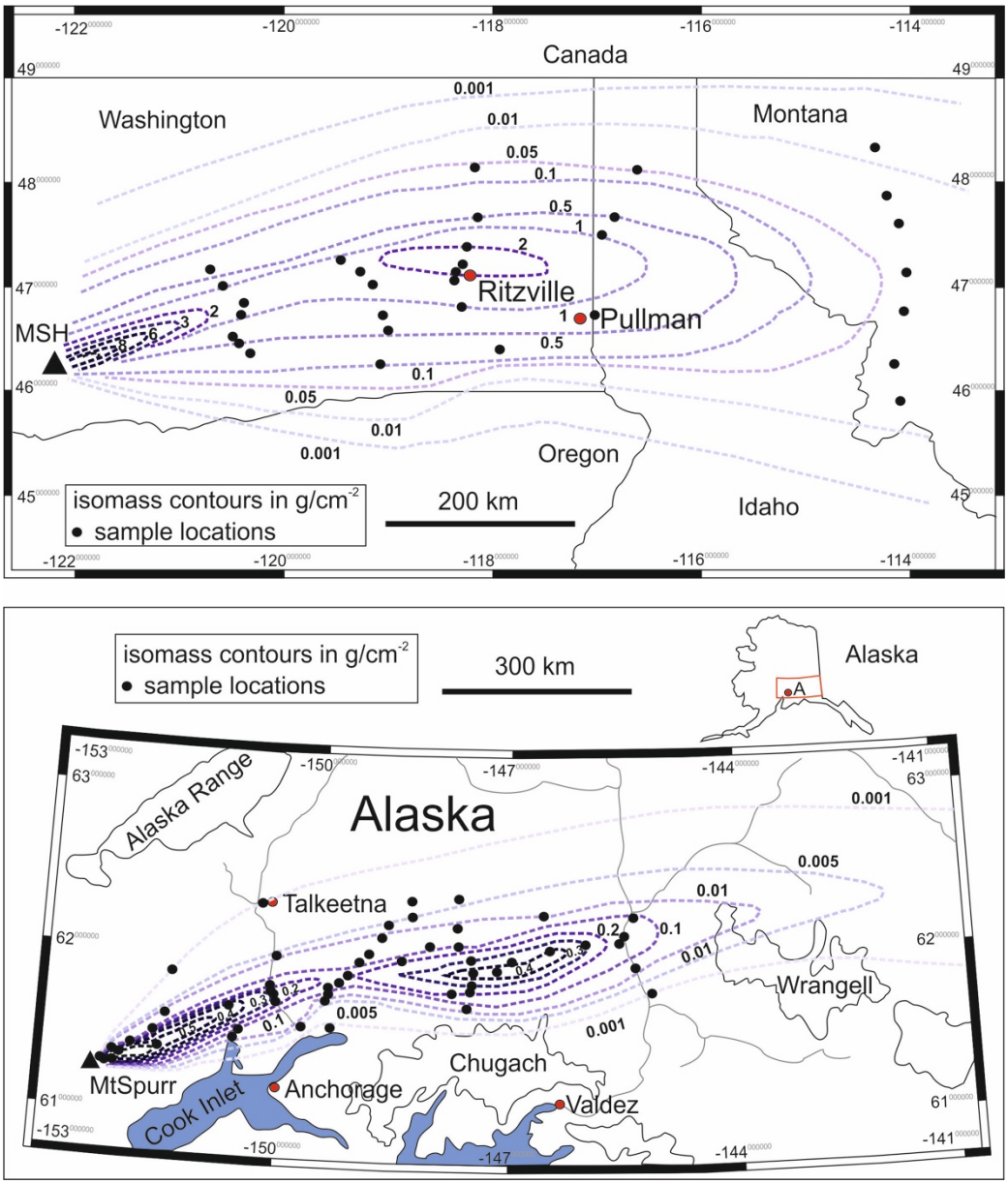

Figure I.4: Secondary thickening effects in ash deposits caused by aggregate fallout following the 1980 Mount St. Helens eruption, Washington (a), or the 1992 Crater Peak eruption of Mount Spurr, Alaska (b). Aggregation is capable of altering ash deposit thickness significantly, even in distant (few 100 km of source) areas. Data modified after Sarna-Wojcicki et al. (1981), Mount St. Helens, and McGimsey et al. (2002), Mount Spurr.

I-3 Aim, approach and structure of this study

Recent ash plume dispersal models implement ash aggregation processes and have significantly improved ash plume forecasting. Fundamental research in the field of volcanic ash aggregation is now required to further advance numerical simulations like FPLUME-1.0, as outlined in the preceding section. Specific ESPs—such as particle size distribution (PSD), particle morphology, humidity or gas release—must be applied to gather valuable information about ash aggregation efficiency and the probability of aggregate sedimentation. This study aims to define critical Eruption Source Parameters for ash aggregation by experimentally investigating the entire lifecycle of wet ash aggregates: from formation mechanisms and parameters controlling aggregation efficiency, to particle surface processes such as cementation, up to final deposition or disaggregation and possible re-entrainment of primary particles into the atmosphere. Finally, these experimental results are validated and applied to aggregates formed during volcanic eruptions and meteorite impact events.

The experimental approach of ash aggregation of this study is achieved through the utilization of industrial powder aggregation technology at *Glatt Ingenieurtechnik GmbH*, Weimar, Germany. Particle aggregation is a crucial procedure in several industrial sectors, in particular in the food, feed, pharmaceutical, fertilizer, detergent, and mineral processing industries. A widely-used aggregation technique is fluidization of particles. Solid particles are hereby placed in a vessel. To generate a fluidized bed of particles, drag forces exerted by externally introduced fluids have to exceed the particles' total weight. Above minimal fluidization velocity, particles behave like a liquid. Single particles follow stochastic streamlines (Salman et al., 2006). A nozzle is installed to deliver an atomized spray of binder liquid (e.g. a NaCl-H_2O mixture) into the fluidized bed. Binder droplets can adhere to particle surfaces and upon evaporation precipitate small crystals of binder material (such as e.g. NaCl crystals) on the particle surface. In a second fluidization step, higher spray rates of liquid binder allow for the establishment of liquid bridging and actual aggregation between particles. Cutting off the feed of binder liquid and subsequent drying transforms liquid bridges into solid bridges, comprising previously-deposited binder material. Particle formation in fluidized beds can be expressed in terms of population balance, which describes temporal changes of particle property distributions. Particle size enlargement through agglomeration is crucially controlled by operating conditions such as moisture, granulometry, process time, pneumatics or thermal conditions (Smith and Nienow, 1983; Banks and Aulton, 1991; Watano et al., 1996; Iveson et al., 1998; Turton et al., 1999; Uhlemann and Mörl, 2000). Industrial powder processing allows the control of abundant operation parameters, affording the opportunity to investigate the influence of specific parameters on particle aggregation. Different ESPs are thus simulated by adjusting the various operation conditions.

The following paragraphs will give a short outline of the coming chapters of this study and their position regarding the full life cycle of volcanic ash aggregates. Chapter II of this dissertation has been published in Earth and Planetary Science Letters (2016) and deals with the fundamental question of whether natural volcanic ash aggregates can be reproduced in the lab, as well as addressing the effect of various external parameters on aggregation efficiency. Experimental aggregation experiments were performed at *Glatt Ingenieurtechnik GmbH*, Germany. Via the use of fluidization technology, the study investigates the effects of binder concentration, humidity, PSD and primary particle morphology on aggregation efficiency. These are valuable results that can, in combination with ESPs, be a powerful tool for the prediction of ash aggregation efficiency during ash-rich volcanic eruptions. Moreover, the chapter explores the causes for the formation of different types of aggregates—as presented by Brown et al. (2012)—such as particle clusters (PC) or internally structured accretionary pellets (AP). By adapting a numerical model from Powder Science, the formation processes and differing environmental plume conditions for PC and AP type aggregation are explained. In turn this allows the use of these aggregates as forensic indicators for volcanic eruption processes.

Chapter III of this dissertation is under second revision in Nature Scientific Reports (2017) and deals with primary particle (particles that constitute an aggregate) surface processes in aggregates. This study focuses both on re-mobilization and cementation processes of soluble salts, as well as on diffusion-driven precipitation of salts and other agents on particle surfaces. Re-mobilization of soluble salts to particle-particle connection points significantly enforces bridging and cementation of aggregates. Further, the effect of HCl on phonolitic volcanic ash and glassbead surfaces is shown: diffusion-driven salt precipitation is capable of causing immediate and in-situ particle aggregation. This study gives microscopic insights into the pathways of surficial salt precipitation and particle aggregation mechanisms in volcanic plumes.

Chapter IV of this dissertation is submitted to Nature Communications. It deals with the potential end of an aggregate lifecycle: disaggregation processes. Besides the input of aggregation parameters and processes (Chapter II and III) into plume dispersal models, disaggregation probabilities of aggregates prior to deposition is the second big uncertainty in the field of modeling: what percentage of aggregated ash particles in plume dispersal models can be removed from the atmosphere, and what proportion will break up again and be re-entrained into the atmosphere as single, primary particles? The break-up behavior of aggregates is evaluated through high-speed video monitoring, and the chapter further tests the stability of aggregates against impact. Parameters such as impact energy, primary particle size distribution and surface morphology and binder concentration are defined as crucial

controls on aggregate strength. A model is proposed which combines a) the experimental results presented herein on aggregate stability, b) aggregation parameters from Chapter II and III, and c) Eruption Source Parameters from the relevant literature (e.g. Mastin et al., 2009) to predict ash removal from the atmosphere through aggregation.

Chapter V of this dissertation is in review at Bulleting of Volcanology. It serves both as an overlook and roundup chapter, but also contains an outlook to a third field of aggregation science. Besides the granulation industry and volcanology, particle aggregation is also present in the field of meteorite impact science, where—similar to volcanology—aggregates are used as telltale indicators for impact processes. During meteorite impact events, aggregates preferentially form in the fallback ejecta curtains and are subsequently deposited. Impact-related aggregates have been sampled from the 15 Ma Ries impact event in Bavaria, Germany. Impact aggregates as well as a wide range of volcanic aggregates and artificial aggregates are analyzed through SEM, X-ray computed tomography (CT) and thin sections, and investigated for their commonalities and differences. Importantly, this interdisciplinary approach allows a critical scrutiny of the different aggregate formation theories of each of these fields in the light of the new experimental results presented in Chapters II-IV.

Chapter VI of this dissertation is not published and serves to recapture important aspects of this doctoral thesis and give concluding remarks and an outlook for future work to be done. Important questions raised and answered throughout this work are:

1. Is it possible to mimic natural aggregation processes in the lab?
2. Which environmental, physical and chemical parameters control aggregation efficiency and to what extent?
3. What alternative aggregation mechanism could explain the generation of structural differences in particle clusters and accretionary pellets?
4. Which physical, mechanical and chemical processes are happening during and immediately before and after aggregation on particle surfaces and to what extent do they control aggregate properties?
5. Deposition or not? What makes aggregates stable enough to survive falling through the atmosphere without breaking up upon collisions and possibly remain in the atmosphere as primary particles?
6. To what extent can experimental results be applied to explain structures and textures in natural volcanic ash aggregates and meteorite impact related particle aggregates.

7. Can findings from volcanology be applied to explain yet un-witnessed formation of aggregates during major meteorite impact events?

Chapter II

Experimental volcanic ash aggregation: internal structuring of accretionary lapilli and the role of liquid bonding

Experimental volcanic ash aggregation: internal structuring of accretionary lapilli and the role of liquid bonding

Sebastian B. Mueller (1), Ulrich Kueppers, (1), Paul M. Ayris, (1), Michael Jacob, (2), Donald B. Dingwell, (1)

(1) Ludwig-Maximilians-Universität München (LMU), Earth and Environmental Sciences, Munich, Germany

(2) Glatt Ingenieurtechnik GmbH, Verfahrenstechnik, Weimar, Germany

Earth and Planetary Science Letters 433:232-240 (2016)

II.1 Abstract

Explosive volcanic eruptions can release vast quantities of pyroclastic material into Earth´s atmosphere, including volcanic ash, particles with diameters less than two millimeters. Ash particles can cluster together to form aggregates, in some cases reaching up to several centimeters in size. Aggregation alters ash transport and settling behavior compared to un-aggregated particles, influencing ash distribution and deposit stratigraphy. Accretionary lapilli, the most commonly preserved type of aggregates within the geologic record, can exhibit complex internal stratigraphy. The processes involved in the formation and preservation of these aggregates remain poorly constrained quantitatively. In this study, we simulate the variable gas-particle flow conditions which may be encountered within eruption plumes and pyroclastic density currents via laboratory experiments using the *ProCell® Lab System* of *Glatt Ingenieurtechnik GmbH*. In this apparatus, solid particles are set into motion in a fluidized bed over a range of well-controlled boundary conditions (particle concentration, air flow rate, gas temperature, humidity, liquid composition). Experiments were conducted with soda-lime glass beads and natural volcanic ash particles under a range of experimental conditions. Both glass beads and volcanic ash exhibited the capacity for aggregation, but stable aggregates could only be produced when materials were coated with high, but volcanically-relevant concentrations of NaCl. The growth and structure of aggregates was dependent on the initial granulometry, while the rate of aggregate formation increased exponentially with increasing relative humidity (12 – 45 % RH), before overwetting promoted mud droplet formation. Notably, by use of a broad granulometry, we generated spherical, internally structured aggregates similar to some accretionary pellets found in volcanic deposits. Adaptation of a powder-technology model offers an explanation for the origin of natural accretionary pellets, suggesting them to be the result of a particular granulometry and fast-acting selective aggregation processes. For such aggregates to survive deposition and be preserved in the deposits of eruption plumes and pyroclastic density currents likely requires a significant pre-existing salt load on ash surfaces, and rapid aggregate drying prior to deposition or interaction with a more energetic environment. Our results carry clear benefits for future efforts to parameterize models of ash transport and deposition in the field.

II.2 Introduction

Volcanic ash, fragments of juvenile lava, crystals and/or older rock units less than two millimeters in diameter (Fisher, 1961), is produced in large quantities during explosive volcanic eruptions. Fine volcanic ash (particle diameter, (p_d) <63µm) can be distributed far away from the eruptive vent by ash transport processes, where it may cause a plethora of hazards and impacts (Dingwell et al., 2012). Under certain conditions within eruption plumes and pyroclastic density currents, ash particles can cluster together to form ash aggregates that range from micrometers to centimeters in size. Aggregates exhibit different aerodynamic properties than the individual ash grains which comprise them, promoting their 'premature' sedimentation from the plume and decreasing their residence time within the atmosphere, relative to the individual particles in isolation (Le Roux, 2014). Thus, ash aggregation may influence ash distribution (e.g., Folch et al. 2010) and deposit stratigraphy (e.g., Durant et al. 2009).

Ash aggregates can be characterized using the terminology of Brown et al. (2012); this prior study defined two classes of ash aggregates, particle clusters (*PC*) and accretionary pellets (*AP*). Particle clusters are sub-divided into ash clusters (*PC1*) and coated particles (*PC2),* while *APs* can be divided into poorly-structured pellets (*AP1*), accretionary pellets (*AP2*) and liquid pellets (*AP3*). However, although field observations have evidenced the formation of all of these subtypes, the aggregates most commonly preserved within the geologic record tend to be *AP1* or *AP2*. The *AP1* aggregates are normally spherical or sub-spherical, ranging in diameter from several 100 µm to a few mm, and generally show poor internal structure. The *AP2* aggregates are similarly shaped, and can also grow to sizes of several mm; they consist of a relatively coarse grained core and (possibly several) fine grained rims.

The presence of the *AP1* and *AP2* aggregates in deposits evidences their comparative resilience to the highly energetic processes related to eruption dynamics and sedimentation processes. This preservation is not universal, as field studies have also documented shattered fragments of accretionary lapilli in deposits (Brown et al., 2010). However, our capacity to interpret the presence, absence and particular features (e.g., internal stratigraphy or granulometry) of aggregates within deposits as being indicative of particular eruption features or characteristics is limited. This stems from the absence of a quantitative understanding of the physical and/or chemical properties and in-plume boundary conditions which drive aggregate formation, disaggregation and the capacity of aggregates to survive deposition and be preserved in ash deposits.

The drivers on aggregate formation may relate to the mechanisms of both ash adhesion and aggregate growth. Particle adhesion is likely a product of three major forces, 1)

electrostatic bonding, 2) Van der Waals forces and 3) liquid bonding. Although electrostatic charging of volcanic plumes is a well-known phenomenon (Lane and Gilbert, 1992; Cimarelli et al., 2013) that can lead to dry aggregation (e.g. Taddeucci et al., 2011, Del Bello et al., 2015), it is neglected in this study. With maximum surface charges of ± 10^{-5} $C.m^{-2}$ observed for particles in volcanic plumes (Gilbert et al., 1991), the electrostatic attraction and binding potential of ash particles is very low and even negligible in the presence of a liquid binder, as implied by experiments in fluidized beds with other particles (Randolph, 1988; Liu and Cameron, 2001; Saleh and Guigon, 2006). In order to build large ash aggregates stable enough to be preserved in the geologic record, we consider that liquid bonding may be the most important aggregation mechanism.

Previous in-field (Trusdell et al., 2005; Branney et al., 2008; Bonadonna et al., 2011), numerical (Costa et al., 2010; Folch et al., 2010) and laboratory studies (Gilbert and Lane, 1994; Schumacher and Schmincke, 1995; Van Eaton et al., 2012) have investigated the role of liquid bonding. Vibratory pan aggregation techniques, (Schumacher and Schmincke, 1995; Van Eaton et al. 2012) have successfully reproduced ash aggregates with characteristics (bulk diameter, density or granulometry) linearly dependent on humidity or wetting, until an 'overwetting' threshold was reached, whereafter, liquid 'mud' droplets (*AP3*) were formed (e.g. Gilbert and Lane, 1994). However, the influence of liquid bonding on ash aggregate formation remains only partially constrained. For example, although laboratory experiments have generated particle clusters (*PC*), the complex internal structures typical for *AP2* aggregates have yet to be reproduced. Furthermore, the effect of additional variables such as the surface tension and viscosity of the binding liquid (e.g. Kueppers et al., 2011), which in volcanic systems may be commonly comprised of condensates of co-erupted volcanic gases (e.g., $H_2O_{(g)}$, $SO_{2(g)}$, $HCl_{(g)}$, $HF_{(g)}$), have yet to be investigated.

The preservation of ash aggregates within ash deposits may be contingent on the establishment of strong interparticle binding mechanisms within the aggregate (e.g., cementation of solid bridges). Cementation may be driven by the interstitial precipitation of various sulphate and halide salts during the evaporation of the binding liquid. This process of cementation has been invoked following investigations of several field deposits (Tomita et al., 1985; Gilbert and Lane, 1994; Brown et al., 2010). The specific chemistry and abundance of these salts may depend both on the pH of the binding liquid and its capacity to dissolve or corrode the ash surface, and on the presence of pre-existing salts emplaced by higher temperature gas-ash interactions (c.f. Witham et al., 2004, Ayris and Delmelle, 2012).

In this mechanistic study we present results of laboratory investigations on the formation and recovery of *AP1* and *AP2*-type ash aggregates. We investigated ash aggregation

within fluidized beds, commonly utilized in industrial sectors, in particular in the food, animal feed, pharmaceutical, fertilizer, detergent and mineral processing industries, for investigation or generation of aggregates. Fluidized bed systems transform a granular material from a static (i.e. solid-like) to a dynamic (i.e. fluid-like) state, promoting aggregate formation under precisely-controlled conditions such as humidity, granulometry, air flow and temperature (Salman et al., 2006). In this study, we pioneer the use of this technology for our mechanistic investigation of volcanic ash aggregate formation, and provide new insights into the variables which permit the formation and survival of ash aggregates.

II.3 Methodology

For this study, we use the *ProCell® Lab System* (Fig. II.1) by *Glatt Ingenieurtechnik GmbH*, Weimar, Germany. The *ProCell® Lab* builds aggregates from fine powders, in this case, volcanic ash or soda-lime silicate glass beads. Solid particles are placed in a vessel and a stream of fluids passes up through the voids of the granular material. To generate a fluidized bed of particles, drag forces exerted by externally introduced fluids must exceed the weight of the particles. At a critical value of fluid velocity (the point of minimal fluidization velocity), the upwardly directed drag on particles will equalize the downwardly directed gravitational forces and maintain the particles in suspension. Above this minimal fluidization velocity, particles behave like a liquid and single particles follow stochastic streamlines (Salman et al., 2006). Within the fluidized bed, particles are wetted by a fine spray of liquid, promoting formation of liquid bridges between particles; aggregate growth is crucially controlled by operating conditions such as moisture, granulometry, process time, pneumatics or thermal conditions.

II.3.1 The ProCell® Lab System

The *ProCell® Lab System* consists of three parts (from bottom to top, see Fig. II.1): the inlet air chamber, the process chamber and the exhaust housing. The Inlet air and process chamber are separated from each other by a bottom screen with a mesh size of 100 µm. An air stream is heated in the inlet air chamber and injected in the process chamber (*GF5* type, continuous fluidization) from below. The flow rate is sufficient to maintain the solid raw material in a fluidized state, while smaller particles which are lofted away from the bed by the airflow are captured within an installment of six cartridge filters. Overpressurized air is directed downwards through the cartridge filters every ten seconds, returning any trapped particles back to the fluidized bed. Liquids are injected into the *GF5* process chamber by a nozzle mounted on the bottom screen which directs its spray upwards, supplied by an external pump. Regulation of the pump allows supplying the process chamber with exactly the desired amount of liquid.

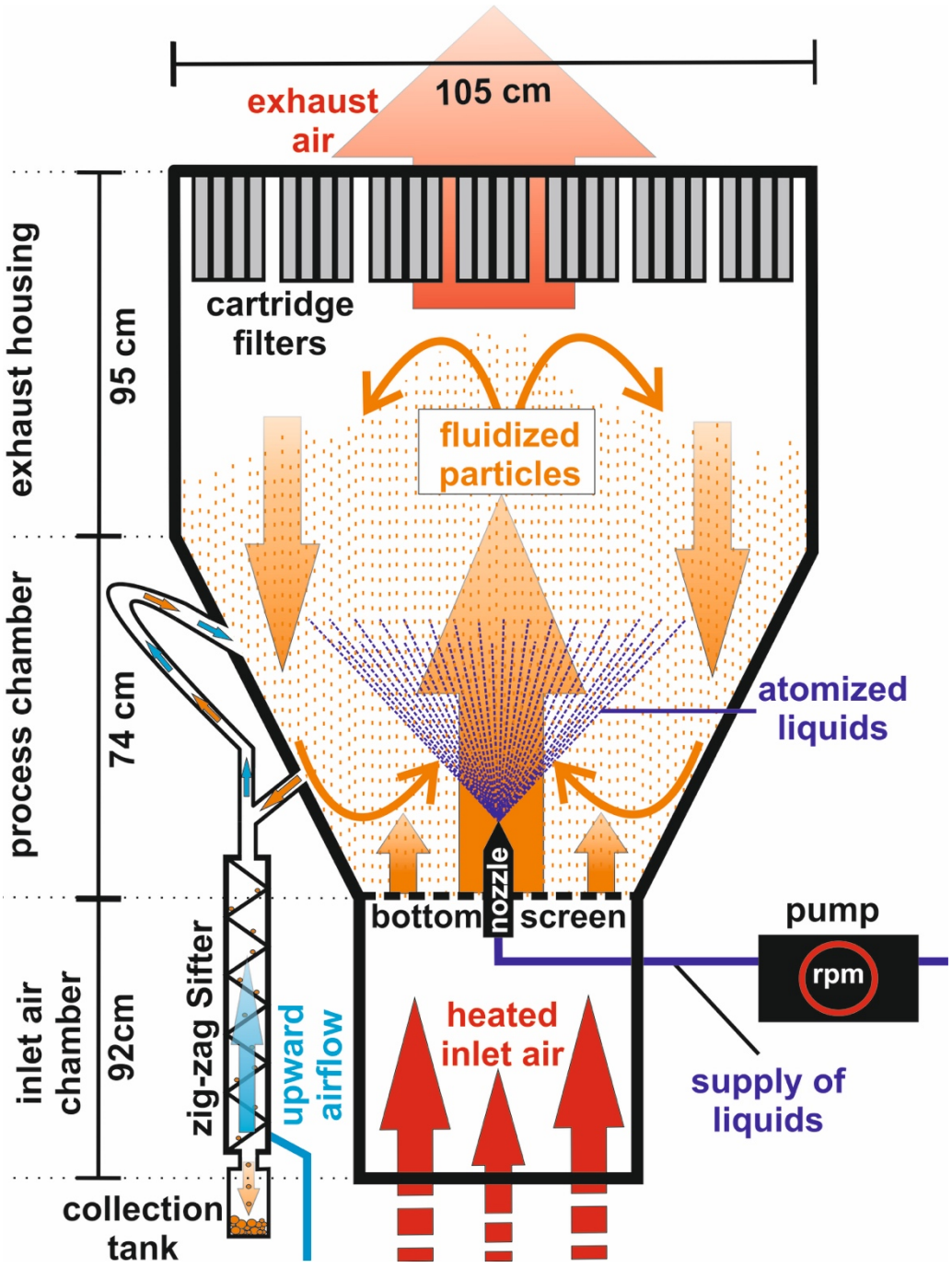

Figure II.1: *Glatt ProCell® Lab System*; solids are deposited on the bottom screen. Heated air flows from the inlet air chamber through the screen into the process chamber and drags particles upwards (fluidization). A nozzle in the center of the bottom screen sprays liquid into the fluidized particles. Liquid droplet size and spray rate are controlled manually. Topside cartridge filters separate fine particles from the exhaust air (exhaust chamber). Aggregates fall into the sifter through a contraflow air stream into a collection tank.

The *ProCell® Lab* is highly customizable in its operational conditions; the user may select the air flow through the process chamber (max. 250 $m^3.h^{-1}$), the air flow temperature

(max. 200 °C) and the pressure of the nozzle spraying the liquid (max. 6 bar). The instrument also maintains a constant record of air humidity and temperature in the process chamber.

The *ProCell® Lab* can either be run in batch or continuous mode; in the latter, a 'zig-zag-sifter' (Fig. II.1) is installed at a product outlet, permitting aggregates to settle down into a collection tank. The sifter consists of a 30 cm long arrangement of steps, oriented with respect to each other at angles of 120°. An upward directed air flow (at 70 – 150 kPa overpressure) through the sifter prevents the collection of non-aggregated particles, forcing them to re-enter the fluidized bed. We also inspected the post-experiment particle bed within the process chamber, to determine whether any aggregates had survived within the fluidized bed.

II.3.2 Sample materials

In this mechanistic study of aggregation, we compared the behavior of two different materials. As an analogue material, we used spherical soda-lime glass beads (*Kremer Pigmente*, Germany, Table II.1) in three granulometries, with p_d of <50 µm (fine), 40-70 µm (medium) and 150-210 µm (coarse). The beads show high abrasion resistance with only 1.6 ± 0.1 % weight loss per 100 h of grinding, ensuring a negligible change in granulometry during experiments. As a natural material, we used phonolitic volcanic ash (LS) from the Laacher See eruption (East Eifel volcanic field, Germany), with p_d of <40 µm (fine), 40-90 µm (medium) and 90-300 µm (coarse). Although the ash is approximately 13 ka old and cannot be considered chemically pristine, we consider the deposition and evaporation of salt solutions on the ash materials to be a physical process acting only on particle surfaces; accordingly, the Laacher See ash is utilized as a proxy for the more complex surface morphology of volcanic ash, relative to the glass beads.

II.3.3 Salt-doping of ash materials

A H_2O-NaCl salt solution was selected for use in this experiment, in light of the extensive previous analysis of soluble salts on ash surfaces from multiple volcanoes via aqueous leaching, (see Witham et al., 2004; Ayris and Delmelle, 2012). These previous reviews noted that the most abundant elements in leachate solutions are Ca, Na, Mg, Cl and S, likely deriving from simple ionic sulphate and chloride salts (e.g., NaCl, $CaSO_4$).

The H_2O-NaCl solution, utilizing deionized H_2O, was sprayed at 7 $ml.min^{-1}$ into the process chamber and over the fluidized LS ash or glass bead beds. The process chamber temperature was maintained at 50 °C and the solution was sprayed at a nozzle pressure of 100 kPa. The particles in the fluidized bed were therefore coated with a thin liquid layer, which rapidly evaporated, precipitating NaCl on the particle surfaces. Particle aggregation during the

coating process was hindered by the low humidity of the heated atmosphere and slow spray rate of the solution. The efficiency of NaCl doping onto LS ash and glass beads was determined by comparison of the initial loading of NaCl dissolved into the sprayed solution, and the concentration on particle surfaces, which was determined by aqueous leaching. The leaching protocol utilized a solid:solution mass ratio of 1:10 and measured the effective NaCl concentration on particle surfaces via electrical conductivity measurements with an *inoLab Cond 730®*, manufactured by *Wissenschaftliche Technische Werkstätten GmbH*, Germany, calibrated using H_2O-NaCl solutions of known concentration.

The methods by which particles were coated with NaCl in the fluidized bed were both successful and reproducible. Twenty-five sub-samples were taken from a single NaCl-doping experiment and revealed a variation in NaCl concentration of less than 3 %. The efficiency of doping, based on comparison of the initial mass of NaCl sprayed onto the ash materials, and the mass determined from post-experiment leachate analysis, was on the order of 90 %. The loss likely reflects the loss of solution adhering to the internal surfaces of the process chamber.

Oxides	**Soda-lime glass beads (GB)**[a]	**Laacher See ash (LS)**[b]
SiO_2 (wt %)	72	54.4
Al_2O_3 (wt %)	*< 0.1*	20.1
Na_2O (wt %)	13	11.7
K_2O (wt %)	*< 0.1*	5.6
CaO (wt %)	9	1.1
Fe_2O_3 (wt %)	-	1.8
FeO (wt %)	-	0.47
MgO (wt %)	*< 0.1*	0.22
Specific surface area of granulometries[c]		
Fine	0.07 $m^2\ g^{-1}$	0.32 $m^2\ g^{-1}$
Medium	0.04 $m^2\ g^{-1}$	0.12 $m^2\ g^{-1}$
Coarse	0.02 $m^2\ g^{-1}$	0.07 $m^2\ g^{-1}$
Density	2,500 kg m^{-3} [a]	2,300 kg m^{-3} [d]

Table II.1:

[a] Bulk chemistry and density provided by *Kremer Pigmente GmbH*, Germany.

[b] Bulk chemistry data from Wörner and Schmincke (1984)

[c] Surface areas measured with *Camsizer® XT, Retsch GmbH*, Germany

[d] Density from ROTEC® GmbH & Co KG Rohstoff-Technik

II.3.4 Salt-doping of ash materials

A H_2O-NaCl salt solution was selected for use in this experiment, in light of the extensive previous analysis of soluble salts on ash surfaces from multiple volcanoes via aqueous leaching, (see Witham et al., 2004; Ayris and Delmelle, 2012). These previous reviews noted that the most abundant elements in leachate solutions are Ca, Na, Mg, Cl and S, likely deriving from simple ionic sulphate and chloride salts (e.g., NaCl, $CaSO_4$).

The H_2O-NaCl solution, utilizing de-ionized H_2O, was sprayed at 7 $ml.min^{-1}$ into the process chamber and over the fluidized LS ash or glass bead beds. The process chamber temperature was maintained at 50 °C and the solution was sprayed at a nozzle pressure of 100 kPa. The particles in the fluidized bed were therefore coated with a thin liquid layer, which rapidly evaporated, precipitating NaCl on the particle surfaces. Particle aggregation during the coating process was hindered by the low humidity of the heated atmosphere and slow spray rate of the solution. The efficiency of NaCl doping onto LS ash and glass beads was determined by comparison of the initial loading of NaCl dissolved into the sprayed solution, and the concentration on particle surfaces, which was determined by aqueous leaching. The leaching protocol utilized a solid:solution mass ratio of 1:10 and measured the effective NaCl concentration on particle surfaces via electrical conductivity measurements with an *inoLab Cond 730®*, manufactured by *Wissenschaftliche Technische Werkstätten GmbH*, Germany, calibrated using H_2O-NaCl solutions of known concentration.

The methods by which particles were coated with NaCl in the fluidized bed were both successful and reproducible. Twenty-five sub-samples were taken from a single NaCl-doping experiment and revealed a variation in NaCl concentration of less than 3 %. The efficiency of doping, based on comparison of the initial mass of NaCl sprayed onto the ash materials, and the mass determined from post-experiment leachate analysis, was on the order of 90 %. The loss likely reflects the loss of solution adhering to the internal surfaces of the process chamber.

II.3.5 Operational conditions

Our experiments were designed to (1) determine the critical concentration of NaCl and humidity needed to achieve artificial ash aggregation in a fluidized bed, (2) constrain the influence of particle size on aggregation efficiency under controlled conditions (process chamber humidity, temperature etc.), and (3) generate internal structures similar to structures in natural *AP* samples (Brown et al., 2012).

Optimal aggregation conditions for fluidized particles of different densities and grainsizes with respect to air temperature, nozzle pressure and air flow inside the process chamber were experimentally constrained. Each individual experiment utilized 1 kg of the

starting material and the inflow temperature T_{in} was set to 160 °C. This resulted in an average process chamber temperature T of 80 ± 15 °C, depending on the applied spray rate. For the aggregation experiment, nozzle pressure was set to 0.5 bar to allow larger water droplets to enter the fluidized bed, promoting the formation of a liquid film on solid particles within the fluidized bed. The airflow was set between 40 $m^3.h^{-1}$ and 80 $m^3.h^{-1}$, depending on particle size and type of material used. These conditions result in Reynolds numbers ranging between 8 and 28 for the ash experiments, applying eq II.1:

$$Re = \frac{D_p V_s \rho}{(1-\varepsilon)\mu} \qquad \text{(Equation II.1)}$$

where Re is Reynolds Number, D_p the equivalent spherical diameter of the particle, V_s the superficial velocity, ρ the density of the fluid, ε the void fraction of the bed and μ the dynamic viscosity of the fluid. The rising velocity of the air flow was 0.15 to 0.22 $m.s^{-1}$, approximately two orders of magnitude lower than natural plume rising speeds (Tournigand et al., 2015).

II.4 Results

A total of 37 experiments were carried out to study the effect of selected aggregation media (glass beads or LS ash), granulometry, NaCl concentration, and relative humidity on aggregate shape, structure and preservation. The incidence of aggregate preservation in each of these experiments is documented in Table II.2. As we observed no evidence for aggregate survival within the process chamber, we consider preservation to occur if aggregates were observed to enter the collection tank, rather than getting abraded and destroyed within the sifter. Notably, in all experiments where aggregation was recorded, aggregate arrival in the sifter was observed within a few seconds of the experiment onset.

II.4.1 Effect of NaCl loading

In our experiment, aggregation occurs independently of surface salt concentration; during initial experiments using untreated glass beads and LS ash, and relative humidities of 10 and 20 %, we observed the formation of aggregates (p_d < 1000 µm) which were destroyed within the sifter, rather than being preserved within the collection tank. The formation of stable aggregates which could be recovered from the collection tank could only be achieved using NaCl-coated glass bead and ash materials.

The minimum NaCl concentration required for recovery of aggregates comprised of glass beads with p_d < 50 µm was 1,800 ± 54 $mg.kg^{-1}$. For beads with initial p_d of 40-70 µm and 150-210 µm, the minimum NaCl concentration for recovery was 2,200 ± 66 $mg.kg^{-1}$. For LS

Material	Particle Diameter (µm)	Air flow [m³/h]	Temperature [°C]	NaCl (mg/kg)	Aggregate preservation Y/N
Soda-lime glass	<50	50	90	1221	N
Soda-lime glass	<50	50	90	1774	Y
Soda-lime glass	<50	50	90	5021	Y
Soda-lime glass	<50	50	91	20312	Y
Soda-lime glass	40-70	60	89	1143	N
Soda-lime glass	40-70	60	92	2241	Y
Soda-lime glass	40-70	60	90	30231	Y
Soda-lime glass	40-70	60	91	49183	Y
Soda-lime glass	40-70	60	90	51563	Y
Soda-lime glass	150-210	80	89	1014	N
Soda-lime glass	150-210	80	90	2189	Y
Soda-lime glass	<50 + 150-210	80	90	1970	Y
Soda-lime glass	<50 + 150-210	80	90	4081	Y
Soda-lime glass	<50 + 150-210	80	92	16832	Y
Laacher See Ash	<40	40	90	2354	N
Laacher See Ash	<40	40	90	4286	N
Laacher See Ash	<40	40	91	5081	Y
Laacher See Ash	<40	40	89	16021	Y
Laacher See Ash	<40	40	90	30185	Y
Laacher See Ash	40-90	50	90	256	N
Laacher See Ash	40-90	50	90	1578	N
Laacher See Ash	40-90	50	90	4012	N
Laacher See Ash	40-90	50	90	5214	Y
Laacher See Ash	40-90	50	91	10743	Y
Laacher See Ash	40-90	50	90	13800	Y
Laacher See Ash	40-90	50	88	15214	Y
Laacher See Ash	40-90	50	91	48069	Y
Laacher See Ash	40-90	50	90	43000	Y
Laacher See Ash	<90	50	90	4912	Y
Laacher See Ash	<90	50	91	15023	Y
Laacher See Ash	90-300	60	93	4943	N
Laacher See Ash	90-300	60	87	14156	Y
Laacher See Ash	90-300	60	90	20145	Y
Laacher See Ash	90-300	60	90	47890	Y
Laacher See Ash	90-300	60	90	49102	Y
Laacher See Ash	<300	70	92	5145	N
Laacher See Ash	<300	70	90	15103	Y
Laacher See Ash	<300	70	89	30861	Y

Table II.2: Summary of aggregation experiments carried out with the *ProCell® Lab*. Aggregation preservation is indicated as having occurred when (Y) when aggregates survived the impact into the collection tank.

ash, higher concentrations of NaCl were necessary for aggregate preservation within the sifter; approximately 5,000 ± 150 mg.kg^{-1} were needed to permit recovery of aggregates comprised of LS ash with p_d < 40 µm and < 90 µm. Significantly higher NaCl concentrations

were required when LS ash with p_d between 90 and 300 µm was used (15,103 ± 453 mg.kg^{-1}). Additionally, we qualitatively observed that increasing NaCl concentrations on particle surfaces increased aggregate recovery from the collection tank. In aggregation experiments using glass beads of all grain sizes, coated with NaCl loadings of 2,000 ± 60 mg.kg^{-1}, we observed that 50% of aggregates which entered the collection tank disaggregated upon impact with its base, while no similar breakup was observed using beads coated with NaCl concentrations of 50,000 ± 1500 mg.kg^{-1}.

The maximum diameter of aggregates formed during p_d < 50 µm glass bead experiments was one millimeter, an enlargement factor (EF) of 20 relative to the initial grain size, while aggregates comprised of 40-70 µm beads achieved an EF of 40. Notably, the EF for the 150 – 210 µm p_d fraction was approximately three; hence, the coarsest granulometry utilized in our experiments exhibited a limited capacity for aggregation, even at the highest NaCl concentrations. For the LS ash, much higher NaCl concentrations were necessary to achieve aggregation. The two ash fractions, fine and medium (p_d < 40 µm, 40 – 90 µm), required a minimum NaCl concentration of 5,000 ± 150 mg.kg^{-1} to aggregate with sufficient stability to survive the collection process. The large grained ash fraction (p_d < 300 µm) barely aggregated and required high NaCl concentrations (20,000 ± 600 mg.kg^{-1}) to sediment as aggregates in the collection vessel. The EFs are 25 for fine, 35 for medium and 2 for coarse particles, respectively.

II.4.2 Effect of granulometry

In both glass bead and LS ash materials, changes in the granulometry of the starting material did not affect the minimum concentration of NaCl needed to permit the recovery of stable aggregates (2000 ± 60 mg.kg^{-1} of NaCl for mixtures of glass beads with p_d of < 50 µm and 150-210 µm; 5,000 ± 390 mg.kg^{-1} NaCl for mixtures of LS ash with p_d of 40-90 µm and 90-300 µm, and 15,000 ± 450 mg.kg^{-1} for LS ash with p_d < 300 µm). Over a range of NaCl concentrations up to 50,000 ± 1,500 mg.kg^{-1}, we observed no effect on aggregation efficiency (mass of aggregates produced over time) in either material. However, changing granulometry did affect the shape of aggregates; with a narrow granulometry (e.g., p_d < 40 µm), aggregates were non-spherical, irregularly shaped and resembled un-structured particle clusters (*PC*), Fig. II.2a. Broadening the initial granulometry by mixing two particle populations (e.g., 50:50 mixtures of particles with p_d of 40-90 µm and 90-300 µm or < 40 µm and 40-90 µm) resulted in a transition in aggregate morphology from sub-spherical (Fig. II.2b) to spherical (Fig. II.2c).

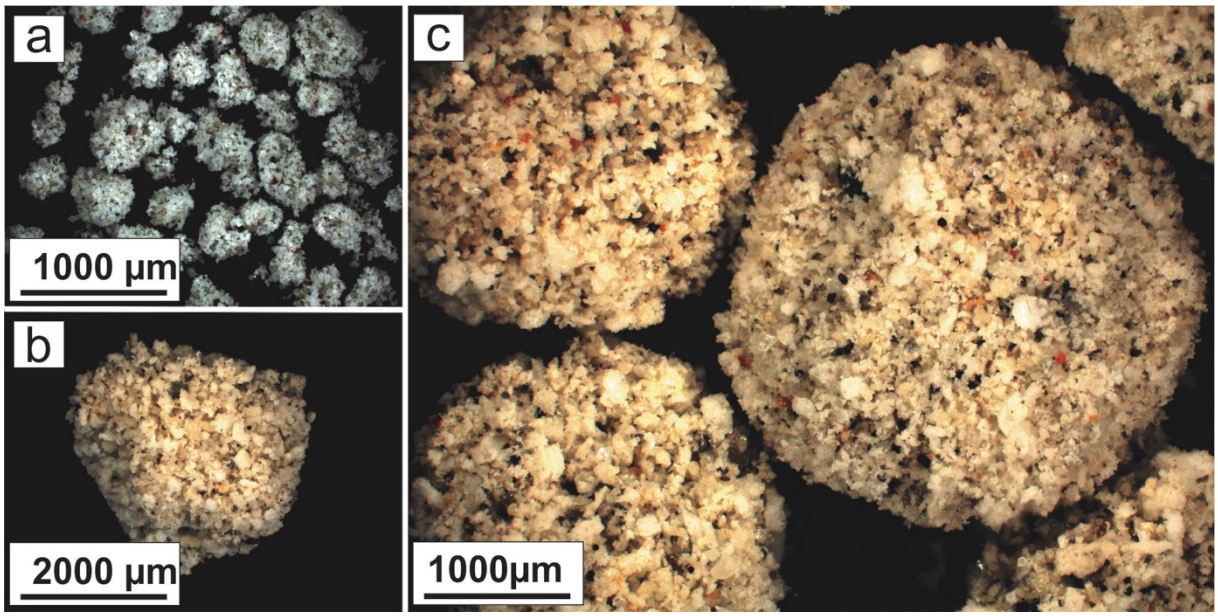

Figure II.2: a), b) and c) show the transformation of aggregate shape from angular to (sub-) spherical. a) shows aggregates that were produced from 40 – 90 µm LS ash. Broadening the granulometry to p_d of 40–300 µm (b), aggregates become sub-spherical. Adding a fine fraction (p_d < 40 µm) produces spherical aggregates (c). All images were produced using reflected light microscopy.

Fluidized beds comprised of glass beads with p_d of < 50 µm and 150-210 µm produced aggregates with accumulations of coarse particles (p_d > 150 µm) in their core and fine particles in their rims (Fig. II.3a). Additionally, solid NaCl bridges were clearly visible connecting particles with each other (Fig. II.3b).

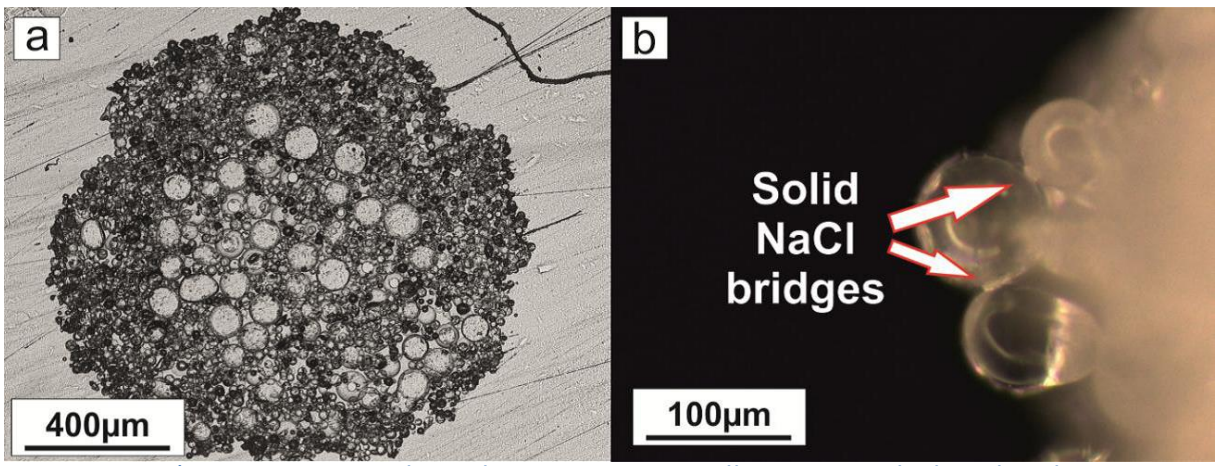

Figure II.3: a) Cross section through an experimentally generated glass bead aggregate, produced after impregnating with epoxy resin. The starting granulometry in the experiment consisted of particles with p_d < 50 µm and p_d = 150-210 µm glass beads. Coarse glass beads are predominantly found in the core region, while fine particles are principally located on the outside of the aggregate. b) Image showing solid NaCl bridges connecting glass beads (p_d = 40-70 µm) of an aggregate. All images were produced using reflected light microscopy.

Similarly, for LS ash aggregates, internal structuring was enhanced by broadening the starting granulometry (Fig. II.4); while a separation between core and rim was not readily observed in aggregates comprised of LS ash with p_d < 40 µm (Fig. II.4a), the cores became coarser grained than the rims for aggregation experiments using LS ash with p_d < 90 µm (Fig. II.4b) and p_d < 300 µm (Fig. II.4c).

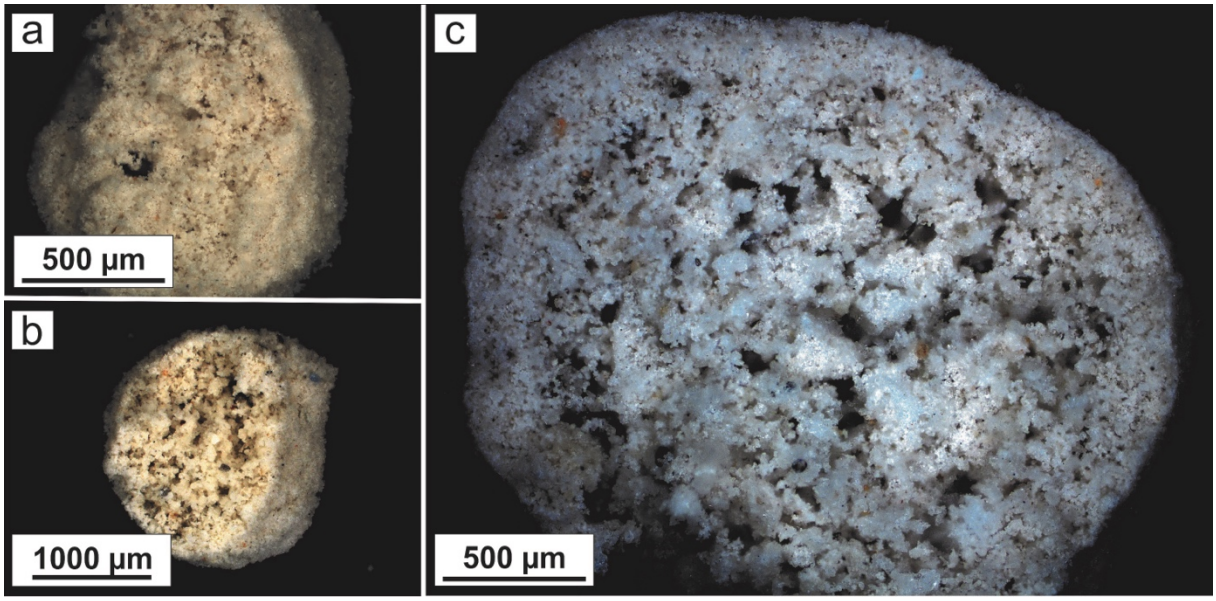

Figure II.4: a) – c) Cross sections showing the increasing evidence of internal aggregate structuring depending on the starting granulometry; a) consists of LS ash with p_d < 40 µm – internal stratification is not detected. b) consists of LS ash with p_d < 90 µm and c) of LS ash with p_d < 300 µm. In c), coarse grained particles (p_d > 100 µm) are concentrated in the center whereas fine grained particles are densely packed in the rim of the aggregate. All images were produced using reflected light microscopy.

II.4.3 Effect of humidity

The effect of humidity on aggregation preservation was also measured (Fig. II.5). As no influences on aggregate recovery other than of surface area were implied from previous experiments on glass beads and LS ash, we confined our investigation of humidity to one material only (LS ash). We performed three experimental series utilizing NaCl loadings of 15,000 ± 450 mg.kg^{-1} on i) LS ash with p_d < 40 µm, ii) LS ash with p_d 40-90 µm, and iii) a 50/50 ratio of these two granulometries. Changing the relative humidity of the air within the system changed the rate of aggregate production. Aggregation initiated, depending on the starting granulometry, between 12 and 18 % RH. The number of aggregates produced per minute increased exponentially up to 45 % RH. Most aggregates are produced when the grain size distribution of the starting material is broad (50/50 mix of LS ash with p_d < 40 µm and 40-90 µm). The lowest production rate of aggregates is achieved by particles with p_d of 40-90 µm, used in isolation. These data evidence a significant control of humidity on aggregation rate.

The upward directed airflow within the sifter dried the aggregates during transit, such that residual internal moistures were below 1 wt. %. However, at approximately 50 % RH, the upward directed airflow in the sifter was insufficient to dry aggregates, resulting in the accumulation of a heap of wet ash in the collection tank, rather than dry, coherent aggregates.

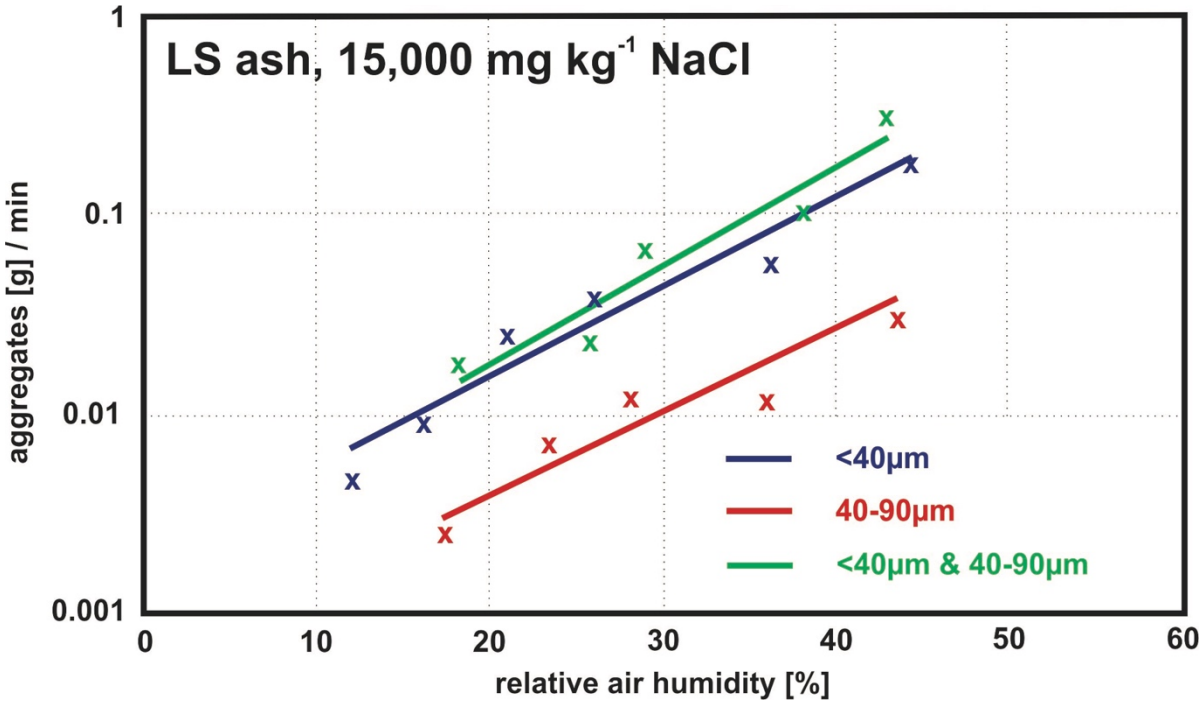

Figure II.5: The influence of humidity on mass production of preserved aggregates [g] per minute is shown for various granulometries. The highest rate of aggregate production is demonstrated when using a broad granulometry of starting material (p_d < 40 and 40-90 µm), followed by the p_d < 40 µm and the p_d 40-90 µm charge. NaCl concentration is at 15,000 mg.kg^{-1}.

II.5 Discussion

II.5.1 Agreement with previous studies

During our experiments, we observed the formation of aggregates with clear internal structuring. LS aggregates from initial materials with p_d < 300 µm, have a modal p_d of 63 µm over the whole particle, but within their rims, the modal p_d is 12 µm. These aggregates show many similarities with *AP2* aggregates found in nature; in studies of natural ash aggregates, the dominant particle size fraction (90 vol. %) has p_d < 60 µm, while the largest particles found in natural aggregates have p_d of ~200-500 µm (Sheridan and Wohletz, 1983; Cole et al., 2001; Bonadonna et al., 2002; Trusdell et al., 2005; Cunningham and Beard, 2014; Scolamacchia and Dingwell, 2014). Within internally structured natural ash aggregates, coarser particles are

enriched in the core, while finer particles comprise the rim (Brown et al., 2012). For example, Scolamacchia and Dingwell (2014) analyzed ash aggregates from the 1982 El Chichon eruption (Mexico); the cores of these aggregates consisted of coarser material (p_d = 63-250 µm) while their rims contained finer-grained particles (p_d < 63 µm) with ~75 % of rim grains smaller than 16 µm in diameter. In addition to their structural similarities, the aggregates formed in our experiments exhibit comparable densities to natural samples; the density of the experimental aggregates (480 kg.m^{-3}) is within the range of values reported for ash aggregates recovered by Taddeucci et al. (2011) from the 2010 Eyjafjallajökull eruption (100 to 1,000 kg.m^{-3}).

Our experiments are also in good agreement with previous studies which identify liquid bonding as a primary control on the formation of AP aggregates. We observed a clear dependency of aggregate accumulation rate in the collection tank on RH, with an exponential increase between 12 and 45 % RH (5-19 wt. % H_2O at 90 °C). At lower values, no aggregates were observed in the sifter. At higher humidity, overwetted aggregates coalesced in the collection tank and formed a heap of wet ash (Fig. II.5). The range of humidity values observed is in good agreement with natural observations and other experimental studies; Tomita et al. (1985) observed pellet fallout during eruptions at Sakurajima Volcano (Japan) and described ash aggregation solely on days with RH of > 18 % at a height of 4 km, corresponding to the maximum plume height. In laboratory experiments, Schumacher and Schmincke (1995) determined that the optimum quantity of water to promote aggregation of ash within a pan was between 15-25 wt. %. In similar experiments, utilizing a vibratory pan, Van Eaton et al. (2012) determined that aggregation was most efficient at liquid concentrations between 10-15 wt. %, while at higher concentrations, slurries rather than aggregates, were formed. Based on the good agreement of our experimental data and previous studies, we conclude that the concentration of liquids during aggregation controls the number of particle aggregates produced; with increasing liquid binder concentration, aggregate production increases exponentially (Fig. II.5).

The process of cementation of aggregates has been described several times for natural deposits, invoking the role of salts as binding agents, but quantification of the related process has not yet been achieved. In our study, although we observed aggregation under all conditions, including NaCl-free particles, we required high NaCl loadings (> 5,000 mg.kg^{-1}) to permit recovery of stable ash aggregates from the collection tank. Higher loadings of NaCl were required to promote recovery of LS ash aggregates, compared to that required for glass bead aggregates. This likely reflects the complex morphology, and accordingly, greater surface area, of the LS ash (Table II.1); to achieve the same salt loading per unit surface area required a greater dose of salts per unit mass in the LS ash, relative to the glass beads. It is not yet known whether the behavior of NaCl is salt-specific, or applicable to all soluble salts on ash

surfaces. If the latter, it is notable that the total loading of soluble salts utilized in this study, while high, remain within the range of concentrations implied by previous leachate studies: data summarized by Ayris and Delmelle (2012) yielded both a calculated mean and median sulphate and chloride salt loading on the order of 6,000 mg.kg^{-1}, with maximum values in excess of 20,000 mg.kg^{-1} being reported in some scenarios. Additionally, preparatory to the current study, we disaggregated and subsequently leached fragile accretionary pellets recovered from deposits of the 2011 dome collapse at Soufrière Hills Volcano (Montserrat). The total concentration of Ca, Cl, Mg, Na and S in leachate solutions (1:100 ash: water ratio, 4 hour leaching time), indicative of total surface salt loading, was in excess of 5,000 mg.kg^{-1}.

II.5.2 A new perspective on ash aggregate formation

Our findings have demonstrated that experiments utilizing fluidization bed techniques can produce aggregates of comparable structure and under comparable conditions to those previously observed both in experimental studies and field investigations. Crucially, this realization of comparability opens a new avenue of research in the application of existing industrial studies to volcanic systems.

Ennis et al. (1991) have previously described a particle coalescence model, which can be utilized to explain our experimental results, and by analogy, the formation of ash aggregates during explosive eruptions. The model is based on the assumption that two approaching particles with a liquid film layer (Fig. II.6a) of thickness *h* coalesce after collision, when the initial kinetic energy is dissipated through viscous and elastic losses. Liquid layers of the two particles will have first contact at a distance *2h*. Viscous losses are calculated by using results for Stokes flow between two approaching particles. The coefficient of restitution *e* dissipates energy within the solid phase. Resulting calculations show that particles will coalesce when the viscous Stokes number St_v (eq. II.2) is less than some critical viscous Stokes number St_v^* (eq. II.3):

$$St_v = \frac{4\rho u_0 p_d}{9\mu} \qquad \text{(Equation II.2)}$$

$$St_v^* = \left(1 + \frac{1}{e}\right) \ln\left(\frac{h}{h_a}\right) \qquad \text{(Equation II.3)}$$

where ρ is the particle or aggregate density, u_0 is half the initial relative velocity of the impact, p_d is the particle or aggregate diameter, μ is the liquid viscosity and h_a is the characteristic height of surface asperities. St_v describes the ratio of initial kinetic energy to energy dissipated by viscous effects. St_v will increase during the aggregation process since the aggregate grows.

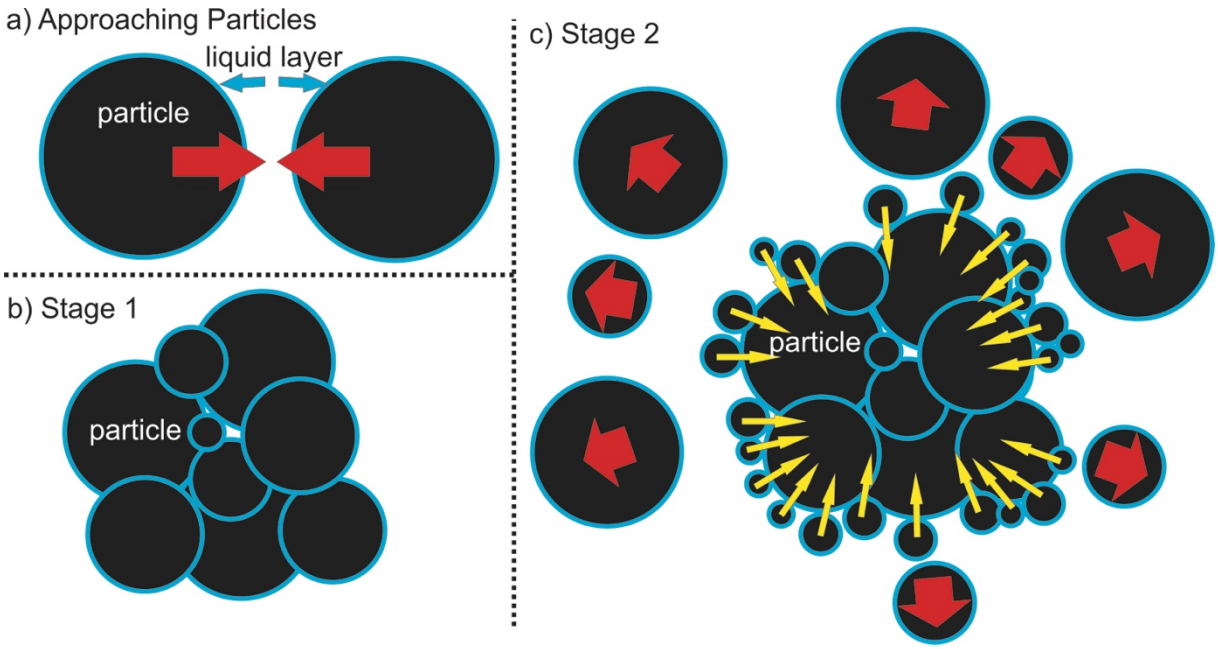

Figure II.6: Illustration of the Ennis et al. (1991) model: in a) two particles with a liquid layer of the thickness *h* are approaching each other. b) reflects the non-inertial regime of aggregate growth in which all particles stick after collision due to viscous and elastic forces sufficiently dissipating kinetic collision energies. c) shows the inertial regime, where aggregate growth in which viscous Stokes number and critical viscous Stokes number are approximately equal. Small particles stick to the existing aggregate due to lower collision energies. Large particles rebound due to higher collision energies; rebound forces cannot be dissipated by liquid bonding forces. The non-inertial regime builds the core of an accretionary pellet, reflecting the total particle size range, while the inertial regime builds up the fine grained rim.

The interplay of the various parameters in this theoretical model allow for the constraint of three granulation stages which describe the growth of both experimental and natural accretionary pellets. After Ennis et al. (1991), the first stage is referred to as the non-inertial regime ($St_v << St_v^*$), where collisions between particles of all sizes are successful (Fig. II.6b). In this stage, a large range of particle sizes will stick together (e.g. p_d <300 µm in the ProCell® Lab experiments), producing a coarse-grained (reflecting the whole size range of available particles), porous core. In the second granulation stage (inertial regime), the viscous Stokes number St_v is approximately equal to the critical Stokes number St_v^*. Coalescence now depends on the size of colliding particles, whereby collisions between two small, or one small and one large particle(s), keeps St_v low and enables coalescence, while collisions between two big particles, e.g. an aggregate and a large ash grain, causes high St_v and hinders coalescence. In the inertial regime, only smaller particles will stick to existing aggregates due to the increasing difference in diameter, the likelihood of increasing impact velocities, and the increasing St_v number (Fig. II.6c). In the third granulation stage, St_v is greater than St_v^* and collisions do not permit coalescence. In this generalized model, the initial particle size distribution is likely an important control; with a narrow granulometry, any aggregate structuring effects imparted during the different regimes are likely minimal, producing a

poorly structured ash pellet (*AP1*). In contrast, with a broader initial particle size distribution, aggregate growth would produce an internally structured clast with a dense, fine-grained rim (*AP2*). It is also possible that pre-inertial regime interruption of aggregation processes via sedimentation into particle-poor environments could favour the formation of *AP1*, rather than *AP2* aggregates.

The Ennis model (1991) can also explain the increasing rate of aggregation with increasing air humidity, prior to overwetting (Fig II.5). The increasing quantity of liquid sprayed into the process chamber increases the liquid layer thickness *h* on single particles; in our experiments using LS ash with p_d < 40 µm, increasing RH from 12 to 45 % is calculated to increase *h* from 160 to 590 nm. Increasing *h* values increase St_v^*, allowing more particles to coalesce, and increasing the rate of aggregate production. The initiation of aggregation at lower humidity for fine grain sizes (Fig. II.5) can also be explained; smaller particle diameters, p_d, result in lower impact velocities u_0 and an overall smaller St_v, another criterion for enhanced aggregation. A further implication for liquid bonding from the Ennis model (1991) is a dependence on liquid viscosity; while our experiments used only deionized water, the condensation or emplacement of fluids of different viscosities (e.g., liquid sulphur, Scolamacchia and Dingwell, 2014) on ash surfaces may significantly influence aggregation processes.

Observations from our experiments offer a number of further insights into the formation of *AP* aggregates. The arrival of aggregates within the collection tank at the start of the experiment was near-instantaneous; this suggests that the rims of *AP* aggregates, rather than being formed by transport through a finer-grained particle suspension than that from which the core was constructed, can formed rapidly from the same particle population that builds the initial core via a selective aggregation process. The fragility of salt-free or salt-poor aggregates in our experiments further suggests that a continuous cycle of collisions, aggregation and disaggregation may occur in eruption plumes and PDCs, but that once specific boundary conditions are achieved, rapid growth of structured aggregates is possible. The low experimental Reynolds numbers of our study (8-28), relative to those of e.g., PDCs (10^6-10^9, e.g. Andrews and Manga, 2012) suggests that one environment where these conditions are achieved could be the most dilute parts of PDCs, lofted co-pyroclastic plumes or the umbrella regions of eruption plumes. However, such conditions are unlikely to be the only regimes where aggregate growth is promoted.

Given the apparent fragility of many of the aggregates formed in our experiments, the capacity of *AP* aggregates to survive deposition and be preserved within a deposit likely requires the establishment of strong interparticle bridges to strengthen it. This may be

particularly important if the aggregate traverses a more energetic region of an eruption plume or PDC after formation but prior to deposition. Salt-driven cementing would require not only an abundance of pre-existing soluble salts, but also rapid drying after formation. This was illustrated in our experiments; the lower humidity within the sifter promoted liquid evaporation and salt precipitation, but the absence of aggregates in the post-experiment process tank suggests that fluidized bed collapse in still-humid conditions prevented drying and favored aggregate breakup. Within volcanic settings, lower humidity conditions could be achieved via numerous mechanisms, e.g., by sedimentation into drier atmospheres from a water-rich plume, or the recycling of aggregates from cold regions of the plume and/or PDC into hotter regions (>100°C). Thus, much as there may be multiple environments where aggregate growth is favored, there may be multiple conditions where salt-driven cementing may stabilize those aggregates.

II.6 Conclusion

Accretionary pellets were produced successfully in the laboratory by using fluidization bed techniques. Liquid bonding forces promoted particle adhesion following collisions, building aggregates up to 1000 µm in size. These aggregates were fragile and were easily disaggregated, but when the initial particle mass was coated with NaCl, could be stabilized by the dissolution and re-precipitation of NaCl as solid interparticle bridges. High, but volcanically relevant (~2,000 $mg.kg^{-1}$) concentrations of surface salts enabled recovery of some aggregated particles, while increasing salt loads promoted increased stability and improved aggregate preservation. The granulometry of the initial particle mass had a strong influence on the growth and structure of aggregates; fine-grained particles (p_d <100 µm) grew up to 40 times larger than the original diameter of the starting material, while coarse particles reached final diameters of only three times that of the initial particle. Similar to the results of previous field studies and experimental observations, aggregate formation occurred within a discrete range of humidities; in our experiment, aggregates formed above 12 % RH, and disaggregated into a mud or slurry at humidities greater than 45 % RH.

Most notably, through the use of particle populations with broad granulometries, we generated (sub-) spherical and internally structured aggregates with coarse grained cores and fine grained rims, similar to natural *AP2* aggregates observed in volcanic deposits. Applying a numerical model derived from industrial particle aggregation studies, we conclude that shape and internal structuring of aggregates is controlled by the initial granulometry, mediated by a fast-acting selective aggregation process. In so doing, we offer a generalized model for the formation of both *AP1* and *AP2* aggregates, which also identifies the importance of the concentration, and perhaps viscosity, of the liquid binding agent which facilitates aggregation. Our findings suggest that aggregation and disaggregation processes occur in all volcanic

environments, but that once specific boundary conditions are achieved, growth of *AP* aggregates is rapid. To preserve these aggregates upon deposition may further require a high loading of pre-existing surface salts, and a pre-deposition transition from a high to low humidity environment. Although further constraints on the parameters which drive both aggregation and cementation are required, the findings of this paper should be considered as a valuable input into numerical aggregation and ash dispersal models.

II.7 Acknowledgements:

We thank Ulrich Walter, Melanie Guttzeit and Katja Oppermann for their help during the fluidized bed experiments at Glatt Industries. We thank Corrado Cimarelli, Jacopo Taddeucci, Stefano Alois and Costanza Bonadonna for fruitful discussions. The Laacher See ash used in this study was kindly offered by ROTEC GmbH & Co. KG (Mühlheim-Kärlich, Germany). This work is supported by the Marie Curie Initial Training Network 'VERTIGO', funded through the European Seventh Framework Program (FP7 2007-2013) under Grant Agreement number 607905. P.A. and D.B.D. acknowledge the support of European Research Council Advanced Grant 247076 "EVOKES" (Explosive volcanism in the Earth System). This manuscript benefitted from constructive comments of Stephen J. Lane, Sebastian Watt and the editor Tamsin A. Mather.

Chapter III

Ash aggregation enhanced by deposition and redistribution of salt on the surface of volcanic ash in eruption plumes

Ash aggregation enhanced by deposition and redistribution of salt on the surface of volcanic ash in eruption plumes

Sebastian B. Mueller (1), Paul M. Ayris, (1), Fabian B. Wadsworth (1), Ulrich Kueppers (1), Ana Silvia Casas (1), Pierre Delmelle (2), Jacopo Taddeucci (3), Michael Jacob, (4), Donald B. Dingwell, (1)

(1) Ludwig-Maximilians-Universität München (LMU), Earth and Environmental Sciences, Munich, Germany

(2) Université catholique de Louvain, Earth and Life Institute, Louvain-La-Neuve, Belgium

(3) Istituto Nazionale di Geofisica e Vulcanologia, Rome, Italy

(4) Glatt Ingenieurtechnik GmbH, Verfahrenstechnik, Weimar, Germany

Scientific Reports 7:45762 (2017)

III.1 Abstract

Interactions with volcanic gases in eruption plumes produce soluble salt deposits on the surface of volcanic ash. While it has long been postulated that saturation-driven precipitation following the dissolution of ash surfaces by condensed acidic liquids is a primary mechanism of salt formation during an eruption, it is only recently that this mechanism has been subjected to detailed study. Here we spray water and HCl droplets into a suspension of salt-doped synthetic glass or volcanic ash particles, and produce aggregates. Deposition of acidic liquid droplets on ash particles promotes dissolution of existing salts and leaches cations from the underlying material surface. The flow of liquid, due to capillary forces, will be directed to particle-particle contact points where subsequent precipitation of salts will cement the aggregate. Our data suggest that volcanically-relevant loads of surface salts can be produced by acid condensation in eruptive settings. Several minor and trace elements mobilized by surface dissolution are biologically-relevant; areas with aggregation-mediated ash fallout could be “hotspots” for these elements on deposited ash. The role of liquids in re-distributing surface salts and cementing ash aggregates also offers further insight into the mechanisms which preserve well-structured aggregates in some ash deposits.

III.2 Introduction

The fast release of over fifty different major, minor and trace elements from volcanic ash on contact with water has historically been attributed to the presence of soluble surface salts (Witham et al., 2004). These salts have environmental relevance in terrestrial and aquatic systems, and may alter the chemical reactivity of volcanic ash in the atmosphere (Ayris and Delmelle, 2012). Soluble salts may also play an important role in the cementation of ash aggregates (Gilbert and Lane, 1994; Mueller et al., 2016), and thus may influence ash sedimentation rates, ash dispersal, and deposit properties. Investigating the various mechanisms of gas-ash interactions which emplace soluble salts therefore offers insight into the physical (e.g., deposit thickness distributions) and chemical effects of ash on the natural and human environments. In the last decade, several studies have investigated the formation of salts via adsorption of volcanic gases (SO_2, HCl, HF) on ash surfaces at temperatures ranging from magmatic to atmospheric (Ayris et al., 2014; Hoshyaripour et al., 2012; Oskarsson, 1980). However, recent numerical studies (Hoshyaripour et al., 2014) have also examined other mechanisms of salt formation, such as the condensation of acidic liquid droplets onto ash surfaces (Rose, 1977). During transport in eruption plumes and pyroclastic density currents at elevated temperature and cold volcanic clouds at ambient temperature, the surface of volcanic ash particles may become partially or fully coated with liquid droplets (Delmelle et al., 2005; Lathem et al., 2011). These liquid droplets can be formed by condensation of volcanogenic acid solutions of HCl, HF or H_2SO_4 (Oskarsson, 1980; Rose, 1977), and can be highly acidic; in simulations (Textor et al., 2003) using the *Active Tracer High Resolution Atmospheric Model* (ATHAM), HCl dissolved into suspended water droplets achieved concentrations of 0.1-10 M during the first hour after an eruption. Acidic liquid droplets condensing onto the ash surface will dissolve its glass and mineral constituents, as well as any pre-existing soluble salts (Hoshyaripour et al., 2014). Upon subsequent evaporation, sulphate and halide salts may become saturated in the condensed liquid and precipitate or re-precipitate. As suspended ash particles traverse an array of temperature, humidity and chemical regimes, the chemistry and volume of the liquid film, and consequently, the solubility of different surface deposits, may fluctuate; accordingly, salt assemblages on post-depositional ash surfaces may be the product of repeated cycles of dissolution and precipitation.

The variables and processes which govern the formation and evolution of liquid droplets and coatings on ash surfaces are difficult to monitor in-situ, and reconstruction of syn- or post-eruptive processing of ash surfaces cannot be easily obtained from post-depositional characterization. While characterization of ash surfaces (Delmelle et al., 2007; Maters et al., 2016) or analysis of spatial variations in leachate chemistry and ash deposit

properties (Ayris et al., 2015) offer detailed insights, targeted experimental work is necessary for the discrimination of possible mechanisms. Here, we investigate the process of liquid film development and salt formation and re-precipitation on ash surfaces directly, using dispersed aqueous solutions in fluidised particle mass comprised of salt-doped natural volcanic ash and synthetic glass bead materials. These findings confirm that acid-condensation-driven surface dissolution is a key mechanism for rapid, large salt formation which has a clear relevance to ash aggregation and both in-plume and atmospheric processing of ash surfaces. Our results offer insight into the conditions which may dictate volcanic ash deposition and their chemical impacts.

III.3 Material and methods

We use two granular materials with particle diameters of < 90 µm; (1) synthetic spherical soda-lime silicate glass beads from *Kremer Pigmente* as a synthetic analogue material with well-constrained chemistry, density and surface area, and (2) phonolitic ash as a natural analogue with irregular surface roughness and intra-particle porosity, quarried from pyroclastic deposits from the lower unit of the 13 ka Laacher See eruption (East Eifel volcanic field, Germany (Wörner and Schmincke, 1984), see Table III.1).

The particles were loaded in a fluidised bed system (*ProCell® Lab System*, *Glatt Ingenieurtechnik GmbH*) (1) initially to dope the surfaces with soluble salt (NaCl), and (2) subsequently to expose them to turbulent liquid (de-ionized H_2O or HCl) spraying (see also Data Repository and Mueller et al. (2016) for fluidized bed design). The ProCell® Lab suspends a granular particle mixture within an upwardly directed gas stream under controlled temperature, bulk turbulence and humidity conditions, generating a fluidised bed when the drag forces exerted by the gas stream exceed the weight of the particles (Salman et al., 2006). Through a nozzle, liquid droplets (at controlled composition, size and temperature) have been added to the fluidised bed and deposited on the particle surfaces.

In step (1) we sprayed variably concentrated NaCl-H_2O brine at a rate of 7 ml.min^{-1} at 50 °C using a nozzle pressure of 100 kPa. Thereby, we coated the particles with droplets or a film from which, upon evaporation, salt crystals precipitated. The salts were identified as halite (NaCl) crystals using energy dispersive x-ray (EDX) spot analysis and mapping associated with scanning electron microscopy (SEM, Fig. III.1). SEM analysis was performed at the HP-HT lab of *INGV Roma*. Initial doping was performed to provide a salt source for remobilization in step (2) because in natural plume environments rapid salt formation after fragmentation is common before a more protracted trajectory down-plume (Ayris et al., 2013). Effective halite loads were determined from conductivity measurements with an *inoLab Cond 730®*, manufactured by *Wissenschaftliche Technische Werkstätten GmbH*, Germany (calibrated

using H_2O-NaCl solutions of known concentration) and were found to be 19-248 and 31-329 mmol.kg^{-1} for the glass bead and volcanic ash materials, respectively (Supplementary Table III.S1). These halite loads are higher than the average median reported from natural ash samples (see Supplementary Material III.11); this granted the artificial aggregates a higher preservation rate and made aggregate production much more time-efficient. However, it was shown that artificial ash aggregation is also possible with lower halite loads such as reported in the global median of ash leachates (Mueller et al., 2016).

During step (2), we sprayed 250 ml of de-ionized H_2O or 12 M HCl solution (at a rate of 40 ml.min^{-1}) into a fluidised bed of glass bead or volcanic ash samples. Also during step (2), in an additional experiment, we sprayed the volcanic ash materials doped with 251 ± 13 mmol.kg^{-1} of halite with 250 ml of 0-12M HCl solution at a rate of 40 ml.min^{-1}. In all experiments, nozzle pressure was 50 kPa to allow µm-sized droplets to be produced, leading to the formation of liquid coatings on solid particles. The inlet air flux was set to 0.01–0.02 m^3.s^{-1}, depending on particle size and type of material used, and the average process chamber temperature of 40 ± 15 °C, depending on the applied spray rate. Aggregation of particles was observed after no more than 10 seconds for both experiment types.

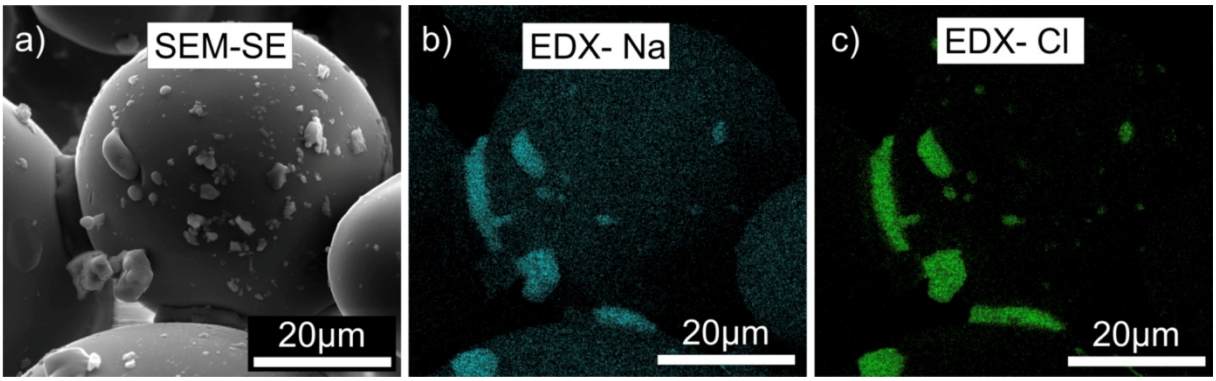

Figure III.1: EDX mapping of soda-lime glass bead aggregates. a) shows a secondary electron (SE) image of the mapping area. b) highlights Na and c) Cl content which, in combination with a), can be identified as NaCl crystals sitting on glass bead surfaces and in connection points of glass beads as a cementing agent.

We conducted all subsequent analysis on experimentally generated aggregates. Aqueous leaching was used to characterize pre- and post-experiment surface salt loading. Aggregates were immersed in deionized water for one hour at a solid-solution mass ratio of 1:250, and the concentrations of Al, Ca, Cl, Fe, K, Mg, Mn and Si in solution measured following analytical protocols (Ayris et al., 2014). However, Fe data were subsequently discarded as the possibility of Fe contamination from the corrosion of the stainless-steel tank walls could not be discounted. The granulometry of selected samples was determined using a *Coulter LS-230* laser diffraction particle size analyzer (*Fraunhofer optical model*, imaginary/real refractive

indices of 0.001/1.52 for glass beads and 0.1/1.52 for volcanic ash). The specific surface area measurements were made on selected samples by application of the *Brunauer-Emmett-Teller* (BET) theory to argon adsorption measurements conducted at -196 °C using a *Micrometrics Gemini 1303* surface area analyzer. Selected aggregates were analyzed by FEG-SEM using a *JEOL JSM 6500* field emission scanning electron microscope to investigate the morphology and chemistry of the surface deposits formed during the experiments.

Bulk chemistry (wt. %)	**SLS$_a$**	**PHN$_b$**
SiO_2 (wt. %)	72	56.2
TiO_2 (wt. %)	–	0.2
Al_2O_3 (wt. %)	*< 0.1*	20.6
Fe_2O_3 (wt. %)	–	1.5
FeO (wt. %)	–	0.6
MnO (wt. %)	–	0.30
MgO (wt. %)	*< 0.1*	0.15
CaO (wt. %)	9	1.1
Na_2O (wt. %)	13	9.4
K_2O (wt. %)	*< 0.1*	5.9

Table III.1:

[a] Bulk chemistry provided by *Kremer Pigmente GmbH*, Germany.

[b] Bulk chemistry data averaged from lower- and middle- units of Laacher See deposits, from Wörner and Schmincke (1984).

III.4 Results

When exposed to HCl solutions of varying concentration, volcanic ash and synthetic glass bead particles undergo dissolution of (1) pre-existing surface salts and (2) the underlying surface. The initial halite doping process produced discrete crystals or clusters of crystals which are evenly dispersed across the material surfaces (Fig III.2a). However, after spraying during turbulent experiments, the distribution and morphologies of surface halite are modified from those produced by the initial doping. When water is used as the sprayed liquid phase, we show that a combination of discrete euhedral and anhedral halite crystals (see Supplementary Material III.11) are preserved on the glass bead surfaces (Fig III.2b), some of which are several 10s µm in size. These are clustered around particle-particle contact points. If a particle broke off after the cementation process, isolated ring structures were left behind, indicating the former position of an adhering particle. When 12M HCl is used as the liquid phase for glass bead materials both without (Fig III.2c) and with (Fig III.2d) a pre-existing halite load, we observe similar structures in addition to extensive patchy regions of sub-micron sized nodules

on the surface of ash particles and mega-crystals of halite (Fig III.2e). When volcanic ash is used, the smaller starting grain size distribution (see Supplementary Material III.11) and more complex and irregular morphology precludes the formation of large halite assemblages, and instead, smaller (< 5 µm) halite deposits and sub-micron nodules cluster in cavities, cracks and other favorable topographic features (Fig III.2f). These features were observed in all volcanic ash samples analyzed, irrespective of the concentration of the applied HCl solution.

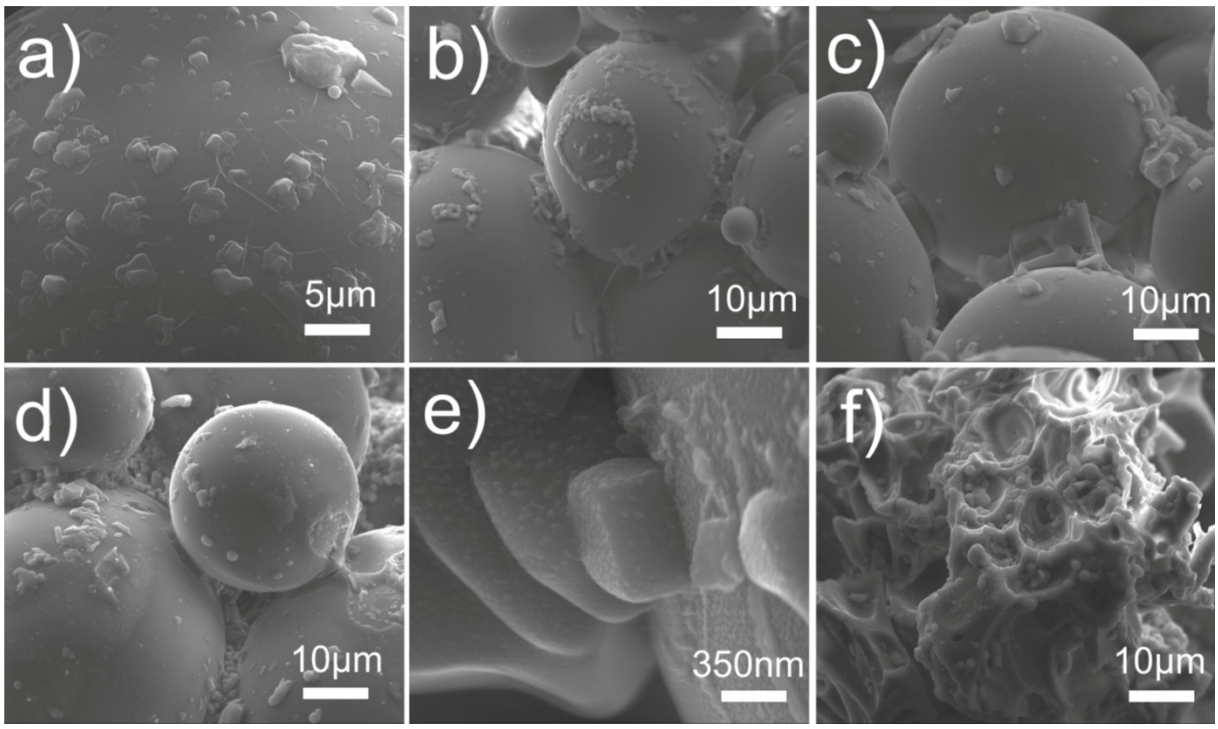

Figure III.2: SEM images of experimental particles after (a) halite doped glass bead materials produced in experimental step 1, (b) halite doped glass bead materials after spraying with deionized water, (c) un-doped glass bead materials after spraying with 12 M HCl, (d) halite doped glass bead materials after spraying with 12 M HCl, (e) surface nodules on halite doped glass bead materials after spraying with 12 M HCl, and (f) halite doped volcanic ash materials after spraying with 12 M HCl.

For the glass bead materials, analytical leachates are dominated by Na and Cl (60-139 mmol.kg^{-1}) with minor quantities (1-6 mmol.kg^{-1}) of Ca and Si, while all other elements were present in concentrations below 1 mmol.kg^{-1}. The ratio of soluble Na in leachate solutions, termed Na_s (where a subscript s denotes a measured soluble cation concentration throughout), to soluble Cl_s is approximately 1, while the ratio of Na_s to the sodium content we would predict from the known pre-existing halite load on the initial material, termed Na_p (where a subscript p denotes the predicted soluble concentration), decreases from 3.8 to 0.4 as the pre-doped applied halite load increases. Analytical leachates from the volcanic ash materials after exposure to HCl are similarly dominated by Na and Cl (206-1,308 mmol.kg^{-1}). Unlike the glass bead materials, the ratio of Na_s to Cl_s in 12 M HCl experiments is 0.4 ± 0.2,

and increases from 0.4 to 0.9 with decreasing HCl concentration from concentrations of 12 M to 0.7 M. The ratio $\mathrm{Na}_s/\mathrm{Na}_p$ decreases from 6.6 to 1.9 as the applied halite load increases, and is approximately 1.5 ± 0.5 for the aggregates formed under varying HCl concentrations. This can be attributed to the decreasing proportional significance of Na extracted from the material surface by HCl dissolution, as the magnitude of the pre-existing halite load increases. Further, the differences in the absolute values of the $\mathrm{Na}_s/\mathrm{Na}_p$ ratios between the two materials are attributable to the incorporation of particles of particular grain size into the final aggregates. For example, for the glass bead material, $\mathrm{Na}_s/\mathrm{Na}_p$ decreases below unity, implying that per unit mass there is less NaCl present in the final aggregates than cumulatively on the surface of loose glass beads. This is possibly attributed to the slightly lower content of fine particles in the aggregates relative to the starting material. The reason for this observation is not clear yet. In contrast, the volcanic ash aggregates show a finer mode than the starting loose ash and exhibit $\mathrm{Na}_s/\mathrm{Na}_p$ ratios greater than unity; this is likely attributable to the contribution of Na mobilized by ash surface dissolution to the pre-existing halite load. These findings can also be shown by estimates of geometric specific surface area (SSA_{geo}), which were calculated from application of a spherical approximation to the particle size distributions of the aggregate materials and are consistently half that of the initial glass beads (Supplementary Material III.11).

III.5 Liquid spreading and redistribution of salts

Comparison between Fig III.2a and III.2b-d demonstrates that the NaCl crystals were redistributed during liquid spraying and aggregation. In the glass bead samples, evenly distributed crystals on the initially doped surfaces became localized NaCl crystal assemblages at particle-particle contact points. NaCl assemblages between coarse glass beads are larger in size (<10 µm) compared to those between fine bead materials (<2 µm; Fig III.2c, d), conveying less aggregate stability to fine materials. We interpret the formation of NaCl assemblages to be due to the capillary-driven action of liquid films toward contact points. To explore this, we consider a spherical particle of radius R with continuous film thickness h. The surface area of the film with air is $s_i = 4\pi(R+h)^2$. This can be minimized by bunching the liquid in a collar around the contact of two particles (Mitarai and Nori, 2006). The flow of the film toward the contact area where the curvature of the liquid surface is largest is driven by the excess Laplace pressure $P = 2\Gamma/a$, where a is the radius of curvature at the contact point. Since a is smaller (tighter curvature) than $R+h$ for the relative radii during liquid collar formation, the flow is toward the contact (Frenkel, 1945). Additionally, during drying of the liquid layer and collar, salts precipitate. We use these simple arguments to suggest that during or after dissolution of surface salt load, flow in the liquid film resulted in a liquid collar around the contact point of particles, which in turn led to the precipitation of salt at these collars on drying (Figs III.2 &

III.3). This effectively cemented the aggregates, preserving them for analysis. This process of (1) dissolution of soluble minerals on the surface of ash particles, (2) transport of the resulting liquid by capillary forces to contact points and (3) crystallization upon evaporation can be rather quick as evidenced from deposits of the 2006 eruption of Tungurahua volcano, Ecuador. In this case, accretionary lapilli were found exclusively close to Chambo river. During the eruption, pyroclastic density currents had temporarily dammed the river. The hot (200-500°C) deposits had interacted with the water, causing a secondary plume of elutriated ash and locally increased air humidity (Kueppers et al., 2016).

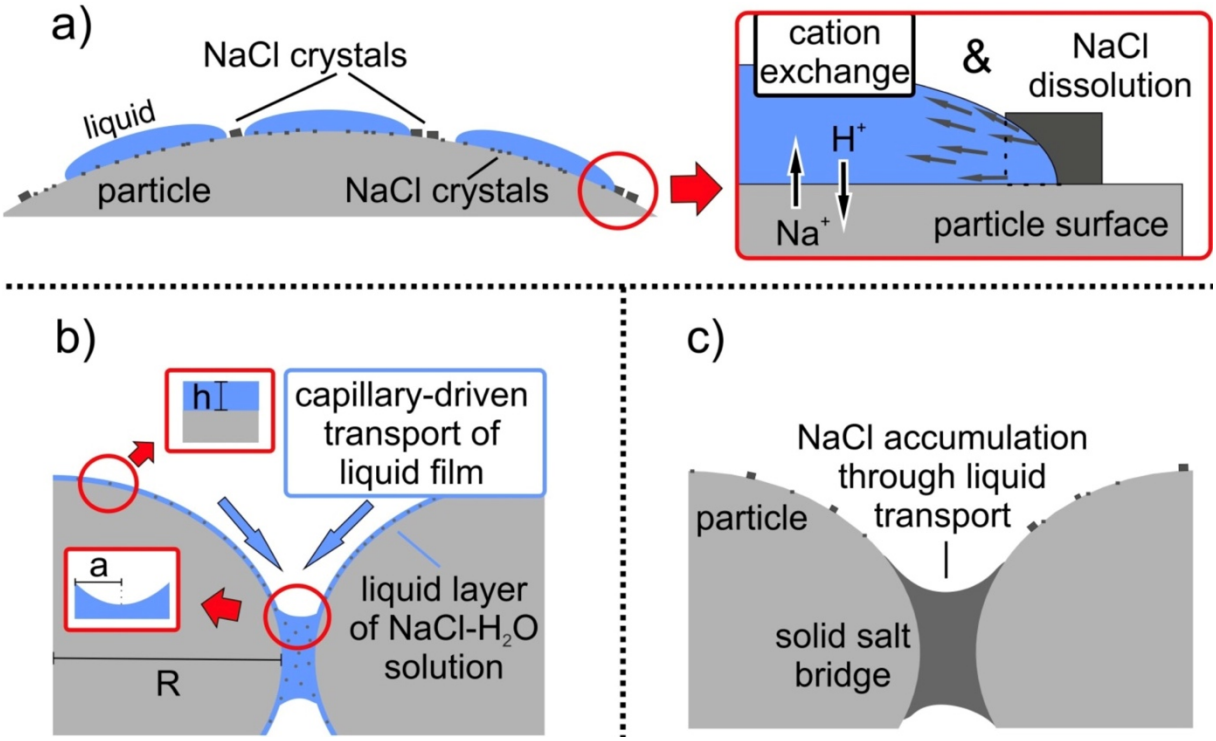

Figure III.3: (a) Liquid droplets of HCl or H_2O spread around the particle as a liquid film, dissolving the NaCl coating and triggering cation exchange with the underlying particle surface. (b) Capillary forces accumulate NaCl-H_2O brine at particle-particle contact points, forming liquid bridges. The liquid layer thickness h, particle radius R and the curvature of radius in the liquid neck a are labelled. (c) Evaporation of the liquids during drying processes leads to precipitation of a solid NaCl bridge and depletes the particle surface in NaCl crystals.

III.6 Surface leaching of materials

The interactions of volcanic ash particles and aggregates with HCl solutions offer insight into those between in-plume ash particles and acidic liquid droplets. In 12 M HCl experiments, there are strong relationships ($r^2 > 0.85$, when a linear relationship is assumed) between Al_s, K_s and Mn_s, elements which solely derive from ash surface dissolution; $K_s/Al_s \approx 0.33$, $Mn_s/Al_s = 0.03$, $Mn_s/K_s = 0.08$. However, no similar relationship is observed between Ca_s

or Mg_s or between these and any of the former elements. This likely reflects the fact that volcanic ash surface constituents do not dissolve at the same rates. Notably, the relative abundance of ratios K_s/Al_s, Mn_s/Al_s and Mn_s/K_s are similar to those for the bulk chemistry of the volcanic ash material. Previous studies of volcanic glass (basalt to rhyolite compositions) in low pH environments (pH 4 in dissolution experiments (Oelkers and Gislason, 2001), or pH <1 in field observations (Gilbert and Lane, 1994)), have shown that metal release rates decrease exponentially with increasing Si content. Silicate dissolution also involves an initially incongruent leaching of univalent and divalent cations from the near surface region; Al release exchange reactions between aqueous H^+ and Al in the glass structure set in before late-stage dissolution of the Si network takes place (Oelkers and Gislason, 2001; Wolff-Boenisch et al., 2004). While at long times of exposure to acidic solutions, the bulk silicate composition should be congruent with the leachate chemistry, over the short exposure times of the current study, it is likely that preferential leaching of alkalis and Al can explain our data.

Our observations highlight the influence of both variations in exposure time and in HCl concentration on surface dissolution. In the second experiment series using the volcanic ash material, the decrease in concentrations of soluble Al, Ca, K, Mg and Mn with decreasing HCl concentrations (Fig III.4a) is due to the decreasing leaching efficiency and subsequent dissolution of the silicate network. Additionally, volcanic ash aggregates produced herein and extracted after only 10 seconds of exposure to 12 M HCl solutions produced significant concentrations of soluble elements; on average, concentrations were ~3 times higher than the global median of published ash leachate data (Ayris and Delmelle, 2012). For comparison, at the end of the experiment, after 375 s, concentrations were ~20 times higher. Even considering that the high measured specific surface area (SSA_{BET}; 3 $m^2.g^{-1}$) of the volcanic ash materials amplifies the representation of surface salts in leachate data relative to natural ash samples with lower SSA_{BET} (e.g., 1-2 $m^2.g^{-1}$, Delmelle et al., 2005), these results still demonstrate the capacity for salt formation in volcanically relevant quantities on very short timescales.

III.7 Relevance to natural processes

Artificial aggregation experiments with the *ProCell Lab* can represent natural processes directly without the necessity for scaling. Reynolds numbers in the fluidized bed system at the operating conditions used here suggest that our experiments most likely reflect conditions of limited particle concentrations ("dilute"), as expected in the upper part of eruption columns or in the ash cloud overriding pyroclastic density currents (Mueller et al., 2016). Binder concentrations reported in this study are higher than a natural average but still within the upper limits of measured ranges. Artificial aggregation with average salt concentrations reported for natural aggregates (~100s $mg.kg^{-1}$) however has been carried out with the *ProCell*

Lab (Mueller et al., 2016) with similar aggregation results. Experimental relative air humidity necessary for aggregation (>10%), temperature range (40-60°C) and particle size distributions (<90 µm) are all naturally applicable.

III.8 Implications

Our experimental results represent the first laboratory investigation of the chemical interactions between volcanic ash or glass beads and acid liquid droplets at temperature and time conditions relevant to explosive eruptions. Our experiments suggest that interaction with variably concentrated HCl droplets promote the preferential leaching and dissolution of the ash surface and the precipitation of surficial chloride salts. Excluding the pre-existing halite load, these salts were emplaced as submicron-sized, patchily distributed deposits, similar to those observed on natural ash surfaces (Delmelle et al., 2007; Gislason et al., 2011). In experiments conducted with 12 M HCl, volcanologically-relevant quantities of salts were formed within 10 s of exposure, while quantities far in excess of those typically observed in volcanic ash leachates were formed after 375 s. In the latter experiment, such prolonged exposure times may only be relevant to the largest explosive eruptions; 3D plume models (Suzuki et al., 2005) indicate that some ash particles in such events may be exposed to temperature of 40-50 ºC for similar periods. Dissolution of the ash surface by acid liquid droplets in large explosive eruptions, particularly those which emit a significant quantity of HCl, may therefore produce ash with high loads of biologically-relevant (Ayris et al., 2014) and readily-soluble minor elements relative to that from smaller eruptions.

However, not all erupted ash particles will encounter liquid droplets of 12 M HCl, and silicate dissolution at lower temperatures than those utilized in our experiments is significantly slower (Chen and Brantley, 1997). Accordingly, it is likely that interactions between ash and acidic liquid droplets in both large and small eruptions produce varying abundances of soluble salts, perhaps even from ash particle to particle according to their individual plume trajectories. Notably, comparison of eight pristine ash leachate data sets (Smith et al., 1983; Hinkley et al., 1987; Armienta et al., 1998; Ruggierei et al., 2011; Durant et al., 2012; Bagnato et al., 2013; D'Addabbo et al., 2015) reveals that Ca, Mg, K, and a number of biologically-relevant minor and trace elements (Ba, Co, Cu, Li, Mn, Sr) increase with increasing Na concentrations (Fig 4b). This should not be interpreted to indicate that Na is a causative factor, but rather that the coincident increase in the abundance of major (Na, K, Mg, Ca) and both minor and trace elements is consistent with increasing ash surface dissolution by liquid acid films both within and across the different studies.

If acidic liquid films drive the formation of soluble salts in most volcanic eruptions, ash deposits with comparatively high yields of biologically-relevant minor elements may coincide

with areas of aggregate-driven sedimentation. Notably, in the retrospective analysis of ash leachates from the May 18th eruption of Mount St Helens, it was noted that a region of low Na_s/Cl_s ratios, indicative of the presence of chloride salts other than halite and attributed to ash interaction with HCl-rich hydrometeors, occurred in an area of aggregate fallout (Ayris et al., 2015). For the same eruption, our observations can also explain the preservation of well-rounded aggregates in the co-ignimbrite ash fall deposits from afternoon flows on May 18th. It was suggested that vaporization of glacier ice or groundwater promoted aggregation of ash (Waitt and Dzurisin, 1981). Leaching of ash from blast deposits revealed a high salt load (Hinkley et al., 1987), which would have encouraged preservation of aggregates (Mueller et al, 2016). While the pre-existing salt load can be derived from several processes such as pre-eruptive alteration by high temperature gases (Ayris et al., 2015), or the production of an NaCl brine (Shinohara, 1994) which deposits NaCl aerosols on ash surfaces (Taylor and Stoiber, 1973; Smith et al., 1982), the condensation of water or acidic droplets onto ash particles would have dissolved the existing salts, re-precipitating them at particle-particle contact points, cementing the aggregates and permitting their preservation within the deposits.

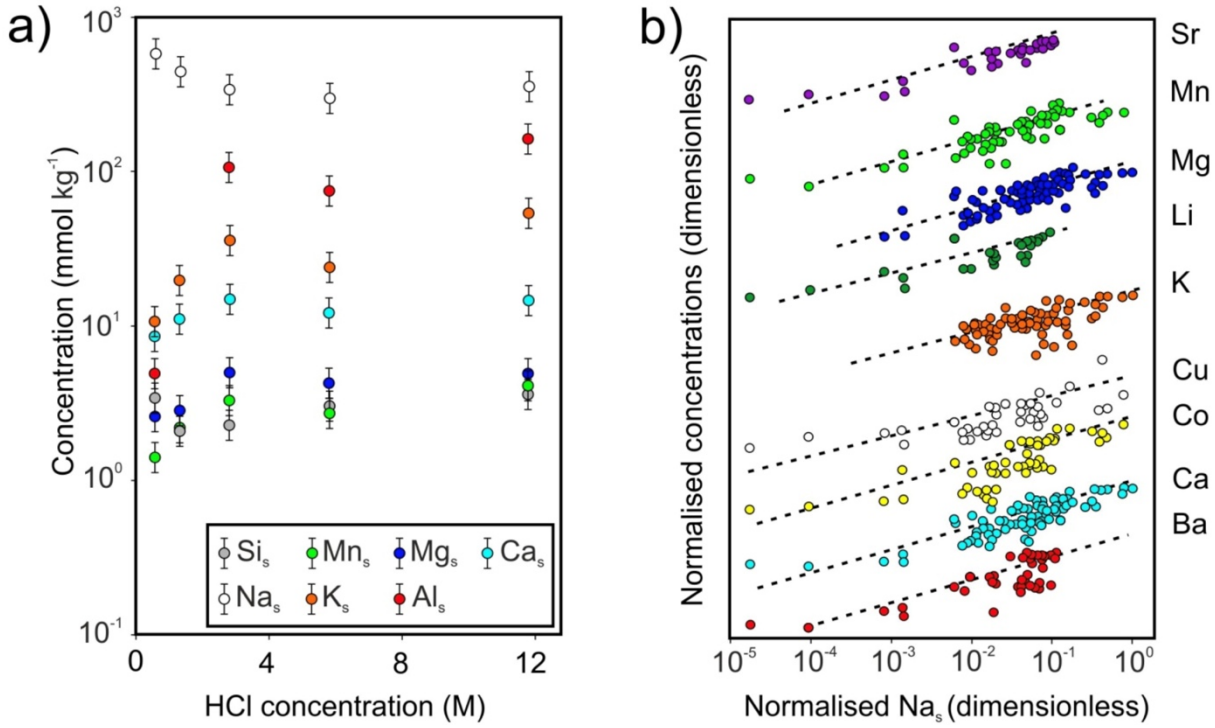

Figure III.4: Composite figure displaying a) Na_s, Al_s, K_s, Ca_s, Mg_s, Mn_s, Si_s from volcanic ash materials sprayed with varying HCl concentrations; b) selected soluble element concentrations plotted against soluble Na concentrations using data from eleven leachate studies (see Supplementary Material III.11), normalized to their maxima and offset arbitrarily to be viewable at the same scale, with best-fit power-laws provided to guide the eye and to demonstrate a commonality of slope.

Volcanic ash aggregates bound by NaCl have been previously described at Sakurajima volcano, Japan (Gilbert and Lane, 1994). The formation of NaCl-laden aggregates in the current study presents further insight into the mechanisms of salt emplacement on ash surfaces and their environmental fate. The spreading of a liquid film around the ash surface may re-deposit the most soluble salts in areas of favourable surface morphology, while less soluble salts are dispersed across larger regions of the surface. Convincingly, previous studies on ash-gas interactions (Delmelle et al., 2007) and on ash deposits of the 2010 Eyjafjallajökull eruption (Gislason et al., 2011), have documented thin nanoscale halite coatings on some particle surfaces, similar to those in Fig. III.2e. The re-distribution of highly soluble salts from across the ash surface into isolated assemblages potentially obscured or hidden by surface topography could also make them difficult to observe without extensive microscopy analyses, and impede their identification by surface sensitive techniques (e.g., XPS, Delmelle et al., 2007), as their proportional footprint on the ash surface will be small.

Ash aggregation can occur by multiple processes, and does not necessarily require salt-formation to bind particles together (Gilbert and Lane, 1994; Bonadonna et al., 2002; Van Eaton et al., 2012). Alternative possibilities include rapid alteration of ash surfaces in the presence of liquid water producing coatings of amorphous silica (Van Eaton et al., 2012) or high temperature sintering by either viscous flow of hot ash surfaces producing necks or diffusive exchange (Brown et al., 2010). However, salt redistribution volcanic ash surfaces or surface dissolution-derived salt formation during any of the mechanisms of initial aggregation will increase the stability of aggregates.

III.9 Acknowledgements

This work is supported by the Marie Curie Initial Training Network 'VERTIGO', funded through the European Seventh Framework Program (FP7 2007-2013) under Grant Agreement number 607905. David E. Damby is acknowledged for fruitful discussions and input during an early stage of this study. We are indebted to Ulrich Walter and Katja Oppermann for their support at Glatt Ingenieurtechnik GmbH. The Laacher See ash used in this study was provided by ROTEC GmbH & Co. KG (Mühlheim-Kärlich, Germany). We acknowledge the support of European Research Council Advanced Grant 247076 "EVOKES" (Explosive volcanism in the Earth System).

III.10 Author contributions

S. B. Mueller, M. Jacob and U. Kueppers performed the aggregation experiments, S. B. Mueller and P. Ayris leached the samples and compiled the first draft of the manuscript. A. S.

Casas performed surface area determination. S. B. Mueller and J. Taddeucci performed the SEM measurements. S.B. Mueller and F. B. Wadsworth performed liquid spreading modelling and finalized the submitted manuscript. All authors interpreted the data and contributed to the manuscript.

III.11 Supplementary material

Table III.S1: Compilation of aggregate specific surface area (m^2 g^{-1}) expressed as geometric specific surface area (GEO), and as measured by argon adsorption and application of the BET theory to the post-experiment aggregates (BET); and analytical leaching data for the measured elements (Na, Cl, Al, Ca, K, Mg, Mn, Si; $mmol.kg^{-1}$) for SLS materials following aggregation experiments with variable halite concentrations after spraying with water (SW1) or with 12 M HCl (SA1-6), and for PHN materials following aggregation experiments with variable halite concentrations after spraying with water (PW1); with 12 M HCl (PA1-6a); and with variably diluted HCl solutions (PC1-6). The ratios of Na_s:Cl_s and Na_s:Na_p, described in the main text, are also given where appropriate. Additionally included is the global mean concentration (GM) of the same measured elements in other volcanic ash leachate studies (Smith et al. 1983; Hinkley et al., 1987; Armienta et al. 1998; De Hoog et al. 2001; Ruggieri et al. 2011; Durant et al. 2012; Bagnato et al. 2013 D'Addabo et al. 2015).

Table III.S2: A compilation of leachate data for various cations used to generate Fig. III.3b, as reported in seven previous studies of volcanic ash. Included as a separate digital .xlsx file, including the study of origin, denoted by a two letter code also documented in the .xlsx file, the original sample code, and the leachate concentration reported in mmol kg^{-1}. Data were excluded when leachate compositions were i) not reported, ii) incompletely reported, iii) reported as an average of multiple ash samples, iv) not pristine, or v) reported as being below the detection limit of the prior study.

Sample Code	Halite [mmol kg^{-1}]	Acid conc. [M]	Specific surface area [m^2 g^{-1}]		Mean PSD (µm)	Leachate concentration [mmol kg^{-1}]								Elemental ratios	
			GEO	BET		Na	Cl	Al	Ca	K	Mg	Mn	Si	Na_s/Cl_s	Na_s/Na_p
SLS	0	0	0.09	3.4	60.5	1.24	<0.1	<0.1	0.9	<0.1	<0.1	<0.1	0.5	-	
SW1	254	0	-	-	*59.3*	-	-	-	-	-	-	-	-		
SA1	19	12	0.05	-	61.3	72.0	72.0	0.2	2.4	0.4	0.6	<0.1	1.9	1.0	3.8
SA2	28	12	-	-	58.2	60.8	61.9	0.1	3.1	0.4	0.6	0.1	2.2	1.0	2.2
SA3	36	12	0.06	-	60.1	64.4	66.7	0.1	2.8	0.4	0.6	<0.1	1.7	1.0	1.8
SA4	84	12	0.06	-	55.1	103.4	104.8	0.2	3.4	0.6	0.8	<0.1	2.2	1.0	1.2
SA5	168	12	0.05	-	63.2	147.1	145.1	0.0	2.6	0.4	0.5	<0.1	1.8	1.0	0.9
SA6	248	12	0.05	-	60.7	142.7	138.6	0.1	1.8	0.3	0.4	<0.1	5.1	1.0	0.6
PHN	0	0	0.31	2.9	59.36	-	-	-	-	-	-	-	-	-	-
PA1	31	12	0.29	~	-	206.1	724.1	125	14.5	38.6	4.8	3.5	5.7	0.3	6.6
PA2	43	12	-	6.1	54.8	239.1	896.9	173.8	13.4	55.7	4.6	4.3	4.4	0.3	5.6
PA3	97	12	0.27	4.2	47.2	227.3	567.3	77.5	13.6	25.7	4.5	2.8	2.9	0.4	2.3
PA4	172	12	0.28	-	-	320.5	969.5	167	13.5	53.3	4.6	4.2	2.6	0.3	1.9
PA5	254	12	0.32	5.6	59.3	514.3	1308.	203.9	15.6	70.2	4.5	5.3	2.4	0.4	2.0
PA6	329	12	0.31	5.4	59.3	632.4	1273	168.8	13.5	57.5	3.9	4.4	3	0.5	1.9
PA6a	329	12	-	-	-	366.4	438.8	15.7	8.2	13.3	3	1.5	2.7	0.8	1.1
PC1	254	0	-	2.8	50.9	184.9	177.2	0.3	2.1	4.6	0.6	0.1	2.3	1.0	0.7
PC2	264	0.7	0.33	-	-	585.5	621.0	5.0	2.1	4.5	0.6	0.0	2.3	0.9	2.2
PC3	264	1.5	0.29	-	-	453.2	556.7	20.4	8.7	10.9	2.6	1.4	3.4	0.8	1.7
PC4	254	2.9	0.35	2.6	79.8	346.3	749.4	76.4	11.3	19.5	2.9	2.2	2.3	0.5	1.4
PC5	237	5.8	0.26	-	-	303.1	628.7	106.7	12.4	24.6	4.3	2.8	3.1	0.5	1.3
PC6	237	12	-	-	-	359.5	977.1	164.2	15.2	36.6	5.0	3.3	2.3	0.3	1.5
GM	-	-	-	-	-	17.7	33.9	2.3	54	1.9	14.4	0.4	1.0	-	-

Table III.S1

Leachate concentration (mmol.kg^{-1})

Armienta et al. (1998). Geochemistry of ash leachates during the 1994–1996 activity of Popocatepetl volcano.

Al	As	B	Ba	Ca	Cd	CO	Cr	Cs	Cu	Fe	K	Li	Mg	Mn	Mo	Na	Ni	Pb	Rb	Sb	Se	Si	Sr	Th	Ti	U	V	Zn
-	-	-	-	1.2E+02	-	-	-	-	-	-	3.0E+00	-	2.5E+00	-	-	1.1E+01	-	-	-	-	1.3E+02	-	-	-	-	-	-	-
-	-	-	-	2.2E+02	2.5E-03	2.0E-02	-	-	4.4E-02	-	8.1E+00	-	1.4E+01	4.2E-01	-	3.4E+01	-	8.5E-02	-	5.7E-04	2.3E+02	-	-	-	7.1E-03	-	-	8.1E-01
-	-	-	-	1.2E+02	1.9E-03	1.8E-02	-	-	8.0E-03	-	5.6E+00	-	1.0E+01	4.0E-01	-	2.3E+01	-	-	-	4.9E-04	1.4E+02	-	-	-	7.1E-03	-	-	1.7E-01
-	-	-	-	7.3E+01	6.2E-04	1.5E-02	-	-	-	-	1.7E+00	-	6.2E+00	2.3E-01	-	6.5E+01	-	-	-	5.7E-04	9.2E+01	-	-	-	2.1E-04	-	-	2.0E-01
-	-	-	-	5.0E+01	-	-	-	-	-	-	4.1E+00	-	6.9E+00	-	-	3.2E+01	-	-	-	-	5.7E+01	-	-	-	-	-	-	-
-	-	-	-	1.9E+01	-	-	-	-	-	-	3.9E+00	-	2.8E+00	-	-	1.1E+01	-	-	-	-	1.9E+01	-	-	-	-	-	-	-
-	-	-	-	4.5E+01	-	-	-	-	-	-	2.1E+00	-	3.5E+00	-	-	7.0E+01	-	-	-	-	4.4E+01	-	-	-	-	-	-	-
-	-	-	-	-	2.7E-04	2.2E-03	-	-	2.0E-03	-	-	-	-	8.8E-02	-	-	-	-	-	7.4E-04	-	-	-	-	1.9E-03	-	-	2.9E-02
-	-	-	-	4.7E+01	-	-	-	-	-	-	1.2E+01	-	5.7E+00	-	-	2.4E+01	-	-	-	-	6.0E+01	-	-	-	-	-	-	-
-	-	-	-	-	3.6E-04	6.4E-03	-	-	6.1E-03	-	-	-	-	1.6E-02	-	-	-	-	-	6.6E-04	-	-	-	-	-	-	-	1.1E-02
-	-	-	-	-	2.7E-04	1.1E-02	-	-	-	-	-	-	-	3.1E-02	-	-	-	-	-	4.9E-04	-	-	-	-	5.0E-03	-	-	-
-	-	-	-	2.5E+01	-	-	-	-	-	-	1.2E+01	-	2.0E+00	-	-	1.7E+01	-	-	-	-	3.1E+01	-	-	-	-	-	-	-
-	-	-	-	3.5E+01	-	-	-	-	-	-	1.7E+00	-	5.3E-01	-	-	3.5E+00	-	-	-	-	3.8E+01	-	-	-	-	-	-	-
-	-	-	-	-	8.9E-05	3.4E-04	-	-	-	-	-	-	-	1.3E-03	-	-	-	-	-	6.6E-04	-	-	-	-	-	-	-	-
-	-	-	-	-	1.3E-03	2.7E-03	-	-	-	-	-	-	-	1.3E-02	-	-	-	-	-	5.1E-02	-	-	-	-	7.1E-03	-	-	5.5E-03
-	-	-	-	1.7E+01	-	1.7E-04	-	-	-	-	8.8E-01	-	1.6E+00	2.3E-02	-	2.1E+00	-	6.0E-02	-	4.1E-04	1.9E+01	-	-	-	8.4E-04	-	-	-
-	-	-	-	8.7E+00	8.9E-04	1.7E-04	-	-	-	-	1.7E+00	-	1.8E+00	-	-	5.4E+00	-	-	-	4.1E-04	5.9E+00	-	-	-	-	-	-	-
-	-	-	-	4.0E+00	2.6E-03	5.1E-04	-	-	7.1E-03	-	5.3E+00	-	1.9E+00	1.6E-03	-	5.4E+00	-	3.4E-02	-	4.1E-04	6.0E+00	-	-	-	1.9E-03	-	-	4.8E-02
-	-	-	-	4.2E+01	-	-	-	-	-	-	9.7E+00	-	2.6E+01	-	-	5.3E+01	-	-	-	-	9.2E+01	-	-	-	-	-	-	-
-	-	-	-	-	3.6E-04	1.7E-04	-	-	-	-	-	-	-	-	-	-	-	-	-	4.9E-04	-	-	-	-	-	-	-	5.1E-02
-	-	-	-	1.2E+01	-	-	-	-	-	-	2.7E+00	-	6.6E+00	-	-	1.3E+01	-	-	-	-	2.4E+01	-	-	-	-	-	-	-

Bagnato et al. (2013). Scavenging of sulphur, halogens and trace metals by volcanic ash: the 2010 Eyjafjallajökull eruption.

Al	As	B	Ba	Ca	Cd	CO	Cr	Cs	Cu	Fe	K	Li	Mg	Mn	Mo	Na	Ni	Pb	Rb	Sb	Se	Si	Sr	Th	Ti	U	V	Zn
9.2E-02	1.3E-04	1.9E-04	7.3E-04	7.6E-01	3.5E-03	7.3E-03	4.4E-03	3.8E-05	1.6E-04	5.4E-04	1.9E-01	1.4E-03	1.0E-01	4.7E-03	2.1E-05	1.6E+00	1.2E-03	9.7E-06	2.0E-03	1.6E-05	1.3E-04	-	4.0E-03	3.0E-04	7.5E-02	1.3E-05	4.0E-05	3.1E-03
4.0E+00	6.7E-04	9.3E-04	3.9E-03	2.7E+00	1.6E-03	3.4E-04	3.8E-05	2.3E-06	4.6E-03	5.6E-03	2.4E-01	7.2E-03	2.7E-01	8.0E-02	2.1E-04	3.9E+00	1.9E-03	4.8E-06	4.7E-04	2.5E-06	8.9E-04	-	1.3E-02	4.3E-06	4.6E-03	4.2E-06	4.0E-04	3.0E-02
3.7E+00	6.7E-04	1.9E-03	3.3E-03	1.8E+00	1.2E-03	3.4E-04	3.8E-05	2.3E-06	5.2E-03	8.6E-03	1.7E-01	7.2E-03	2.1E-01	7.6E-02	2.1E-04	3.4E+00	1.7E-03	4.8E-05	4.7E-04	8.2E-06	8.9E-04	-	1.2E-02	4.3E-06	3.3E-03	4.2E-06	6.0E-04	2.5E-02
3.9E+00	6.7E-04	1.9E-03	3.9E-03	7.3E+00	1.3E-03	3.4E-04	3.8E-05	1.5E-06	3.9E-03	3.4E-03	6.1E-01	5.8E-03	6.6E-01	7.8E-02	2.1E-04	1.0E+01	2.0E-03	4.8E-06	4.7E-04	3.3E-06	8.9E-04	-	1.3E-02	4.3E-06	3.1E-03	4.2E-06	4.0E-04	2.4E-02
1.0E+00	2.7E-04	9.3E-04	1.9E-03	7.6E+00	3.6E-04	1.7E-04	1.9E-05	2.3E-06	7.9E-03	5.2E-03	6.3E-01	2.9E-03	8.7E-01	2.9E-02	1.0E-04	9.8E+00	1.5E-03	4.8E-06	2.3E-04	2.5E-06	2.5E-04	-	4.0E-03	4.3E-06	1.9E-03	8.4E-07	4.0E-04	1.6E-02
1.6E+00	1.3E-04	9.3E-04	2.1E-03	7.5E+00	5.3E-04	1.7E-04	1.9E-05	1.5E-06	4.2E-03	2.7E-03	5.4E-01	2.9E-03	6.4E-01	3.2E-02	1.0E-04	9.7E+00	1.4E-03	4.8E-06	2.3E-04	1.6E-06	2.5E-04	-	4.6E-03	4.3E-06	1.3E-03	3.8E-06	8.0E-05	1.3E-02
3.8E+00	6.7E-04	9.3E-04	2.5E-03	5.4E+00	1.2E-03	3.4E-04	3.8E-05	2.3E-05	7.1E-03	7.0E-03	5.0E-01	5.8E-03	5.4E-01	7.1E-02	2.1E-04	8.4E+00	1.5E-03	4.8E-06	4.7E-04	2.5E-06	8.9E-04	-	1.1E-02	4.3E-06	5.0E-03	4.2E-06	2.6E-04	2.3E-02
1.2E+00	1.3E-04	-	1.8E-03	2.2E+00	4.4E-04	1.7E-04	5.8E-05	1.5E-06	2.4E-03	5.4E-03	2.8E-01	4.3E-03	3.2E-01	2.8E-02	1.0E-04	4.1E+00	6.8E-04	1.4E-05	1.2E-04	1.6E-06	1.3E-04	-	3.7E-03	4.3E-06	1.7E-03	2.1E-06	2.0E-04	1.3E-02
1.0E+00	1.3E-04	9.3E-04	1.9E-03	1.7E+00	2.7E-04	1.7E-04	3.8E-05	1.5E-06	4.7E-04	1.1E-03	1.5E-01	2.9E-03	3.1E-01	1.9E-02	4.2E-05	3.7E+00	6.8E-04	4.8E-06	1.2E-04	1.6E-06	1.3E-04	-	3.2E-03	8.6E-07	4.2E-04	8.4E-07	-	7.6E-03

5.1E-01	4.0E-05	-	3.2E-03	1.1E+00	8.9E-05	-	3.8E-05	1.5E-06	1.6E-04	9.0E-04	1.0E-01	1.4E-03	1.6E-01	9.1E-03	4.2E-05	2.0E+00	3.4E-04	4.8E-06	4.7E-05	1.6E-06	1.3E-04	-	1.8E-03	8.6E-07	-	8.4E-07	-	2.3E-03

De Hoog et al. (2001). Sulfur and chlorine degassing from primitive arc magmas: temporal changes during the 1982–1983 eruptions of Galunggung (West Java, Indonesia).

Al	As	B	Ba	Ca	Cd	CO	Cr	Cs	Cu	Fe	K	Li	Mg	Mn	Mo	Na	Ni	Pb	Rb	Sb	Se	Si	Sr	Th	Ti	U	V	Zn
1.3E-01	-	-	-	1.6E+01	-	-	-	-	-	4.3E-02	-	-	6.6E+00	4.6E-01	-	1.1E+01	-	-	-	-	-	5.6E-01	-	-	-	-	-	-
8.9E-02	-	-	-	2.8E+01	-	-	-	-	-	1.8E-02	-	-	1.0E+01	9.1E-01	-	2.1E+01	-	-	-	-	-	7.8E-01	-	-	-	-	-	-
-	-	-	-	6.2E+01	-	-	-	-	-	1.4E-02	-	-	1.3E+01	1.0E+00	-	2.4E+01	-	-	-	-	-	1.4E+00	-	-	-	-	-	-
5.3E-01	-	-	-	2.3E+01	-	-	-	-	-	2.9E-01	-	-	5.6E+00	1.6E-01	-	1.8E+01	-	-	-	-	-	2.8E+00	-	-	-	-	-	-
1.1E-01	-	-	-	3.1E+00	-	-	-	-	-	1.6E-02	-	-	1.5E+00	2.2E-02	-	1.1E+01	-	-	-	-	-	3.1E-01	-	-	-	-	-	-
2.9E-01	-	-	-	3.3E+01	-	-	-	-	-	1.6E-01	-	-	8.8E+00	1.2E-01	-	1.6E+01	-	-	-	-	-	2.9E+00	-	-	-	-	-	-
1.6E-01	-	-	-	2.8E+01	-	-	-	-	-	2.7E-02	-	-	8.3E+00	4.2E-01	-	2.2E+01	-	-	-	-	-	9.6E-01	-	-	-	-	-	-
1.2E-01	-	-	-	3.0E+01	-	-	-	-	-	2.5E-02	-	-	9.3E+00	4.9E-01	-	2.7E+01	-	-	-	-	-	8.5E-01	-	-	-	-	-	-
-	-	-	-	5.9E+00	-	-	-	-	-	5.6E-01	-	-	3.7E+00	1.0E-01	-	1.5E+01	-	-	-	-	-	3.6E-01	-	-	-	-	-	-
2.1E-01	-	-	-	5.8E+00	-	-	-	-	-	1.1E-02	-	-	3.7E+00	8.7E-02	-	1.1E+01	-	-	-	-	-	6.4E-02	-	-	-	-	-	-
-	-	-	-	1.0E+01	-	-	-	-	-	1.4E-02	-	-	6.0E+00	1.3E-01	-	1.8E+01	-	-	-	-	-	2.3E-01	-	-	-	-	-	-
4.1E-01	-	-	-	1.0E+01	-	-	-	-	-	2.3E-02	-	-	3.4E+00	6.2E-02	-	2.5E+01	-	-	-	-	-	6.8E-01	-	-	-	-	-	-
2.7E-01	-	-	-	1.2E+00	-	-	-	-	-	-	-	-	7.0E-01	-	-	9.4E+00	-	-	-	-	-	5.7E-02	-	-	-	-	-	-
-	-	-	-	-	-	-	-	-	-	8.2E-02	-	-	-	-	-	9.7E+00	-	-	-	-	-	5.0E-01	-	-	-	-	-	-
2.3E+00	-	-	-	1.3E+01	-	-	-	-	-	-	-	-	7.3E+00	1.1E-01	-	1.8E+01	-	-	-	-	-	2.0E-01	-	-	-	-	-	-
1.4E-01	-	-	-	4.6E+00	-	-	-	-	-	-	-	-	6.2E-01	-	-	9.6E+00	-	-	-	-	-	1.1E-01	-	-	-	-	-	-
-	-	-	-	1.0E+00	-	-	-	-	-	-	-	-	5.8E-01	-	-	1.0E+01	-	-	-	-	-	1.3E-01	-	-	-	-	-	-
-	-	-	-	-	-	-	-	-	-	-	-	-	-	-	-	8.3E+00	-	-	-	-	-	1.4E-01	-	-	-	-	-	-
-	-	-	-	-	-	-	-	-	-	-	-	-	-	-	-	7.9E+00	-	-	-	-	-	1.1E-01	-	-	-	-	-	-

Durant et al. (2012). Long-range volcanic ash transport and fallout during the 2008 eruption of Chaitén Volcano, Chile.

Al	As	B	Ba	Ca	Cd	CO	Cr	Cs	Cu	Fe	K	Li	Mg	Mn	Mo	Na	Ni	Pb	Rb	Sb	Se	Si	Sr	Th	Ti	U	V	Zn
1.6E-01	-	-	-	2.1E+00	3.0E-06	2.4E-05	4.0E-06	-	6.6E-04	1.6E-02	3.5E-01	-	5.9E-01	5.0E-02	-	3.3E+00	6.4E-05	-	-	-	5.5E-05	6.1E-01	-	-	-	-	-	5.5E-03
8.0E-02	-	-	-	3.3E+00	1.0E-06	2.5E-05	-	-	2.6E-04	5.7E-03	9.6E-01	-	5.8E-01	4.0E-02	-	3.0E+00	7.5E-05	-	-	-	8.6E-05	4.6E-01	-	-	-	-	-	4.0E-04
1.0E-01	-	-	-	6.3E-01	-	1.0E-05	9.0E-06	-	4.6E-04	8.0E-04	2.8E-01	-	4.8E-01	1.7E-03	-	3.4E+00	6.6E-05	-	-	-	6.7E-05	5.1E-01	-	-	-	-	-	-
9.0E-02	-	-	-	1.1E+00	2.0E-06	1.8E-05	2.0E-06	-	3.5E-04	3.2E-03	4.0E-01	-	2.9E-01	2.4E-02	-	2.4E+00	3.7E-05	-	-	-	-	3.5E-01	-	-	-	-	-	5.2E-03
4.0E-02	-	-	-	4.2E+00	-	1.4E-05	-	-	3.7E-04	1.5E-04	3.6E-01	-	7.6E-01	1.3E-02	-	3.1E+00	7.6E-05	-	-	-	4.2E-05	5.2E-01	-	-	-	-	-	-
8.0E-02	-	-	-	2.8E+00	-	2.2E-05	2.0E-05	-	3.1E-04	8.2E-03	2.9E-01	-	1.2E+00	2.3E-02	-	2.4E+00	5.2E-05	-	-	-	4.0E-06	4.5E-01	-	-	-	-	-	1.8E-04
1.3E-01	-	-	-	8.9E-01	1.0E-06	3.3E-05	4.3E-05	-	5.4E-04	1.3E-02	4.9E-01	-	4.0E-01	2.9E-02	-	1.8E+00	5.8E-05	-	-	-	-	4.9E-01	-	-	-	-	-	2.3E-03
1.7E-01	-	-	-	6.4E-01	2.0E-06	1.8E-05	-	-	3.4E-04	1.6E-02	7.3E-01	-	2.9E-01	1.8E-02	-	1.6E+00	3.8E-05	-	-	-	1.7E-05	6.0E-01	-	-	-	-	-	5.9E-03
6.0E-02	-	-	-	9.6E-01	1.0E-06	2.0E-05	-	-	3.5E-04	1.0E-04	8.7E-01	-	3.1E-01	2.3E-02	-	2.5E+00	4.3E-05	-	-	-	-	2.2E-01	-	-	-	-	-	3.3E-03
6.0E-02	-	-	-	4.4E+00	1.0E-06	9.0E-06	1.1E-05	-	4.0E-04	1.2E-03	3.1E-01	-	5.5E-01	1.0E-02	-	3.3E+00	8.0E-05	-	-	-	4.5E-05	8.2E-01	-	-	-	-	-	2.8E-04
2.0E-02	-	-	-	4.2E+00	1.0E-06	1.5E-05	7.7E-05	-	6.5E-04	-	4.6E-01	-	6.9E-01	6.8E-03	-	2.9E+00	2.3E-04	-	-	-	2.5E-05	7.8E-01	-	-	-	-	-	1.4E-04
7.0E-02	-	-	-	2.4E+00	2.0E-06	2.7E-05	-	-	3.6E-04	3.7E-03	5.0E-01	-	7.2E-01	5.0E-02	-	4.1E+00	8.6E-05	-	-	-	-	2.9E-01	-	-	-	-	-	3.1E-03

-	-	-	-	1.9E+00	-	-	-	-	-	-	5.6E-01	-	4.2E-01	-	-	3.5E+00	-	-	-	-	-	-	-	-	-	-	-	-
6.0E-02	-	-	-	1.2E+00	2.0E-06	7.0E-06	-	-	7.3E-04	3.6E-03	5.0E-02	-	2.4E-01	8.3E-03	-	3.6E+00	3.3E-05	-	-	-	2.0E-06	7.4E-01	-	-	-	-	-	-
-	-	-	-	2.0E+00	-	-	-	-	-	-	7.0E-02	-	2.1E-01	-	-	2.3E+00	-	-	-	-	-	-	-	-	-	-	-	-

Hinkley et al. (1987). Chemistry of ash and leachates from the May 18, 1980 eruption of Mount St. Helens, Washington.

Al	As	B	Ba	Ca	Cd	CO	Cr	Cs	Cu	Fe	K	Li	Mg	Mn	Mo	Na	Ni	Pb	Rb	Sb	Se	Si	Sr	Th	Ti	U	V	Zn
-	-	-	3.1E-02	1.7E+01	-	5.1E-03	-	-	-	-	1.8E+00	-	2.9E+00	1.8E-01	-	1.8E+01	-	-	-	-	-	1.1E+00	3.1E-02	-	-	-	-	-
-	-	-	3.0E-02	1.8E+01	-	5.1E-03	-	-	-	-	1.9E+00	-	3.3E+00	2.0E-01	-	1.8E+01	-	-	-	-	-	7.1E-01	3.1E-02	-	-	-	-	-
-	-	-	4.8E-02	2.2E+01	-	6.8E-03	-	-	-	-	2.3E+00	-	3.7E+00	2.6E-01	-	2.3E+01	-	-	-	-	-	1.1E+00	3.8E-02	-	-	-	-	-
-	-	-	2.5E-02	2.3E+01	-	5.1E-03	-	-	-	-	2.2E+00	-	3.7E+00	2.6E-01	-	2.3E+01	-	-	-	-	-	7.1E-01	3.8E-02	-	-	-	-	-
-	-	-	3.5E-02	2.2E+01	-	5.1E-03	-	-	-	-	2.5E+00	-	4.1E+00	3.3E-01	-	1.5E+01	-	-	-	-	-	7.1E-01	3.9E-02	-	-	-	-	-
-	-	-	2.3E-02	1.1E+01	-	5.1E-03	-	-	-	-	1.4E+00	-	2.1E+00	1.5E-01	-	8.7E+00	-	-	-	-	-	7.1E-01	2.1E-02	-	-	-	-	-
-	-	-	2.8E-02	2.4E+01	-	5.1E-03	-	-	-	-	2.5E+00	-	4.1E+00	2.7E-01	-	1.7E+01	-	-	-	-	-	1.1E+00	4.0E-02	-	-	-	-	-
-	-	-	3.4E-02	2.4E+01	-	6.8E-03	-	-	-	-	2.4E+00	-	4.1E+00	2.7E-01	-	1.8E+01	-	-	-	-	-	1.1E+00	4.0E-02	-	-	-	-	-
-	-	-	4.9E-02	3.0E+01	-	5.1E-03	-	-	-	-	2.9E+00	-	4.9E+00	3.5E-01	-	2.2E+01	-	-	-	-	-	1.1E+00	4.9E-02	-	-	-	-	-
-	-	-	3.5E-02	2.7E+01	-	6.8E-03	-	-	-	-	2.7E+00	-	4.5E+00	3.3E-01	-	2.0E+01	-	-	-	-	-	1.1E+00	4.3E-02	-	-	-	-	-
-	-	-	2.4E-02	3.0E+01	-	5.1E-03	-	-	-	-	2.8E+00	-	4.5E+00	3.5E-01	-	2.1E+01	-	-	-	-	-	1.1E+00	4.8E-02	-	-	-	-	-
-	-	-	3.8E-02	1.8E+01	-	5.1E-03	-	-	-	-	1.9E+00	-	3.3E+00	2.4E-01	-	1.7E+01	-	-	-	-	-	1.1E+00	3.2E-02	-	-	-	-	-
-	-	-	2.3E-02	9.5E+00	-	3.4E-03	-	-	-	-	1.4E+00	-	2.5E+00	1.3E-01	-	1.5E+01	-	-	-	-	-	3.6E-01	1.8E-02	-	-	-	-	-
-	-	-	3.9E-02	9.0E+00	-	5.1E-03	-	-	-	-	1.3E+00	-	2.1E+00	1.1E-01	-	1.5E+01	-	-	-	-	-	7.1E-01	1.7E-02	-	-	-	-	-
-	-	-	3.4E-02	1.0E+01	-	3.4E-03	-	-	-	-	1.0E+00	-	1.6E+00	1.1E-01	-	1.2E+01	-	-	-	-	-	7.1E-01	1.9E-02	-	-	-	-	-
-	-	-	3.1E-02	7.0E+00	-	3.4E-03	-	-	-	-	9.0E-01	-	1.2E+00	5.5E-02	-	6.1E+00	-	-	-	-	-	1.1E+00	1.1E-02	-	-	-	-	-
-	-	-	2.6E-02	2.7E+01	-	5.1E-03	-	-	-	-	2.3E+00	-	3.7E+00	2.9E-01	-	1.7E+01	-	-	-	-	-	1.1E+00	4.3E-02	-	-	-	-	-
-	-	-	3.2E-02	1.0E+01	-	3.4E-03	-	-	-	-	1.2E+00	-	2.1E+00	1.5E-01	-	1.3E+01	-	-	-	-	-	7.1E-01	2.1E-02	-	-	-	-	-
-	-	-	2.5E-02	1.1E+01	-	5.1E-03	-	-	-	-	1.4E+00	-	2.1E+00	1.6E-01	-	1.3E+01	-	-	-	-	-	7.1E-01	2.2E-02	-	-	-	-	-
-	-	-	4.2E-02	8.0E+00	-	5.1E-03	-	-	-	-	-	-	1.6E+00	1.3E-01	-	1.3E+01	-	-	-	-	-	7.1E-01	1.7E-02	-	-	-	-	-
-	-	-	4.9E-02	1.0E+01	-	5.1E-03	-	-	-	-	9.7E-01	-	1.6E+00	5.5E-02	-	1.0E+01	-	-	-	-	-	1.1E+00	1.8E-02	-	-	-	-	-
-	-	-	2.3E-02	8.2E+00	-	5.1E-03	-	-	-	-	9.2E-01	-	1.6E+00	1.1E-01	-	1.2E+01	-	-	-	-	-	-	1.7E-02	-	-	-	-	-
-	-	-	1.6E-02	8.2E+00	-	3.4E-03	-	-	-	-	9.5E-01	-	1.6E+00	1.1E-01	-	1.1E+01	-	-	-	-	-	3.6E-01	1.8E-02	-	-	-	-	-
-	-	-	3.9E-02	7.5E+00	-	5.1E-03	-	-	-	-	9.7E-01	-	1.6E+00	1.1E-01	-	1.1E+01	-	-	-	-	-	-	1.6E-02	-	-	-	-	-
-	-	-	2.1E-02	7.5E+00	-	5.1E-03	-	-	-	-	9.7E-01	-	1.6E+00	1.1E-01	-	1.1E+01	-	-	-	-	-	-	1.6E-02	-	-	-	-	-
-	-	-	2.8E-02	6.5E+00	-	5.1E-03	-	-	-	-	7.7E-01	-	1.2E+00	5.5E-02	-	8.7E+00	-	-	-	-	-	3.6E-01	1.5E-02	-	-	-	-	-
-	-	-	3.5E-02	1.7E+01	-	3.4E-03	-	-	-	-	1.5E+00	-	2.5E+00	1.6E-01	-	1.4E+01	-	-	-	-	-	7.1E-01	3.0E-02	-	-	-	-	-

D'Addabbo et al. (2015). Ash leachates from some recent eruptions of Mount Etna and Popocatépetl volcanoes and their impact on amphibian living freshwater organisms.

Al	As	B	Ba	Ca	Cd	CO	Cr	Cs	Cu	Fe	K	Li	Mg	Mn	Mo	Na	Ni	Pb	Rb	Sb	Se	Si	Sr	Th	Ti	U	V	Zn
-	1.2E-04	2.0E-01	-	9.7E+00	-	-	-	-	-	4.4E-02	8.3E-01	-	4.7E+00	1.8E-02	-	4.9E+00	-	-	-	-	-	5.1E-01	-	-	-	-	-	-
-	8.4E-04	1.8E-01	-	9.7E+00	-	-	-	-	-	5.9E-02	8.5E-01	-	4.8E+00	1.7E-02	-	4.6E+00	-	-	-	-	-	7.2E-01	-	-	-	-	-	-

-	1.4E-04	1.4E-01	-	8.0E+00	-	-	-	-	-	6.1E-02	1.5E-01	-	3.8E+00	3.0E-03	-	1.3E+00	-	-	-	-	-	2.8E-01	-	-	-	-	-	-
-	1.4E-04	5.1E-01	-	9.1E+00	-	-	-	-	-	4.7E-02	6.7E-01	-	4.3E+00	6.7E-03	-	2.8E+00	-	-	-	-	-	4.5E-01	-	-	-	-	-	-
-	-	6.7E-02	-	5.8E+01	-	-	-	-	-	1.1E-02	1.0E+00	-	2.9E+01	3.8E-01	-	2.4E+01	-	-	-	-	-	2.9E-01	-	-	-	-	-	-
-	-	3.5E-02	-	3.9E+01	-	-	-	-	-	-	7.5E-01	-	2.0E+01	2.5E-02	-	1.6E+01	-	-	-	-	-	7.4E-01	-	-	-	-	-	-

Ruggieri et al. (2011). Environmental geochemistry of recent volcanic ashes from the Southern Andes.

Al	As	B	Ba	Ca	Cd	CO	Cr	Cs	Cu	Fe	K	Li	Mg	Mn	Mo	Na	Ni	Pb	Rb	Sb	Se	Si	Sr	Th	Ti	U	V	Zn
5.5E-02	9.6E-05	1.1E-02	1.2E-04	2.5E-01	6.8E-06	2.1E-04	6.8E-05	3.0E-07	3.9E-04	3.1E-02	-	5.7E-04	5.0E-01	4.4E-03	3.5E-06	2.8E-01	4.5E-04	1.5E-05	3.6E-05	1.3E-06	-	3.0E-02	5.5E-04	-	1.9E-04	-	3.7E-05	3.3E-03
1.2E-02	7.8E-05	5.6E-03	2.0E-05	8.6E-02	8.9E-08	3.1E-06	4.9E-05	1.5E-07	5.6E-05	5.7E-03	-	6.1E-05	-	3.2E-04	5.5E-06	3.5E-03	1.7E-04	4.2E-06	5.0E-06	-	-	3.8E-02	8.1E-05	-	1.0E-03	-	-	8.9E-04
3.1E-02	1.1E-05	2.5E-03	1.4E-05	6.6E-02	6.2E-07	4.2E-06	4.5E-05	7.5E-08	2.0E-04	5.2E-03	-	1.4E-04	-	1.4E-04	2.0E-05	1.9E-02	1.8E-04	4.8E-06	-	-	-	4.6E-02	1.4E-04	-	4.9E-04	2.5E-07	4.2E-05	1.6E-03
5.2E-02	2.5E-03	1.4E-02	8.3E-05	1.2E-01	2.8E-06	7.8E-06	4.3E-05	5.0E-06	3.1E-04	2.5E-02	-	1.0E-03	3.2E-02	1.1E-03	3.3E-05	1.6E-01	1.9E-04	1.2E-05	5.6E-05	-	-	1.2E-01	1.1E-04	-	4.1E-04	3.8E-07	1.2E-04	1.4E-03
4.3E-02	7.2E-05	7.4E-03	4.9E-05	1.2E-01	2.8E-06	9.5E-06	7.9E-06	1.5E-07	8.9E-05	1.3E-02	-	1.7E-04	3.5E-02	1.1E-03	5.3E-06	2.9E-01	1.7E-04	1.0E-05	1.5E-05	2.5E-07	-	5.0E-02	1.9E-04	-	1.6E-03	-	9.6E-05	1.3E-03

Smith et al. (1983). Leaching characteristics of ash from the May 18, 1980, eruption of Mount St. Helens volcano, Washington.

Al	As	B	Ba	Ca	Cd	CO	Cr	Cs	Cu	Fe	K	Li	Mg	Mn	Mo	Na	Ni	Pb	Rb	Sb	Se	Si	Sr	Th	Ti	U	V	Zn
-	-	-	1.2E-03	1.1E+01	2.2E-04	2.4E-04	-	-	6.3E-04	2.8E-04	-	3.2E-02	2.3E+00	1.7E-01	-	1.4E+01	-	-	-	-	-	6.7E-01	2.1E-02	-	-	-	-	3.5E-03
-	-	-	1.3E-03	2.0E+01	-	2.2E-04	-	-	-	3.1E-04	-	7.5E-02	3.5E+00	2.4E-01	-	2.0E+01	-	-	-	-	-	6.7E-01	2.5E-02	-	-	-	-	4.5E-03
-	-	-	1.1E-03	1.2E+01	-	4.7E-04	-	-	1.0E-03	-	-	3.7E-02	2.3E+00	1.8E-01	-	1.2E+00	-	-	-	-	-	6.7E-01	2.1E-02	-	-	-	-	1.0E-02
-	-	-	1.0E-03	1.3E+01	1.9E-04	3.9E-04	-	-	1.3E-03	1.1E-04	-	3.7E-02	2.5E+00	1.7E-01	-	1.4E+01	-	-	-	-	-	5.9E-01	2.1E-02	-	-	-	-	1.0E-02
-	-	-	7.3E-05	2.7E+00	-	-	-	-	6.9E-04	1.9E-04	-	2.0E-03	5.6E-01	1.5E-02	-	3.7E+00	-	-	-	-	-	6.3E-01	4.6E-03	-	-	-	-	1.5E-03
-	-	-	9.0E-03	1.8E+01	-	3.3E-04	-	-	1.6E-03	7.2E-04	-	4.6E-02	2.6E+00	1.5E-01	4.6E-04	1.6E+01	-	-	-	-	-	9.3E-01	2.7E-02	-	-	-	-	1.8E-02
-	-	-	1.2E-03	6.2E+00	-	3.3E-04	-	-	2.8E-03	4.0E-02	-	2.4E-02	1.1E+00	1.1E-01	-	7.7E+00	-	-	-	-	-	5.9E-01	1.6E-02	-	-	-	-	1.0E-02
-	-	-	1.6E-03	1.4E+01	4.6E-05	4.3E-04	-	-	2.5E-03	1.8E-02	-	3.7E-02	2.5E+00	2.1E-01	-	1.4E+01	-	-	-	-	-	7.3E-01	2.3E-02	-	-	-	-	2.1E-02
-	-	-	1.1E-03	1.1E+01	2.2E-04	1.2E-03	-	-	6.9E-03	8.6E-03	-	3.0E-02	2.3E+00	1.5E-01	-	9.8E+00	-	-	-	-	-	6.1E-01	2.0E-02	-	-	-	-	6.1E-02
-	-	-	1.1E-03	6.7E+00	-	-	-	-	2.5E-03	3.5E-02	-	2.1E-02	1.1E+00	1.1E-01	-	8.4E+00	-	-	-	-	-	5.5E-01	1.1E-02	-	-	-	-	2.9E-03
-	-	-	1.4E-03	1.2E+01	2.9E-03	2.8E-04	-	-	3.5E-03	3.7E-03	-	2.5E-02	2.1E+00	1.1E-01	-	1.3E+01	-	-	-	-	-	6.6E-01	1.7E-02	-	-	-	-	1.4E-02
-	-	-	6.4E-04	9.5E+00	8.2E-05	-	-	-	3.4E-03	3.3E-04	-	1.6E-02	1.5E+00	6.5E-02	-	8.6E+00	-	-	-	-	-	5.7E-01	1.6E-02	-	-	-	-	1.5E-02
-	-	-	1.1E-03	9.0E+00	-	3.4E-04	-	-	1.1E-03	4.2E-04	-	2.5E-02	1.8E+00	1.3E-01	-	1.1E+01	-	-	-	-	-	7.3E-01	1.7E-02	-	-	-	-	3.4E-03
-	-	-	1.1E-03	9.8E+00	-	5.5E-04	-	-	7.6E-03	4.7E-03	-	1.7E-02	1.6E+00	9.5E-02	5.4E-04	1.1E+01	-	2.1E-04	-	-	-	5.9E-01	2.0E-02	-	-	-	-	1.8E-03
-	-	-	9.9E-04	1.4E+01	-	4.1E-04	-	-	3.0E-03	3.5E-03	-	3.3E-02	2.1E+00	1.3E-01	4.2E-04	1.2E+01	-	2.7E-04	-	-	-	7.3E-01	3.3E-02	-	-	-	-	1.6E-02
-	-	-	1.4E-03	7.9E+00	7.1E-05	4.8E-04	-	-	1.4E-03	5.4E-04	-	1.6E-02	1.5E+00	1.1E-01	5.0E-04	1.1E+01	-	-	-	-	-	5.8E-01	1.7E-02	-	-	-	-	1.1E-03
-	-	-	1.4E-03	1.7E+01	-	-	-	-	5.4E-03	7.9E-03	-	4.1E-02	2.5E+00	2.0E-01	5.8E-04	1.4E+01	-	-	-	-	-	8.0E-01	2.9E-02	-	-	-	-	4.1E-01
-	-	-	6.4E-04	5.6E+00	-	-	-	-	1.1E-03	6.7E-04	-	1.7E-02	1.0E+00	6.6E-02	-	8.2E+00	-	-	-	-	-	5.3E-01	1.1E-02	-	-	-	-	2.3E-03
-	-	-	1.7E-03	1.3E+01	-	6.8E-04	-	-	2.3E-02	3.2E-03	-	3.5E-02	2.5E+00	1.9E-01	4.6E-04	1.4E+01	-	-	-	-	-	8.7E-01	2.4E-02	-	-	-	-	6.7E-03

Table III.S2

Chapter IV

Stability controls of volcanic ash aggregates against break-up processes

Stability controls of volcanic ash aggregates and break-up processes

Sebastian B. Mueller (1), Ulrich Kueppers (1), Jonathan Ametsbichler (1), Corrado Cimarelli (1), Jonathan P. Merrison (2), Matthieu Poret (3), Fabian B. Wadsworth (1), Donald B. Dingwell (1)

(1) Ludwig-Maximilians-Universität München (LMU), Earth and Environmental Sciences, München, Germany

(2) Aarhus Universitet, Aarhus, Denmark

(3) Istituto Nazionale di Geofisica e Vulcanologia, Bologna section, Bologna, Italy

Scientific Reports 7:7440 (2017)

IV.1 Abstract

Numerical modeling of ash plume dispersal is an important tool for forecasting and mitigating potential hazards from volcanic ash erupted during explosive volcanism. Recent tephra dispersal models have been expanded to account for dynamic ash aggregation processes. However, there are very few studies on rates of disaggregation during transport. It follows that current models regard ash aggregation as irrevocable and may therefore overestimate aggregation-enhanced sedimentation. In this experimental study, we use industrial granulation techniques to artificially produce aggregates. We subject these to impact tests and evaluate their resistance to break-up processes. We find a dependence of aggregate stability on primary particle size distribution and solid particle binder concentration. We posit that our findings could be combined with eruption source parameters and implemented in future tephra dispersal models.

IV.2 Introduction

Numerous investigations, using field, numerical and experimental approaches have extended our understanding of the generation of volcanic ash aggregates (e.g. Schumacher and Schmincke, 1991; Gilbert and Lane, 1994; Schumacher and Schmincke, 1995; Textor et al., 2006 a&b; Brown et al., 2010; Taddeucci et al., 2011; Brown et al., 2012 and references therein; Van Eaton et al., 2012; Telling and Dufek, 2012; Van Eaton and Wilson, 2013; Telling et al., 2013; and Mueller et al., 2016). The control of volcanic ash aggregation on ash plume dispersal has also been demonstrated by field studies (Durant et al., 2009; Watt et al., 2009; Bonadonna et al., 2011) and is now a well-accepted component in numerical modeling of volcanic ash dispersal (e.g. Costa et al., 2006; Costa et al., 2010; Folch et al., 2010; and 2016). However, an understanding of aggregate preservation potential during transport and sedimentation processes is not yet fully understood. Ash is exposed to strongly variable transport conditions that may control aggregation rates (e.g. wind speed, temperature, humidity, acidity, glass content of the ash, particle-particle interaction rates). Nevertheless, the same factors can also control aggregate preservation potential. Disaggregation processes resulting from the elastic mechanical stresses associated with particle-particle interactions may occur both during transport (aggregate-aggregate or aggregate-particle) as well as during sedimentation (aggregate-substrate). There are two key controls on aggregate stability: (1) the properties of the ash particles that form aggregates (i.e. primary particle size, morphology and the aggregate binder agent, e.g. Thornton and Liu, 2004; Bika et al., 2005; and Adi et al., 2011) and (2) aggregate size, shape and roughness. Aggregates fail to remain intact and cohesive if extrinsic elastic stress is higher than the tensile strength of inter-particle contact areas. Analysis of large volcanic aggregates (i.e. mm- to cm-size) from several locations has shown secondary mineral phases like NaCl, $MgSO_4$ or $CaSO_4$ (Sheridan and Wohletz, 1983; Tomita et al., 1985; Gilbert and Lane, 1994; Brown et al., 2010; Scolamacchia and Dingwell, 2014; and Mueller et al., 2016) that act as binding agents between particles. Crack initiation in solid salt bridges may lead either to internal failure of the solid bridge (cohesive failure) or failure of the contact line between solid bridge and particle (adhesive failure; see Mullier et al., 1987). Depending on the initial impact energy, particles may be chipped off from the aggregate surface (low impact energy), the aggregate may fragment into several parts (moderate impact energy) or the aggregate may wholly disaggregate into primary particles (high impact energy; Walker, 1995). Any size reduction process will liberate individual ash particles that subsequently respond in their dispersal behavior based on the aerodynamic properties of single ash shards whose density and drag coefficients differ from those of the prior aggregates. Clearly then, ash aggregation cannot be solely considered as irreversible process that progressively contributes to depletion of airborne ash. The probability of disaggregation processes and resultant influence of locally increased ash concentrations on

bulk ash plume dispersal remains unexplored and is not explicitly implemented in tephra dispersal models.

Recent experimental studies have shown the influence of density instabilities and ash particle concentration (loose, not aggregated) on dispersal and settling behavior (distance from vent and velocity) of volcanic ash (Del Bello et al., 2017; Scollo et al., 2017). From a computational point of view, model results of tephra dispersal and deposition is crucially modified by ash aggregation processes. Neglecting aggregation within a tephra dispersal model may lead to a tephra loading underestimate in proximal area (tens to hundreds of kilometers of distance from the vent) and an overestimate in distal regions (Taddeucci et al., 2011; Mastin et al., 2016). The removal of ash particles from the plume in aggregation events, and the re-release of those ash particles during disaggregation events affects the dispersal and the tephra fallout deposit thickness variations down-wind. Although a variable ash dispersal pattern has been observed and reported for several eruptions and attributed to aggregation processes (Telling et al., 2013; Brazier et al., 1982; Durant et al., 2010; Mastin et al., 2016), this is not necessarily reflected in the fall deposits of the eruption, because disaggregation during deposition can remove the evidence that particles aggregated in the first place (Poret et al., 2017). While the latest models of ash dispersal take ash aggregation into account by solving for advection-diffusion-sedimentation equations in defined meteorological conditions and using input eruption source parameters (e.g., eruption duration, column height, total erupted mass, mass eruption rate, and total grainsize distribution, e.g., Folch et al., 2016; Mastin et al., 2016), no plume model incorporates post-aggregation disaggregation processes. Such plume models incorporate aggregation as an effective aggregated class of particles in the plume (characterized by a diameter d_a and a density ρ_a) in different ways. For example, the Cornell model (Cornell et al., 1983) fills the class with 50% of the 63-44 µm ash particles, 75% of the 44-31 µm and 90% of the smaller than 31 µm. The Sulpizio model (Sulpizio et al., 2012) considers a constant aggregated fraction defined by the user. And the Costa et al. model (Costa et al., 2010; Folch et al., 2016) is more complex and solves for the first order of the Smoluchowski equation (Smochulowski and Veruch, 1917) to estimate the fractions of each gain-size class to remove from the primary particle classes. Software packages such as FPlume (Folch et al., 2016) and FALL3D (Costa et al., 2006; Folch et al., 2009; Folch et al., 2012) have implemented each of these techniques. From these constraints, among the eruption source parameters, aggregation processes are likely to affect the total grain size distribution most substantially, and especially the fine-ash tail of the distribution. This highlights the need to assess the total size distribution, which is representative of bulk tephra deposits.

It's clear that aggregation models are incorporated into plume models. But it is also important to implement disaggregation processes based on both observational and experimental data. Aggregate growth and stability characteristics can be estimated by coupling observations from deposits with *in-situ* observations during eruptions through the application of monitored eruption source parameters (Mastin et al., 2009), such as total grain size distribution or mass eruption rate. We can envisage end member scenarios for the aggregation-disaggregation process in plumes. First, efficient aggregation occurs. This can be because aggregation is efficient while disaggregation is inefficient such that particle fall deposits are modified by the progressive coarsening of the plume load. Second, no net aggregation occurs, which can be because aggregation is inefficient or because disaggregation is more efficient than aggregation. This scenario would result in particle size classes that are either unaffected during classic plume transport, or they are variably aggregated and disaggregated in-plume causing additional complexity in ash dispersal patterns.

Here, we present the results of an experimental campaign in which aggregates, bound by salt bridges at particle-particle contact points (Mueller et al., 2016), have been subjected to impact events at a range of constrained energies. We identify the failure modes and estimate the strength of the aggregates of particles which are crucial parameters for future incorporation of disaggregation processes into tephra dispersal models.

IV. 3 Methods

IV.3.1 Production of sample materials

Experimentally-generated aggregates of 1) soda-lime silicate glass beads and 2) phonolitic Laacher See volcanic ash (Eifel, Germany), were used for the experiments; the granulometry of selected samples was determined using a Coulter LS-230 laser diffraction particle size analyser (Fraunhofer optical model, imaginary/real refractive indices of 0.001 / 1.52 for glass beads and 0.1 / 1.52 for volcanic ash; see Table 1 and Appendix for detailed grain size distribution of experimental materials). Aggregates were produced at *Glatt Ingenieurtechnik GmbH*, Weimar, Germany, by applying fluidization bed techniques with the *Glatt ProCell Lab*®. Particle aggregation was achieved in two steps. First, particles were placed in a vessel and transformed from a deposited state at rest to a fluid-like state in motion through an upwards directed gas-stream, generating a fluidized bed. This lead to effective particle concentrations of 0.003 g cm^{-3}, which relates to dilute and downwind areas of volcanic plumes or lofted plumes coincident with pyroclastic density currents. Humidity was controlled by spraying NaCl-H_2O mixture of various concentration into the fluidized sample via a nozzle (1.0 bar pressure and 8 $ml.min^{-1}$ spray rate) at low spray rate, the NaCl brine is only wetting the particle surfaces, but did not lead to aggregation. At well-controlled temperatures of 25-

110°C, evaporation of the liquid resulted in precipitation of NaCl crystals on particle surfaces with regular, isotropic distribution. Then, de-ionized H_2O was sprayed into the fluidized bed at a significantly higher spray-rate of 50 ml.min^{-1}. Aerosolized liquid droplets deposited on particle surfaces and partially dissolved the previously deposited NaCl crystals. The high amount of liquid in the second step allowed for particles to cluster for longer periods and for aggregates to grow bigger. Capillary forces allowed for the movement of the surficial NaCl brine to particle-particle contact points (Mueller et al., 2017). Upon drying, solid NaCl bridges crystallized and cemented the aggregates. Aggregates strong enough to survive the drying and collection process were able to be collected and analyzed for this study. (See Mueller et al., 2016 for a detailed description of the aggregate production process). Spraying brine liquids simplifies and accelerates the aggregation. When water or acid aerosols condense on ash particles, leaching will cause various elements to be transported to the surface of the grains where they will form precipitates and bind aggregates. While these two processes (acid-driven leaching and salt precipitation and brine evaporation driven salt precipitation) are subtly different, they both produce salt-bound aggregates.

Several types of aggregates can be produced by the above method (Table IV.1). Glass bead aggregates are composed of primary particle sizes of < 50 µm, 40-70 µm or < 70 µm and are bound with NaCl concentrations of 2, 5 or 15 g.kg^{-1}, respectively. Volcanic ash aggregates are comprised of primary particle sizes < 40 µm, 40-90 µm or < 90 µm and are bound with NaCl concentrations of 5, 10, 15 or 20 g.kg^{-1}, respectively.

Primary particle material	Primary particle size distribution	NaCl [g kg^{-1}]
Laacher See Ash	< 40 µm	5
Laacher See Ash	< 40 µm	10
Laacher See Ash	< 40 µm	20
Laacher See Ash	40-90 µm	20
Laacher See Ash	< 90 µm	10
Laacher See Ash	< 90 µm	15
Laacher See Ash	< 90 µm	20
Soda-lime glass beads	< 50 µm	5
Soda-lime glass beads	< 50 µm	15
Soda-lime glass beads	40-70 µm	2
Soda-lime glass beads	40-70 µm	5
Soda-lime glass beads	40-70 µm	15
Soda-lime glass beads	< 70 µm	2
Soda-lime glass beads	< 70 µm	5
Soda-lime glass beads	< 70 µm	15

Table IV.1: Overview of characteristics of artificially produced aggregates used for impact experiments.

Efficient binding of volcanic ash was found to be impossible at concentrations of 2 $g.kg^{-1}$ due to the higher specific surface area of the starting material (see also Mueller et al., 2016, 2017).

NaCl concentration ($g.kg^{-1}$) of artificial aggregates used for stability experiments were determined by aqueous leaching. The leaching protocol requires a solid solution mass ratio of 1:10 and measured the effective NaCl concentration of particle surfaces via electrical conductivity measurements with an *inoLab Cond 730®*, manufactured by *Wissenschaftliche Technische Werkstätten GmbH*, Germany. The instrument was calibrated using H_2O-NaCl solutions of known concentration. NaCl coating of particle surfaces and hence NaCl concentrations of *ProCell Lab®* aggregates are reproducible within 3% error (Mueller et al., 2016). Scanning Electron Microscopy (SEM) was carried out at LMU Munich using a *Hitachi SU 5000* and at the HT-HP lab of INGV Rome, using a *JEOL JSM-6500F*.

IV.3.2 Impact testing

Two experimental setups were designed to investigate the modes of breaking behavior of aggregates and the aggregate strength. Setup 1 was built at the *Mars Laboratory Simulation Laboratory* at Aarhus University, Denmark. An over-pressurized nozzle (50-400 kPa) propelled individual volcanic ash aggregates (particle sizes < 90 µm with 20 $g.kg^{-1}$ NaCl) against a vertical target wall aligned perpendicular to the aggregate flight path. The impact was recorded with a *Phantom v710* high-speed camera (Fig. IV.1a). Varying the overpressure condition at the nozzle, we investigated a range of impact velocities for which we observed different modalities of aggregate breakup upon impact such as surface chipping, fragmentation and total disintegration (Fig. IV.1b). Setup 2, built at LMU Munich, Germany, aimed at investigating the aggregate strength by free-fall experiments. Individual aggregates were dropped from a height *h* onto a metal plate (Fig. IV.1c). These experiments were designed to evaluate the effect of particle size distribution (PSD), shape and surface morphology of primary particles and binder concentration on aggregate stability. We performed these experiments on artificial aggregates only as young natural ash aggregates are rare and even the youngest (Burns et al., 2017) have likely already undergone further post-depositional (re-)crystallization, e.g. by growth of zeolites.

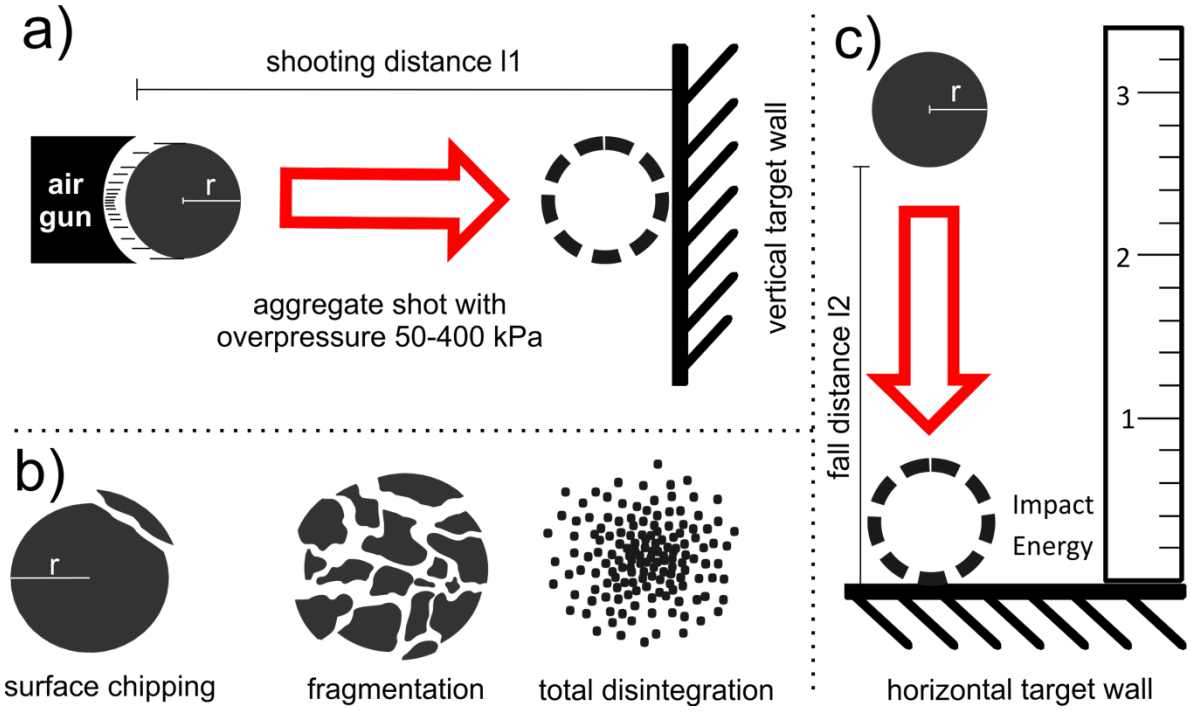

Figure IV.1: a) Pressurized air-gun setup at Aarhus University, Denmark. Aggregate was shot with overpressure against a vertical metal wall. Applied overpressures ranged between 0.5 and 4 bar, resulting in impact velocities of 2.9-7.8 m.s^{-1}. b) Impact setup at LMU Munich, Germany. Aggregates were dropped from heights between 5 and 200 cm onto a metal plate. Impact speed was monitored with a high-speed camera and used to calculate impact energy. c) Modes of break-up that were observed throughout experiments: surface chipping (<10 wt% loss of material from parent aggregate), fragmentation (10-90 wt% material loss from parent aggregate) and total disintegration (> 90 wt% material loss from parent aggregate).

Following a pre-established framework (Mueller et al., 2015) allowed us to parameterize the potential, kinetic and loss-during-flight (atmospheric) energies of particles during both horizontal (Setup 1) and vertical (Setup 2) experiments. For a quantitative approach, potential energies E_{P} of the aggregates were calculated and used to estimate kinetic energies E_{K} of the samples during impact. During fall, samples will lose energy due to drag, an energy loss which we term a loss energy E_{L}. These energy scalings are given by Equation IV.1:

$$\left.\begin{aligned} E_{\mathrm{P}} &= m_i g h \\ E_{\mathrm{K}}|_{l=l_1} &= \frac{1}{2} m_i v_i^2 \\ E_{\mathrm{L}} &= A c_w \frac{\rho}{2} v_i^2 \end{aligned}\right\} \qquad \text{(Equation IV.1)}$$

where m_i is the initial sample mass, g is the acceleration due to gravity, v_i is the impact velocity of the sample, A is the cross sectional area of sample, c_w is the drag coefficient and ρ is sample density. Here, we define $l = l_i$ as the distance in flight from the launch position at which impact occurs. Impact velocities were measured by analysis of high-speed video-

records. Calculated atmospheric loss energies E_L lead to a median loss of initial potential energies of ~11.5% for glass bead aggregates and ~15.7% for volcanic ash aggregates, which is in good agreement with atmospheric losses of ~15% reported by Mueller et al. (2015) during drop experiments of larger volcanic clasts.

For each of the 14 aggregate groups displayed on Table 1, 20 drop experiments with 20 aggregates were performed. Impact velocities varied between 1 and 6 m.s^{-1}. Maximum fall height *h* (between 0.05 m and 2 m) was chosen according to aggregate stability. If a sample was disintegrated completely, *h* was not increased further. Mass m_i of each sample was evaluated before the fall experiment with a *Sartorius MC 210 P* balance with an accuracy of 10^{-8} kg. Aggregates for each experimental setup selected to be in a mass range of $\pm$ 10 wt%. After impact, the mass m_f of the largest remaining aggregate fragment was evaluated and compared with the initial mass of the aggregate by m_f/m_i. Based on this ratio, aggregates were categorized into three groups, 'chipping surface' (i.e. $m_f/m_i = 0.9$), 'fragmented' (i.e. $0.1 < m_f/m_i < 0.9$) and 'total disintegration' (i.e. $m_f/m_i < 0.1$). See Appendix for the complete dataset.

IV.4 Results

A total of 280 aggregates for the drop experiments were chosen to be consistent in mass to facilitate dataset comparison. On average, the aggregate mass m_i was 1.4 mg with a standard deviation of 0.16 mg. High-speed videos reveal different break-up behavior as a function of impact velocity ranging between 2.9-7.8 m.s^{-1} as summarized in Fig. IV.2. Experiments with a nozzle overpressure of 50 kPa lead to surface chipping (Fig. IV.2a), with the aggregate remaining mostly intact after impact. Experiments with 200 kPa overpressure resulted in further fragmentation of the aggregate, with largest fragments showing up to 5 wt.% of the parental aggregate (Fig. IV.2b). Overpressure experiments of 400 kPa led to total disintegration of the aggregate, no fragments could be observed in the high-speed video or recovered from the ground after the experiment (Fig. IV.2c).

We used our data to evaluate and isolate the effects of binder (NaCl) concentration, particle-size and of particle roughness on the energy required to break-up aggregates. In general, larger primary particle sizes produced stronger aggregates that required higher break up energies. Fig. IV.3a shows glass bead aggregates bound with 5 g.kg^{-1} NaCl. In this dataset, higher impact energies were necessary to fragment aggregates consisting of coarse glass bead sizes (40-70 µm) compared with those consisting of fine glass bead sizes. Equivalent results can be seen for the volcanic ash aggregates (Fig. IV.3b), in which samples with coarse particle fractions (40-90 µm and < 90 µm) needed higher impact energies to fragment than the volcanic ash aggregates of the same salt concentration but a primary particle size distribution

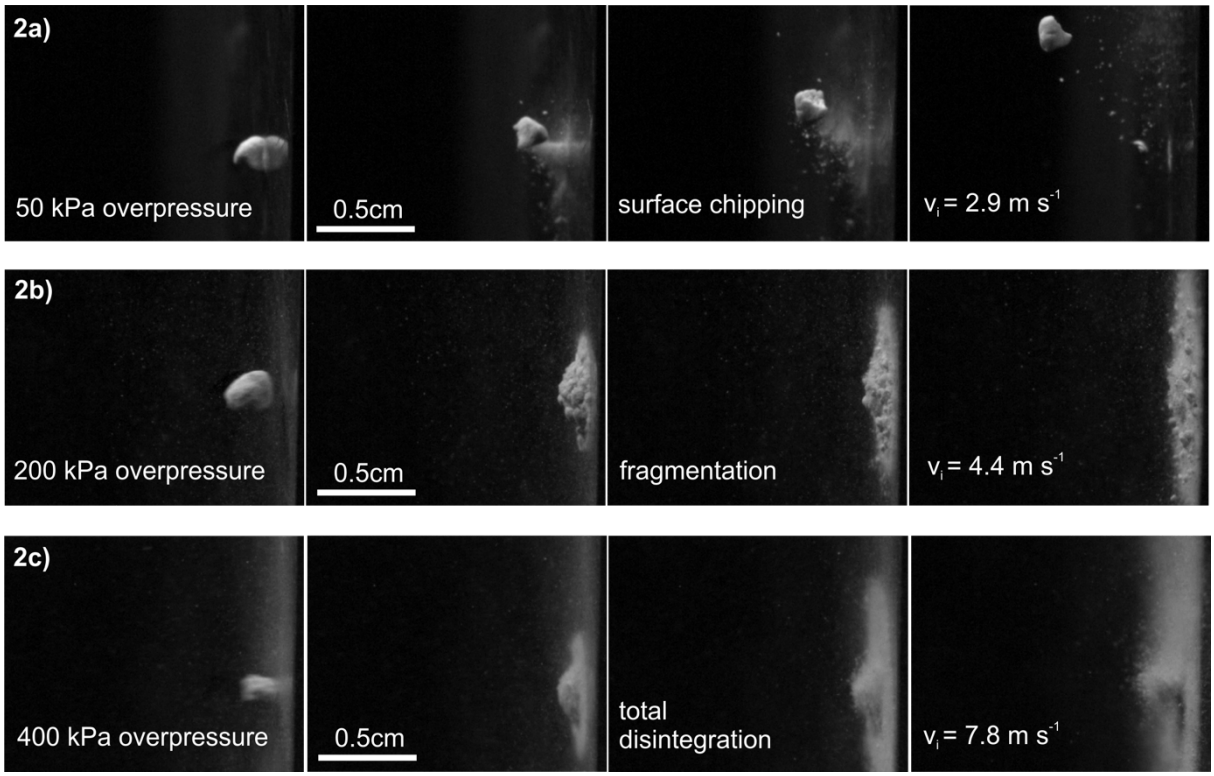

Figure IV.2: Sequence of photos taken with a high-speed camera; aggregates impact on metal wall of the Aarhus setup. 2a) sequence shows surface chipping of aggregate, 2b) fragmentation and 2c) total disintegration.

of < 40 µm. Further, volcanic ash aggregates with coarse primary particles either show surface chipping (left gray field) or fragmentation (center gray field), whereas volcanic ash aggregates with only fine primary particles mainly show total disintegration and at lower impact energies. Overall a clear positive effect of larger particle size distribution on aggregate stability could be observed for both glass bead and volcanic ash aggregates. We report the complete dataset in the Appendix.

In a second experimental suite, we compared the stability of aggregates bound by different NaCl concentrations but having the same primary particle size distribution. Higher NaCl concentrations in the bridges between particles conferred greater stability to the aggregates. Glass bead aggregates of the same primary particle sizes (< 70 µm) require higher impact energies in order to breakup if there is more NaCl binding the particles (Fig. IV.3c). Trends become even more clear for the volcanic ash aggregates (Fig. IV.3d). Here, not only higher impact energies are required to break aggregates with higher NaCl concentrations, but also the breakup behavior changes. Approximately 75% of the tested samples with high binder concentration (20 $g.kg^{-1}$) exhibit surface chipping upon impact, whereas samples with comparatively low NaCl content (10 $g.kg^{-1}$) undergo fragmentation or total disintegration.

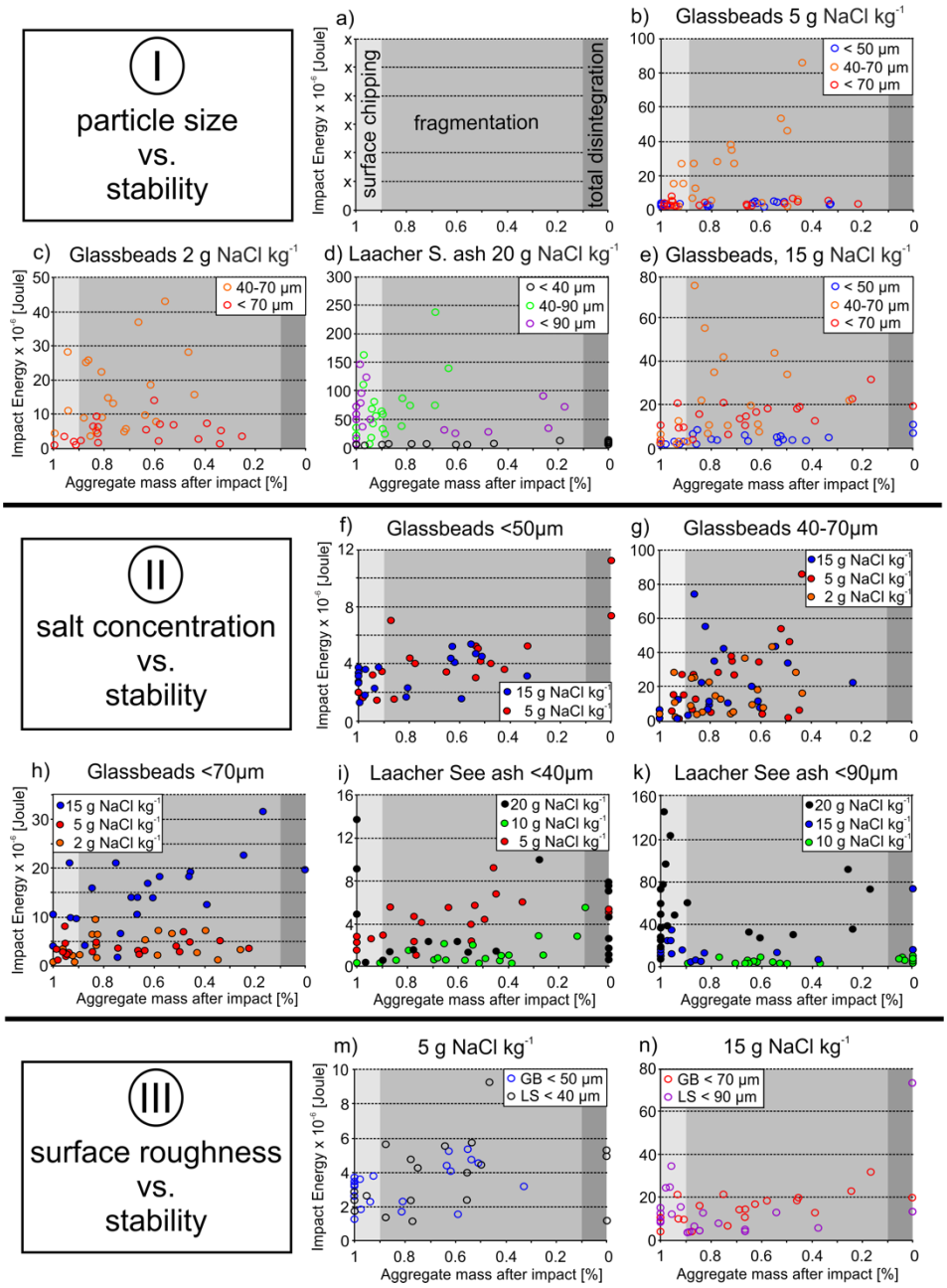

Figure IV.3: Contemplation of impact results at LMU Munich setup. Each graph shows calculated impact energies of aggregates and the remaining aggregate mass after impact. Remaining mass > 0.9 stands for surface chipping (light gray background), mass 0.1-0.9 for fragmentation (medium gray background) and mass < 0.1 for total disintegration (dark gray background). a) shows breakup classes of aggregates. b) IV BC of 2 $g.kg^{-1}$. e) compares LSA with PPSDs of < 40, 40-90 and < 90 µm and a BC of 20 $g.kg^{-1}$. f) compares glass bead aggregates (GBA) with a primary particle size distribution (PPSD) of < 50 µm and binder concentrations (BC) of 5 and 15 $g.kg^{-1}$. g) compares GBA with a PPSD 40-70 µm and a BC of 2, 5 and 15 $g.kg^{-1}$. h) compares GBA with a PPSD < 70 µm and a BC of 2, 5 and 15 $g.kg^{-1}$. i) compares Laacher See ash aggregates (LSA) with a PPSD < 40 µm and a BC of 5, 10 and 20 $g.kg^{-1}$. k) compares LSA with a PPSD < 90 µm and a BC of 10, 15 and 20 $g.kg^{-1}$. m) compares GBA and LSA with PPSDs of < 50 and < 40 µm and a BC of 5 $g.kg^{-1}$. n) compares GBA and LSA with PPSDs of < 70 and < 90 µm and a BC of 15 $g.kg^{-1}$.

We conclude that the salt budget available for particle-particle binding increased aggregate stability against breakup processes.

A final suite of drop experiments was conducted to investigate in the effect of surface morphology of primary particles on aggregate strength. No clear effect was empirically obvious. Stability of glass bead aggregates (spherical primary particles) and volcanic ash aggregates (angular, irregular primary particles) with the same NaCl concentrations do not reveal any difference in the breakup behavior or impact energies required for breakup (Fig. IV.3e). We conclude here that particle morphology is a second order control on aggregate stability and that spherical assumptions can be made for the mechanical stability of volcanic ash aggregation.

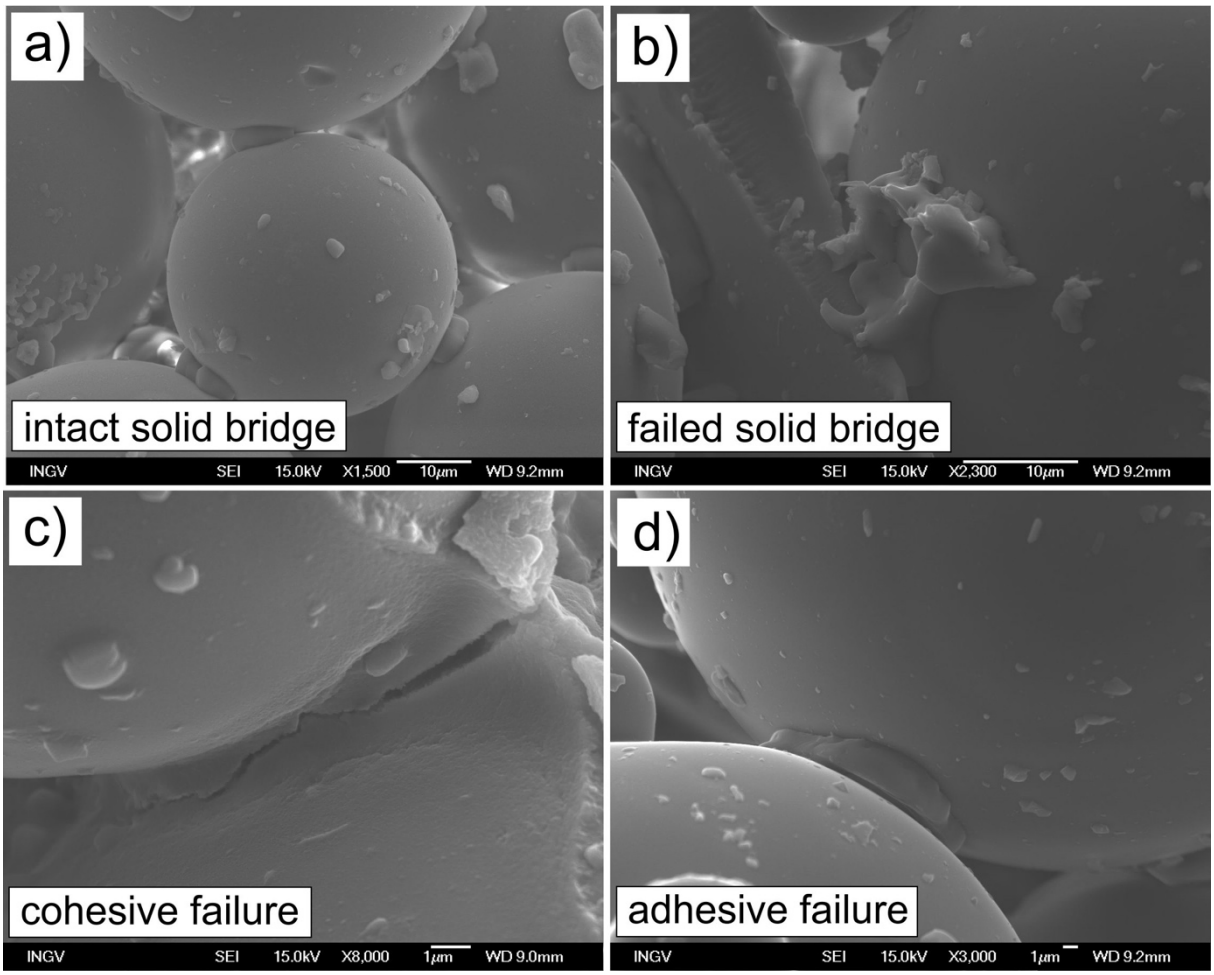

Figure IV.4: a) shows an intact solid NaCl bridge connecting two glass beads. b) shows a failed solid NaCl bridge with the once connected glass bead missing. c) shows cohesive failure within a solid NaCl bridge. d) shows adhesive failure between a solid NaCl bridge and a glass bead.

Scanning electron microscopy (SEM) provides insights into the size and geometry of NaCl crystals as well as their failure mode upon breakup. This analysis shows (i) intact bridges

(Fig. IV.4a), (ii) failed bridges (Fig. IV.4b), (iii) bridges with cracks (i.e. cohesive failure, Fig. IV.4c) or (iv) cracks between bridge and solid particle (i.e. adhesive failure, Fig. IV.4d). Salt bridge volumes were estimated by measuring visible horizontal and vertical axes assuming cuboid growth valid for NaCl crystals. In reality there are deviations from cuboid geometry, conferring minor error on our salt bridge volume estimates. Nevertheless, we observed a positive correlation between salt crystal length and particle radius suggesting that bridge thickness scales with average particle size (Fig. IV.5).

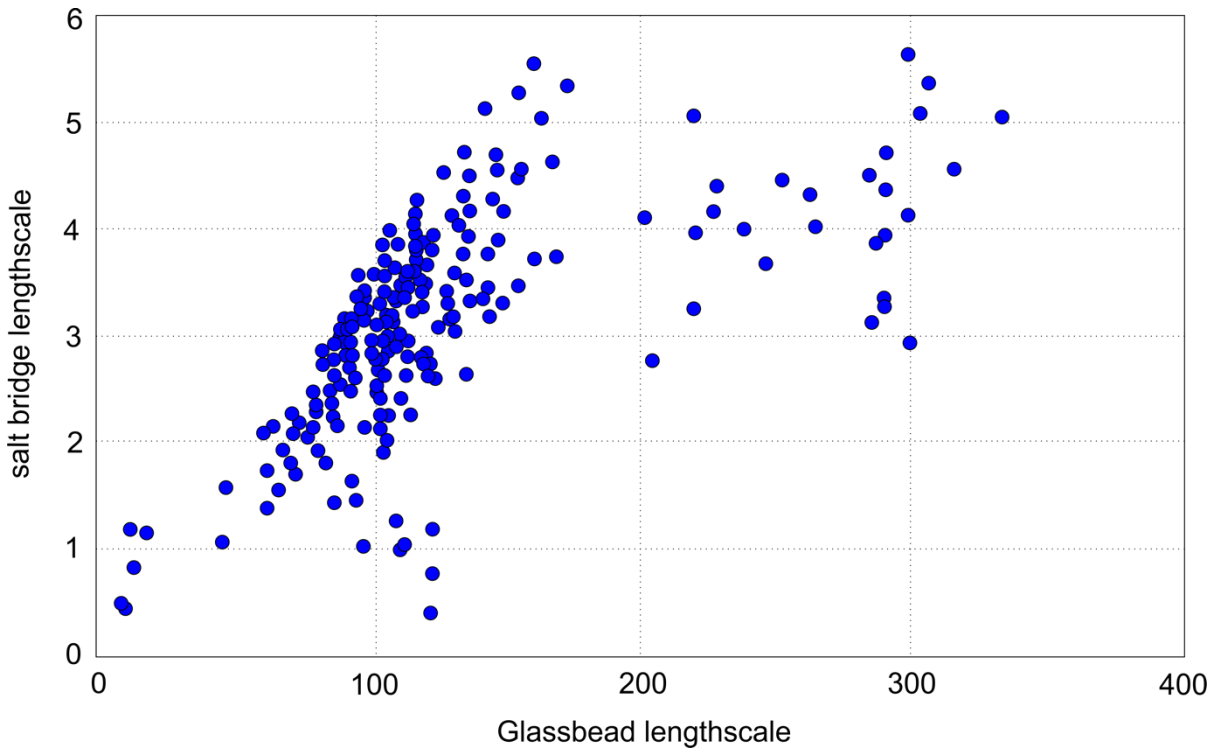

Figure IV.5: Solid NaCl bridge volumes evaluated from SEM analysis are plotted against total available surface of the two particles connected through the solid bridge. Maximum salt bridge volumes show exponential dependency on available particle surface area.

IV.5 Analysis and discussion

Once formed, aggregates can break up in three different micromechanical ways: (1) surface chipping, (2) fragmentation into smaller aggregate pieces, or (3) total disintegration into particle sizes comparable to the primary ones. In volcanic ash plumes, total disintegration, the most efficient process in releasing primary particles back into the plume, could result in re-entrainment of fine ash particles in the plume dispersal trajectory. We show that the mode of aggregate break-up depends on both bulk stability of the aggregate and on the impact energy. Previous discrete element method simulations, as well as experiments, have shown that aggregates impacting a solid wall generate multiple branches of cracks that dynamically propagate inside the aggregate, causing break up of solid bridges between primary particles

(Antonyuk et al., 2006). The propagation of the cracks depends primarily on the impact energy. While the propagating master cracks cause the aggregate to break-up into fragments, areas of high crack density are also the regions from which primary particles are released.

Impact energies between two aggregates or an aggregate and a clast cannot be easily predicted for volcanic plume conditions. A readily calculable constraint of impact energy for volcanic particles or aggregates in a plume is the energy at terminal velocity, which depends on the mass of particles or clasts via Eq. IV.2:

$$v_t = \sqrt{\frac{2mg}{c_w \rho A}} \qquad \text{(Equation IV.2)}$$

with the mass m, gravity g, drag coefficient c_w, aggregate or particle density ρ and cross sectional area of aggregate or particle A. Terminal fall velocities were reached or exceeded only in our experimental setup 1, and not in setup 2, due to insufficient fall distances. Nevertheless, total disintegration was routinely observed at impact velocities below v_t.

Our experimental results illustrate that aggregates with small primary particle sizes (e.g. < 50 µm) are less stable than aggregates with large primary particle sizes (e.g. 40-70 µm). Aggregation in natural volcanic environments rarely exceeds an upper limit in particle size of 200-250 µm (Brown et al., 2012; Cole et al., 2001); however, primary particles larger than 200 µm have been shown to incorporate in oversaturated (wet) pockets of the solid/liquid mixture, simulating mud drops (Van Eaton et al., 2012). Our SEM observations of solid salt bridges cementing analogue glass bead aggregates shows a clear dependence of salt bridge volume on available primary particle surface area (Fig. IV.5). This relationship can be explained in the context of previous work (Mueller et al., 2017) that shows how surface liquids such as H_2O may dissolve salt crystals and create a salt brine. The capillary forces at the contact line between the liquid and the particle cause migration of the salt brine to liquid bonding points between two particles, bunching the liquid in collars around particle-particle contacts. The amount of re-mobilized surficial salt deposits depends on the available catchment area, i.e. the cumulative surface of primary particles. Large, voluminous salt bridges can be formed if the catchment area is significantly large and the number of contact points is small. Two 50 µm glass beads can be cemented by one much larger salt bridge than two glass beads with 10 µm diameter (see also Fig. IV.6). Generally speaking, the size of salt bridges depends on the connection density, i.e. whether there are many or just few other glass beads connected with each other. This also translates into a higher probability of large salt bridges in aggregates formed from a monodisperse starting particle size distribution and explains why aggregates containing very fine particles (0-40 µm) relative to the mean particle size (highly polydisperse distributions) proved to be comparatively less stable upon impact. In the case in which a large

glass bead is connected with many other glass beads, the total available surface salt is probably separated into several contact points, where, at comparable available salt volume, smaller individual salt bridges will crystallize. Salt will also be re-mobilized on ash particles; however, given the more irregular shapes of ash grains, the number of contact points is probably higher than between spheres, producing a relatively weaker connection. However, the effect of complex surface morphologies allows for mechanical interlocking of ash grains adding to the bulk mechanical strength. Indeed, we observed comparable aggregate strengths for ash and glass-bead aggregates with similar binder concentration and particle-size distribution (see Fig. IV.3).

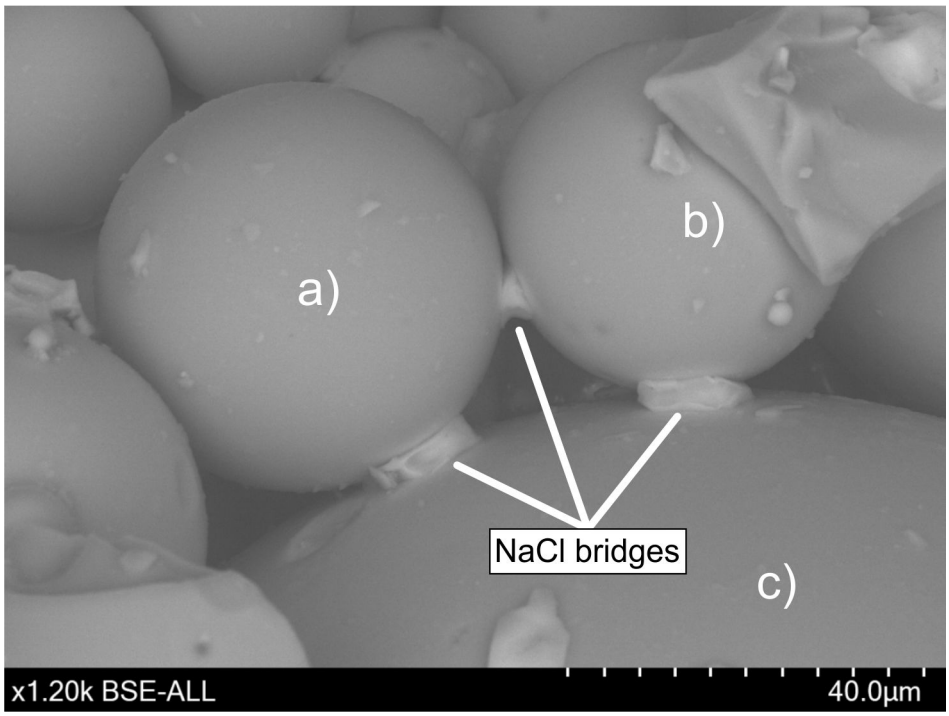

Figure IV.6: SEM image of aggregated glass beads. The two glass beads a) and b) are connected with each other through a smaller solid NaCl bridge than they are to glass bead c). Glass bead c) is larger in volume and therefore surface and allows for the establishment of more voluminous bridges.

The strength of aggregates can be calculated based on forces required to separate two particles connected through a solid bridge for a given size, volume and strength. Models, such those proposed by Rumpf (1975) or by Johnson et al. (1971) assume breakage of solid salt bridges to occur at the neck of a bridge – the area with the smallest diameter – which is termed cohesive failure. Contrastingly, adhesive failure occurs by the separation of the contact point between the solid bridge and the primary particle (Fig. IV.4). The diameter of the bridge neck increases with time as capillary forces drive more brine liquid to the contact zone, bunching up a collar of liquid which, upon drying, precipitates a binding crystal assemblage. Therefore,

the force *F* required to separate two particles connected by a solid bridge increases with an increasing neck diameter and can be calculated with a simple micromechanical scaling:

$$F \approx \pi r_{sb}^2 \sigma_{sb} \qquad \text{(Equation IV.3)}$$

where r_{sb} is the radius of the narrowest bridge part (the neck) and σ_{sb} is the neck strength (Bika et al., 2005). Bonding strengths of various salts, σ_{sb}, including NaCl have been experimentally investigated (Jeremic, 1994). Average tensile and compressive bonding strengths of crystallized NaCl compounds are reported to be between 0.2 MPa (tensile) and 30 MPa (compressive). The force required to break the neck region F, can then be applied to the model of Rumpf (1975) in which the overall aggregate strength is calculated by scaling neck strengths to the porosity of the aggregate:

$$\sigma_{cr} = z(\varepsilon) \frac{F}{d_p^2} \qquad \text{(Equation IV.4)}$$

where d_p is the whole aggregate diameter and z is a function dependent on porosity ε, given in turn by

$$z(\varepsilon) = (1 - \varepsilon)/\varepsilon \qquad \text{(Rumpf, 1975, Equation IV.5)}$$

Bika et al. (2005) pointed out that the major challenge in applying micromechanical views of disaggregation processes lies in the uncertainty in neck diameters of the solid bridge. Here, we directly observe maximum bridge length scales and compare them with particle radius (Fig. IV.5). Using the constraints from our experimental samples, we demonstrate end-member solutions to equations 3-5, in which we show how the strength scales with neck radius (100 nm and 12.5 µm evaluated from SEM data, Fig. IV.5) in some scenarios of two different aggregate porosities of 0.8 and 0.5 which reflect the densities measured for our artificial samples. Lowest aggregate strengths of up to 25 Pa are calculated for the tensile stress and high porosity (0.8) case, whereas the highest aggregate strength of up to 15 kPa can be computed for a compressive stress and the low porosity (0.5) case (Fig. IV.7). Although the calculated aggregate strengths are based on glass bead aggregates and their solid bridge values, we assume very similar strength values for ash aggregates. Low aggregate strengths (1 mPa to a few Pa) are typical of aggregates with fine primary particle sizes (<40 µm for ash and <50 µm for glass beads), and with high strengths are consistent with aggregates composed of coarse primary particle sizes (up to 90 µm) that are capable of generating larger solid salt bridges. Consequently, one implication is that aggregation of fine ash alone will produce the weakest aggregates and therefore it is fine-grained material is most likely to be disaggregated upon impact and re-suspended in dynamic plumes. Also, accretionary lapilli containing ash particles < 40 µm (as used in the experiments) have never been documented in nature which

supports the theory that they either don't survive the plume or they don't last long enough after sedimentation to be measured.

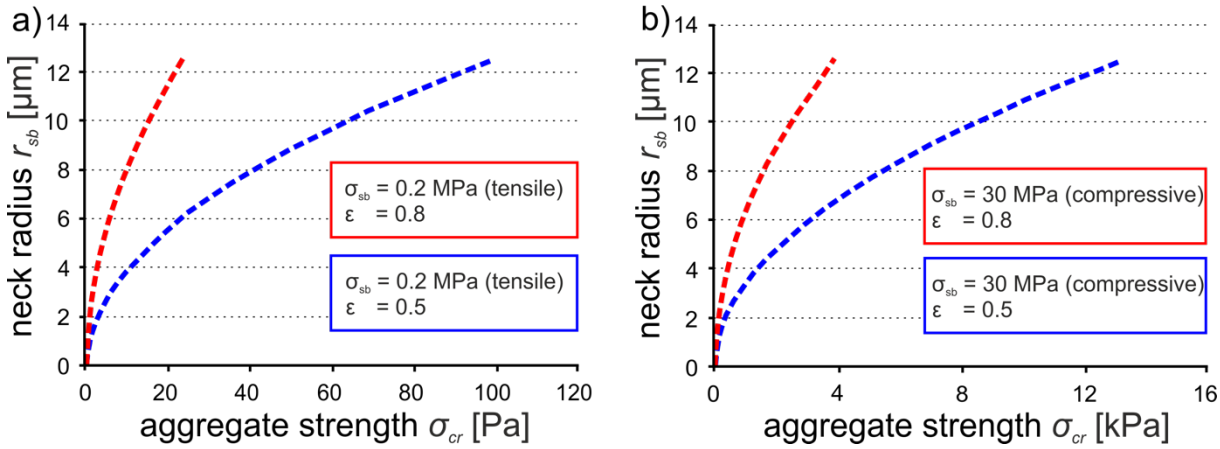

Figure IV.7: Aggregate strength σ_{Cr} of artificial aggregates have been computed, following the models of Johnson et al. (1971) and Rumpf (1975). Solid salt bridge neck radii represent SEM analysis results or our artificial aggregates. a) shows aggregate strengths for tensile stress case and aggregate porosities ε of 0.5 and 0.8. b) shows aggregate strengths for compressive stress case and aggregate porosity of 0.5 and 0.8.

IV.6 Relevance to natural processes and implications

Aggregation models in plume simulations are not based on either the physical description of aggregation growth (Costa et al., 2012; Folch et al., 2016) or the bulk approach (Mastin et al., 2016; Cornell et al., 1983; Sulpizio et al., 2012; Bonadonna et al., 2002) which is focused on the field deposit. The full description of the aggregation processes confers a high computational cost. To reduce the computational cost, the models are set up to calculate the aggregate contribution and its distribution by pre-aggregating the erupted mixture. While the models are used to fit deposits, they often require tuning via inversion methods to capture the aggregated contribution observed. This implies that the tuning procedure applied in modelling plume aggregation is an approximate method of accounting for the bulk effect of aggregation and disaggregation. A full implementation of disaggregation within tephra dispersal models requires a constitutive understanding of how aggregation and post-aggregation disaggregation occurs during eruptions. This study aims to highlight the feasibility of developing a first such constitutive law for disaggregation impact energies at experimental Reynolds numbers < 500 (Mueller et al., 2016), velocity of the bulk airflow 0.15-0.22 m/s (Mueller et al., 2016), environmental temperature of 40-60 °C, and bulk ash density 900 kg/m^3. At these conditions, impacts lead to surface chipping, fragmentation and total disintegration within the plume. To go towards the full characterization of the tephra transport and its sedimentation, it would be useful to assess disaggregation rates in real meteorological

conditions (e.g. wind, temperature, air moisture profiles) and at real mass eruption rates, eruption durations and airborne ash mass.

While this study highlights the importance of considering aggregation processes within a model of plume dispersion and sedimentation, we have demonstrated that aggregates can disintegrate if impact energies are sufficient (Taddeucci et al., 2011). Bonadonna et al., 2011 indeed show that tephra fall deposits from the 2010 Eyjafjallajökull eruption (Iceland) were found to be enriched with fine ash in proximal areas, in combination with deposited aggregates, suggesting that upon aggregation-induced sedimentation from the plume, aggregate break-up on impact skewed the particle size distributions measured.

In this study, we have presented insights into the influence of primary particle size distribution, surface morphology and binder concentration on aggregate stability. Mueller et al., 2016 have additionally described the effect of primary particle size distribution, effective particle concentration, humidity and binder concentration on aggregation efficiency. Together these experimental datasets illustrate that fine particles (e.g. ash < 40 µm) are much more efficient (up to 100%) in their aggregation rate than coarse particles (e.g. ash 40-90 µm), but are also much more prone to subsequent break-up due to their low comparative stability.

IV.7 Conclusion

This study evaluated the stability of aggregates produced artificially from analogue soda-lime silicate glass beads and natural volcanic ash. NaCl was used as binding agent. Impact experiments demonstrated the influence of (1) primary particle size distribution, (2) particle surface area and morphology and (3) binder concentration on aggregate stability. Salt bridge volumes of glass bead aggregates obtained via Scanning Electron Microscopy were used for numerical calculations of aggregate strength, computed to be in the range of < 1 Pa up to several 100 Pa. Notably, coarse-grained aggregates (made of primary particles > 50 µm) exhibit a significantly increased stability compared with fine-grained aggregates. Aggregates with small primary particle size (<50 µm) are up to one order of magnitude weaker than aggregates with larger primary particle size (>50 µm). Current tephra dispersal models regard aggregation of ash as irrevocable leading to sedimentation and removal from the atmosphere[19] without explicitly estimating the disaggregation contribution. Here, we have presented quantitative data on disaggregation that can be used for further work investigating potential links with eruption source parameters which are required for numerical ash plume dispersal forecasting. In combination with other experimental studies, it is now possible to attribute disaggregation processes to eruption parameters such as mass eruption rate, eruption intensity, total grain-size distribution, degassing rate and magma composition, or to meteorological parameters such as air moisture and temperature, or to other particle

parameters such as primary particle size distribution, effective particle concentration, binder concentration, Reynolds number of the solid/gas system and exposure time.

IV.8 Acknowledgements

This work is supported by the Marie Curie Initial Training Network 'VERTIGO', funded through the European Seventh Framework (FP7 2007-2013) under Grant Agreement number 607905. We are indebted to Jacopo Taddeucci for acquiring SEM images and to Glatt Ingenieurtechnik GmbH, particularly to Michael Jacob, Ulrich Walter and Katja Oppermann for their support. The Laacher See ash used in this study was provided by ROTEC GmbH & Co. KG (Mühlheim-Kärlich, Germany). C.C. acknowledges the support of the AXA Research Fund grant 'Risk from volcanic ash in the Earth system'. D.B.D. acknowledges the support of the European Research Council Advanced Grant 247076 'EVOKES' (Explosive volcanism in the Earth System).

IV.9 Author Contributions

S.B. Mueller and U. Kueppers produced artificial aggregates. S.B. Mueller, J. Ametsbichler, U. Kueppers and J.P. Merrison performed impact experiments. S.B. Mueller and C. Cimarelli carried out SEM analysis. All authors interpreted the data and worked on the finalization of the manuscript.

Chapter V

Aggregation in particle rich environments: a textural study of examples from volcanic eruptions, meteorite impacts and fluidized bed processing

Aggregation in particle rich environments: a textural study of examples from volcanic eruptions, meteorite impacts and fluidized bed processing

Sebastian B. Mueller (1), Ulrich Kueppers (1), Matthew S. Huber (2, 3), Kai-Uwe Hess (1), Gisela Poesges (4), Bernhard Ruthensteiner (5), Donald B. Dingwell (1)

(4) Ludwig-Maximilians-Universität München (LMU), Earth and Environmental Sciences, München, Germany

(5) University of the Free State, Bloemfontein, South Africa

(6) Vrije Universiteit Brussel, Brussels, Belgium

(7) Ries Krater Museum Nördlingen, Germany

(8) Zoologische Staatssammlung München, München, Germany

Bulletin of Volcanology 80:32 (2018)

V.1 Abstract

Aggregation is a common process occurring in many diverse particulate gas mixtures (e.g., those derived from explosive volcanic eruptions, meteorite impact events and fluid bed processing). It results from the collision and sticking of particles suspended in turbulent gas/air. To date, there is no generalized model of the underlying physical processes. Here, we investigate aggregates from 18 natural deposits (16 volcanic deposits and two meteorite impact deposits) as well as aggregates produced experimentally via fluidized bed techniques. All aggregates were analyzed for their size, internal structuring and constituent particle size distribution. Commonalities and differences between the aggregate types are then used to infer salient features of the aggregation process. Average core to rim ratios of internally structured aggregates (accretionary lapilli) are found to be similar for artificial and volcanic aggregates but up to an order of magnitude different than impact related aggregates. Rim structures of artificial and volcanic aggregates appear to be physically similar (single, sub-spherical, regularly-shaped rims) whereas impact-related aggregates more often show multiple or irregularly-shaped rims. The particle size distributions (PSDs) of all three aggregate types are similar (< 200 µm). This proves that in all three environments, aggregation occurs under broadly similar conditions despite the significant differences in source conditions (particle volume fraction, particle size distribution, particle composition, temperature), residence times, plume conditions (e.g., humidity and temperature) and dynamics of fallout and deposition. Impact-generated and volcanic aggregates share many similarities, and in some cases may be indistinguishable without their stratigraphic context.

V.2 Introduction

Particle aggregation is a common feature in nature and technology. It has been observed in deposits of volcanic eruptions (e.g. Self, 1983; Hayakawa, 1990; Schumacher and Schmincke, 1991; De Rita et al., 2002; Branney et al., 2008; Brown et al., 2012; Van Eaton and Wilson, 2013; Scolamacchia and Dingwell 2014) and meteorite impacts (e.g., Graup 1981; Alegret et al., 2005; Pinto and Warme 2008; Cannon et al., 2010; Rocholl et al., 2011; Branney and Brown, 2011, Huber and Koeberl 2017) as well as in powder processing technologies (e.g. Salman et al., 2006). Several phenomena promote the aggregation of suspended particles, including, 1) electrostatic forces (e.g. James et al. 2002, Bonadonna et al. 2012, Del Bello et al. 2015), 2) liquid bonding or freezing (e.g. Tomita et al. 1985, Gilbert and Lane 1994, Bonadonna et al. 2002, Durant et al., 2009, Van Eaton et al. 2012, Mueller et al. 2016), and 3) the growth of secondary mineral phases (Sheridan and Wohletz 1983, Gilbert and Lane 1994; Brown et al. 2010; Scolamacchia and Dingwell 2014; Mueller et al. 2016). Although the same underlying physical and chemical phenomena may occur in all environments under consideration here (volcanic eruptions, meteorite impacts, experiments), the aggregate P-T growth conditions, growth rates and preservation potential are likely to differ significantly depending on their petrogenesis.

Throughout this paper, we describe the different sample types in the following order, a) volcanic, b) meteorite and c) experimental.

V.2.1 Volcanic ash aggregates

Explosive volcanic eruptions can inject large volumes of volcanic ash into the atmosphere. Under certain circumstances, ash can cluster together and form aggregates, which have been documented in many deposits (e.g. Van Eaton and Wilson 2013; Wallace et al. 2013; Scolamacchia and Dingwell 2014) and there is growing evidence that aggregation is the norm rather than the exception (e.g. Brown et al. 2012). Observations of aggregate fallout indicate that many aggregates do not survive transport and/or sedimentation (e.g. Taddeucci et al. 2011; Bonadonna et al. 2011; Bagheri et al. 2016; Mueller et al. 2017a), and this has also been inferred from modeling and observations of secondary thickness maxima in ash deposits (Durant et al. 2009). Larger and strongly bonded aggregates, such as accretionary lapilli, do survive transport and deposition processes and are commonly preserved in deposits as, for example in deposits of the eruptions of Tungurahua volcano, Ecuador (Kueppers et al. 2016), Soufriere Hills volcano, Montserrat (Burns et al. 2017), and Volcán de Colima, Mexico (Reyes-Dávila et al. 2016), as well as many others (e.g. Brown et al. 2012).

Volcanic ash aggregation strongly influences ash dispersal because ash aggregates have different aerodynamic properties to their constituent ash particles (e.g. Durant et al. 2009).

This can result in premature fallout from the atmosphere (e.g. Sisson 1995; Durant et al. 2009), and changes to the proximal and distal ash mass loadings in the eruption plume. Based on aggregate analysis from recent eruptions together with experimental and numerical studies, a better mechanistic and quantitative understanding of the parameters relevant inside an eruption plume is emerging (Costa et al. 2010; Van Eaton et al. 2012; Del Bello et al. 2015; Mueller et al. 2016). As a result, ash aggregation has been incorporated in ash-plume forecasting models (Folch et al. 2016).

V.2.2 Meteorite impact events

Meteorite impact events produce large dust-rich ejecta clouds (e.g. French and Koeberl 2010). Particle aggregates have been documented in impact deposits on Earth, Mars (Fralick et al. 2012), and Moon (McKay et al. 1970), where they have been used as impact event indicators. On Earth, aggregates have been described in numerous meteorite impact deposits, such as those from the Sudbury (1850±1 Ma; Ontario, Canada; Cannon et al. 2010; Huber and Koeberl 2017), Stac Fada (1199±70 Ma, Scotland; Branney and Brown 2011), Alamo (382±4 Ma; Nevada, USA; Pinto and Warme 2008), Chicxulub (66±0.3 Ma; Gulf of Mexico; Alegret et al. 2005) and Nördlinger Ries (14.94 ± 0.07 Ma; Germany; Graup 1981; Rocholl et al. 2011) impact events.

The basic process of impact cratering is reasonably well-understood (e.g. Melosh 1989; French and Koeberl 2010): upon impact, fragmented target rock is accelerated away from the impact site as an excavation flow, leaving a crater. The accelerated particle flow emerges above the surface, ejects material ballistically and produces an expanding material cone, the ejecta curtain. Most of the material is deposited within a few crater radii, however, a small fraction is ejected significantly further and accordingly deposited at greater distances. Glassy ejecta bombs from the Nördlinger Ries meteorite impact crater, for example, are found 1,000 km away (Gentner et al. 1971; Koeberl 1992, Schwarz et al. 2002). Several models have been proposed to explain impact-related particle aggregates. Johnson and Melosh (2014) suggest that aggregates form within the ejecta curtain. A similar conclusion of aggregation of silicate particles from a cooling ejecta plume was reached for distal (about 1,000 km) aggregates from the Chicxulub impact crater by Yancey and Guillemette (2008). Alternatively, distal aggregates have been attributed to deposits from particulate density currents, physically similar to volcanic pyroclastic density currents (e.g. Addison et al. 2010; Branney and Brown 2011). Grieve et al. (2010) examined the Onaping Formation in the Sudbury crater, which represents fallback material within the crater itself, and concluded that the aggregates formed as a result of melt-fuel coolant interaction (MFCI): water flowed into the crater causing phreatomagmatic eruptions, allowing aggregates to form over several generations, and examples are shown of broken aggregates that have been coated with ash and incorporated into other aggregates. Accretionary lapilli in the Nördlinger Ries impact crater have been attributed to the fallback of

melt-rich impact breccia (which forms the characteristic Suevite upon deposition, Graup 1981) and the gravitational collapse of unlithified suevitic breccias (Stöffler et al. 2013).

V.2.3 Artificial aggregation

Aggregation is a key process in the industrial processing of many powders (e.g. food, feed, pharmaceutical, fertilizer, detergent, and mineral powders). Powders are typically processed under controlled laboratory settings in fluidized beds. For this purpose, gas is fluxed from below through initially stagnant particles. At sufficient flux, particles are lifted and set in a chaotic motion, following stochastic streamlines (Salman et al. 2006). Aggregate formation in fluidized beds can be described in terms of population balance, which describes temporal changes of particle property distributions. Particle size enlargement through aggregation is controlled by operating conditions such as moisture, initial grain-size distribution, processing time, pneumatics and/or thermal conditions (Smith and Nienow 1983; Banks and Aulton 1991; Watano et al. 1996; Iveson et al. 1998; Turton et al. 1999; Uhlemann and Mörl 2000). Under these controlled boundary conditions, the dependence of aggregation efficiency and preservation from the input parameters can be constrained empirically (Mueller et al. 2016).

A structural and textural classification scheme for volcanic ash aggregates has been proposed by Brown et al. (2012), which can also be applied for impact and artificial aggregates. Aggregates are divided into two main categories: particle clusters (PC) and accretionary pellets (AP). Particle clusters can further be sub-classified into ash clusters (PC1) and coated particles (PC2). Accretionary pellets are sub-divided into poorly structured pellets (AP1), pellets with concentric structure (AP2), and liquid pellets (AP3). Based on this classification scheme, we analyze volcanic, impact and artificial aggregates, examine the textural differences and commonalities, and determine the resulting implications for generation mechanisms.

V.3 Methodology

Natural samples were collected during field studies and then transported to the lab, analyzed and classified. Three methods were applied to unravel the inner structure of aggregates: a) cutting and grinding; b) thin section analysis; or c) x-ray computed tomography (CT) of the samples. CT has the advantage of being non-destructive and was used for the rare impact aggregate samples.

The granulometry of artificial aggregates and of several volcanic aggregate samples was determined using a Coulter® LS230 laser diffraction particle size analyzer (Fraunhofer optical model, imaginary / real refractive indices of 0.001 / 1.52 for glass beads and 0.1 / 1.52 for volcanic ash). All artificial aggregate and several volcanic aggregate samples were weak enough to be disintegrated into single particles in an ultra-sonic bath which were then

measured with the LS230. For strongly cemented volcanic aggregate and impact aggregate samples that could not be disintegrated in the ultra-sonic bath, thin section and computed tomography (x-ray CT) based data has been used to evaluate size ranges of single particles using ImageJ software (Schneider et al. 2012).

We apply the aggregate classification scheme of Brown et al. (2012) to volcanic, artificial and impact aggregate samples. We also present special types of aggregates that do not fit in this classification scheme.

V.4 Sample Overview

a) Volcanic ash aggregates

Caldera del Rey tuff ring, Tenerife, Canary Islands

Caldera del Rey is a 1.13 million-year-old (Huertas et al. 2002) phonolitic tuff ring complex (Paradas-Herrero and Fernandez-Santin 1984). Ash aggregates were sampled from a sequence of cm- to dm-thick beds of primarily massive and cross-bedded tuffs that contain occasional pumice lapilli clasts and that show significant lateral thickness variations (Table 1). Ash aggregates are abundant (<10–40 vol%, Brown et al. 2010). Aggregates typically become more abundant and clast-supported towards the top of each bed. No apparent change in aggregate size, structure or abundance could be observed throughout the sampled stratigraphy.

Stromboli volcano, Aeolian Islands, Italy

Ash aggregates were collected from the ~ 5 ka Secche di Lazzaro succession (SDL) at Punta Lena (Giordano et al. 2008), on the SW coast of Stromboli (Table 1). The SDL succession resulted from some northwards directed collapse that allowed seawater to come in contact with magma in the upper part of the plumbing system and triggered a phreatomagmatic eruption. Our samples come from a clast-supported, matrix-free lens of aggregates that sits above the lower SDL unit (UA, see Fig. 7a, Giordano et al. 2008) which consists of aggregate-rich, thinly bedded ash tuffs, deposited from dilute pyroclastic density currents (PDCs). It contains aggregates up to 5 mm in diameter and is interpreted as a fall deposit.

Monte Razzano, Baccano Caldera, Lago di Martignano and Stracciacappa, Sabatini Volcanic District, Italy

The Sabatini Volcanic District (SVD) is part of the potassic Quaternary Roman Province and extends over an area of 1,800 km^2, including the city of Rome (De Rita et al. 1994). Monte Razzano and Baccano Caldera are both part of the Baccano Eruptive Center (BEC) within the SVD. The Baccano pyroclastic succession is dominated by massive to variably laminated ash-

lapilli tuffs with subordinate ash or lapilli fallout horizons (Sottili et al. 2010). Aggregates sampled at Monte Razzano occur in a poorly sorted, matrix-supported ash-lapilli tuff with low aggregate content (Table 1). Aggregates at Baccano Caldera occur within a fine-grained ash tuff with subordinate pumice and lithic lapilli. Lago di Martignano is an 86 ka composite maar located east of Bracciano lake (Sottili et al. 2010). Samples were collected inside the caldera from a poorly-sorted, cross-bedded PDC deposit (Table 1). Stracciacappa is 97 ka hydromagmatic center (maar) north of Lago di Martignano (Sottili et al. 2010). Samples come from laminated and cross-bedded lapilli-tuffs of PDC origin in the northern crater wall (Table 1).

Colli Albani, Italy

The large composite caldera complex of Colli Albani (Alban Hills) is located about 30 km SE of the city of Rome, Italy (De Rita et al. 1995a). Three locations at the foot of the Apennines were chosen for sampling: 1) the Valle Lungherina valley and the villages of Empiglione and Cave (Table 1). At all sites, the sampled deposits were well-sorted massive ash tuffs interpreted as fall deposits from co-PDC plumes (De Rita et al. 1995 a, b).

Solfatara volcano, Campi Flegrei, Italy

Solfatara is a 4.2 ka maar-diatreme volcano cut into older volcanic deposits. Eruptions were dominated by a series of explosions of variable intensity (Di Vito et al. 1999; Isaia et al. 2009, 2015). Aggregates were collected from well-sorted, strongly hydrothermally altered fall deposits exposed in the NNW crater wall.

Soufrière Hills Volcano, Montserrat, West Indies

Aggregates were sampled from the co-PDC fall deposits of the 11 February 2010 eruption (see Stinton et al. 2014; Burns et al. 2017). The sampled deposit consisted of a 10 cm thick layer entirely composed of accretionary pellets. It is underlain and overlain by PDC deposits.

Eifel volcanic field, Germany

The Eifel volcanic field in west Germany is characterized by numerous explosion craters and maars. Aggregates were sampled from the deposits of the Plinian phase of the 12.9 ka Laacher See eruption (Schmincke 2009, Table 1). These deposits are fine- to medium-grained, well-sorted ash beds and were deposited from ash clouds overriding PDCs from Plinian plume collapse (Schmincke 2009). At a separate location 3 km NW of Laacher See, aggregates were found within 150 ka deposits of an eruption at the Wehrer Kessel volcano (Förster and Sirocko 2016). Aggregates were sampled from an ~ 15 cm thick, 3 m long lens composed entirely of ash aggregates.

Tungurahua volcano, Ecuador

Ash aggregates were collected from the deposits of the July-August 2006 eruptions. The August eruptions generated PDCs that flowed down the NW- and W-flank of the volcano (Douillet et al. 2013). Aggregates were observed in a fines-depleted lapilli tuff at the top of a several meter-thick deposit located where PDCs deposits had temporarily dammed the river (Kueppers et al. 2016).

Santo Antão, Cape Verde

Aggregates were sampled on the island of Santo Antão, Cape Verde, which was dominated by two partly co-existing magmatic series of mafic shield-building phases until about 100 ka ago (Holm et al. 2006). Towards the end of the shield-building phase, highly explosive eruptions emplaced the Cão Grande Formation. Aggregates were sampled in the uppermost part of the dry river bed of the Ribeira do Canudo on the western plateau of Santo Antão. They occur in a single horizon intercalated with tephra-phonolitic PDC deposits from the initial phase of the Cão Grande 2 eruption, which overlies the phonolitic Cão Grande 1 pumice fall deposit.

Masaya Caldera, Nicaragua

Aggregates were sampled from an ~34 ka ignimbrite (Bice 1985) in a quarry at Canteras, about 7 km WSW of Diriamba. The scoria-rich ignimbrite belongs to the upper part of the Pleistocene Las Sierras Formation which was erupted from a caldera adjacent to Masaya Caldera (Freundt et al. 2010). The ignimbrite is composed of three depositional units 1–3 (Freundt et al. 2010). Units 1 and 2 likely to represent the same eruption, while unit 3 followed after a significant time interval of several years. Aggregates occur in Units 1 and 3, in both fall and PDC deposits.

b) Impact Aggregates

Nördlinger Ries impact crater, Germany

The 15 Ma old, 25 km diameter Nördlinger Ries impact crater (Rocholl et al. 2011; Stöffler et al. 2013) was created by the impact of a 1.1–1.5 km diameter asteroid (Artemieva et al. 2013). The target stratigraphy comprised 600-700 m of Triassic and Jurassic sedimentary rocks overlying crystalline basement (Pohl et al. 1977; Hüttner and Schmidt-Kaler 1999; Stöffler et al. 2002). The crater volume estimates range between 124 km^3 and 200 km^3 (Pohl et al. 1977; Hörz et al. 1983; von Engelhardt and Graup 1984). Immediately after impact, a primary ejecta curtain started emplacing primary suevite—a widespread layer of massive, very poorly sorted, clast- to matrix-supported fallback sediments with abundant clasts of molten ejecta—directly on top of parautochthounous (as uplifted) crystalline basement (Artemieva

et al. 2013; Stöffler et al. 2013). Later ejecta deposits in and outside the crater are finer-grained and lack melt clasts (Graup 1981). Thirteen boreholes have been drilled inside the morphologic crater; ten of which penetrated the suevite and reached the underlying crystalline basement (Stöffler et al. 2013). Accretionary lapilli occur in suevite units in three boreholes. Samples in this study come from the Nördlingen 1973 drillhole (FBN 73) at depths of 296 m and 301 m. In all three cases, the aggregates are found only in the transition zone between post-eruptive lake sediments and underlying suevite, where they are sparsely distributed within fine grained (< mm) layers. This has been interpreted as fallout from the uppermost part of the primary ejecta curtain, rich in solid particles and water vapor. Aggregates in the Deiningen and the 1001 drillholes have been described elsewhere (Mosebach 1964; Förstner 1967; Graup 1981).

Sudbury impact structure, Canada

Sampled Sudbury aggregates derive from the Connors Creek location (see Huber et al. 2014). The deposit comprises ~1 m of lithic (chert) breccia, overlain by ~1 m of breccia that also contains melt glass and accretionary lapilli. Cannon et al. (2010) include an overlying ~5 m thick layer that grades from brecciated material at the base to finer material near the top, but note that the accretionary lapilli are found in beds that are cross-bedded, with thin bands of fine-grained breccia between the beds, which may be evidence of reworking.

c) Artificial aggregates

Glatt Ingenieurtechnik GmbH, Weimar, Germany

Artificial aggregates used in this study were produced via fluidized bed techniques at Glatt Ingenieurtechnik GmbH, Weimar, Germany, from soda-lime glass beads (<50µm, 40–70µm, <70µm) and natural volcanic ash (<40µm, 40–90µm, <90µm) collected from deposits of the Laacher See eruption (Germany). Grain size data is provided in the Supplementary Dataset. Mueller et al. (2016) produced both particle clusters (PC) and accretionary pellets (AP) under controlled and reproducible conditions. The following parameters were varied during the experiments to examine their influence on aggregation: 1) initial particle size distribution, 2) humidity, 3) viscosity of the liquid binder, 4) Reynolds numbers of the fluidized particles, 5) gas velocity, 6) salt concentration on the particle surfaces, 7) temperature, and 8) processing time. Aggregates were produced through spraying either a NaCl-bearing solution of H_2O or a 37% HCl solution. In both cases, the liquid phase induces aggregation following collisions and the resultant salts cement the particles together after evaporation of the liquid. Salts (mainly NaCl) are either generated through re-crystallization upon H_2O evaporation, or through chemical reactions between the HCl phase and the glass (Mueller et al. 2017b). The

aggregates produced in this manner are between 0.5–5 mm in size, depending on experimental parameters (Mueller et al., 2016).

Sample location	Age	Stratigr. unit	distance to vent [m]	**(PC1)**	**(PC2)**	**(AP1)**	**(AP2)**
Baccano Caldera, Sabatini Volcanic District	90 ka	fallout	100	x			
Caldera del Rey, Tenerife	1.13 Ma	PDC	100		x		x
Cave, Colli Albani	600 ka	PDC	18,000			x	x
Dachsbusch, Eifel	12.9 ka	fallout	2,000	x			
Empiglione, Colli Albani	600 ka	PDC	25,000			x	x
Lago di Martigniano, Sabatini Volcanic District	90 ka	PDC	50	x		x	x
Masaya Caldera, Nicaragua	33.8 ka	fallout & PDC	23,600			x	x
Monte Razzano, Sabatini Volcanic District	90 ka	fallout	1,600	x	x		
Montserrat, Soufrière Hills	2010 AD	fallout	5,400			x	x
Nickenich, Eifel	12.9 ka	co-PDC fallout	5,000	x	x	x	
Santo Antão, Cap Verde	100 ka	PDC	5,300	x			
Secche di Lazzaro, Stromboli, Italy	5-13 ka	fallout	2,000	x	x	x	x
Solfatara, Campi Flegrei	6.2 ka	fallout	100	x		x	
Stracciacappa, Sabatini Volcanic District	90 ka	PDC	300	x		x	x
Tungurahua, Ecuador	2006 AD	PDC	4,500		X	x	x
Valle Lungherina, Colli Albani	600 ka	PDC	20,000			x	x

Table V.1: Overview of investigated aggregates, their stratigraphic unit and structural type. Tenerife, Spain; Stromboli, Italy; Sabatini Volcanic District, Italy (Monte Razzano, Baccano Caldera, Lago di Martignano, Stracciacappa); Colli Albani, Italy (Valle Lungherina, Empiglione, Cave); Solfatara, Italy; Soufrière Hills Volcano, Montserrat; Eifel volcanic field, Germany (Laacher See, Dachsbusch); Tungurahua, Ecuador; Santo Antão, Cape Verde and Masaya Caldera, Nicaragua (Huertas et al., 2002; Giordano et al., 2008; Sottili et al., 2010; De Rita et al., 1995 a & b; Isaia et al., 2009; Stinton et al., 2014; Schmincke, 2013; Douillet et al., 2013; Holm et al., 2006; Freundt et al., 2010).

V.4.1 Results: Structural Analysis

a) Volcanic ash aggregates

Samples analyzed in this study represent mainly PC and AP aggregate types (plus all subcategories except mud drops, AP3). In total, more than 1,100 volcanic aggregates were analyzed. Aggregate sizes range from 1 mm (e.g. Secche di Lazzaro, SDL) to 2 cm in diameter (e.g. Valle Lungherina, Figure V.1). In this study, aggregates from the same sample location

generally exhibit restricted size ranges (Fig. V.1); this contrasts with other studies where a wide range of aggregate sizes exist at a single location (e.g., Wallace et al. 2013).

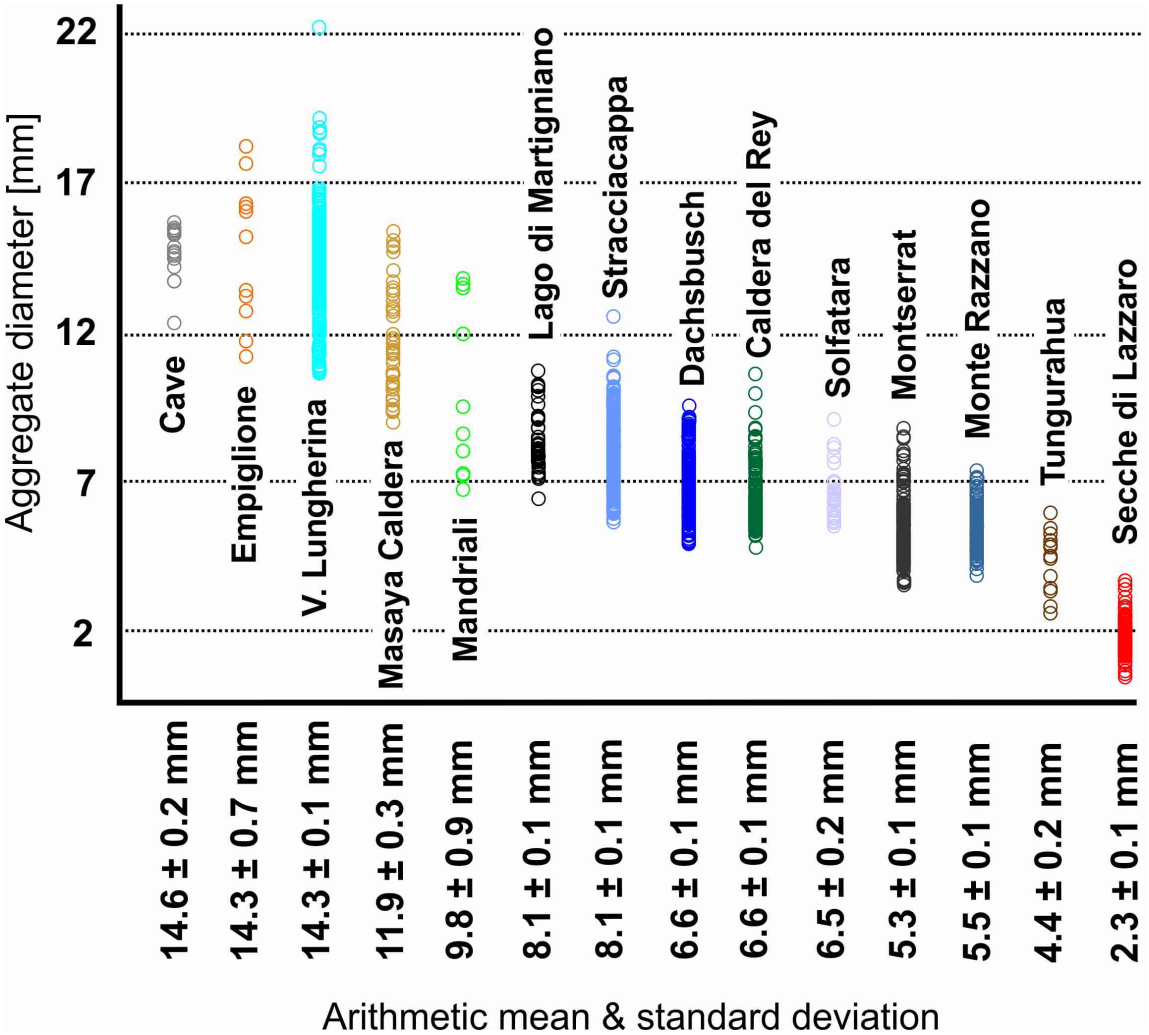

Figure V.1: Size ranges of more than 1100 sampled volcanic aggregates. Mean size (diameter) and standard deviation are shown. Size ranges of aggregates are clearly confined to several mm.

Diverse types of aggregates were found very close to each other, sometimes within the same stratigraphic unit. For example, in the SDL succession on Stromboli (Table V.1), a single drill core (2.5 cm diameter, 5 cm long), analyzed by x-ray CT, revealed lithic fragments coated with thick ash layers resembling to some extent PC2 type aggregates, poorly structured pellets (AP1), and pellets with concentric structure (AP2, Fig. V.2a). Mixed populations of aggregates were also found at Caldera del Rey (see also Table V.1).

Besides aggregates that fall into the PC/AP classification of Brown et al. (2012), we also sampled aggregates that can be described as coated accretionary pellets: a hybrid between PC2 and AP2 type aggregates. These aggregates are spherical, cm-sized pellets with concentric rim structures, exhibiting cores composed of either broken fragments of other aggregates (e.g. the rims fragments in the samples from Empiglione, Fig. V.2b) or lithic fragments (aggregates at Masaya Caldera, Fig. V.2c). Other samples can be described as double featured, i.e., accretionary pellets that have a second accretionary pellet as a core (Fig. V.2d).

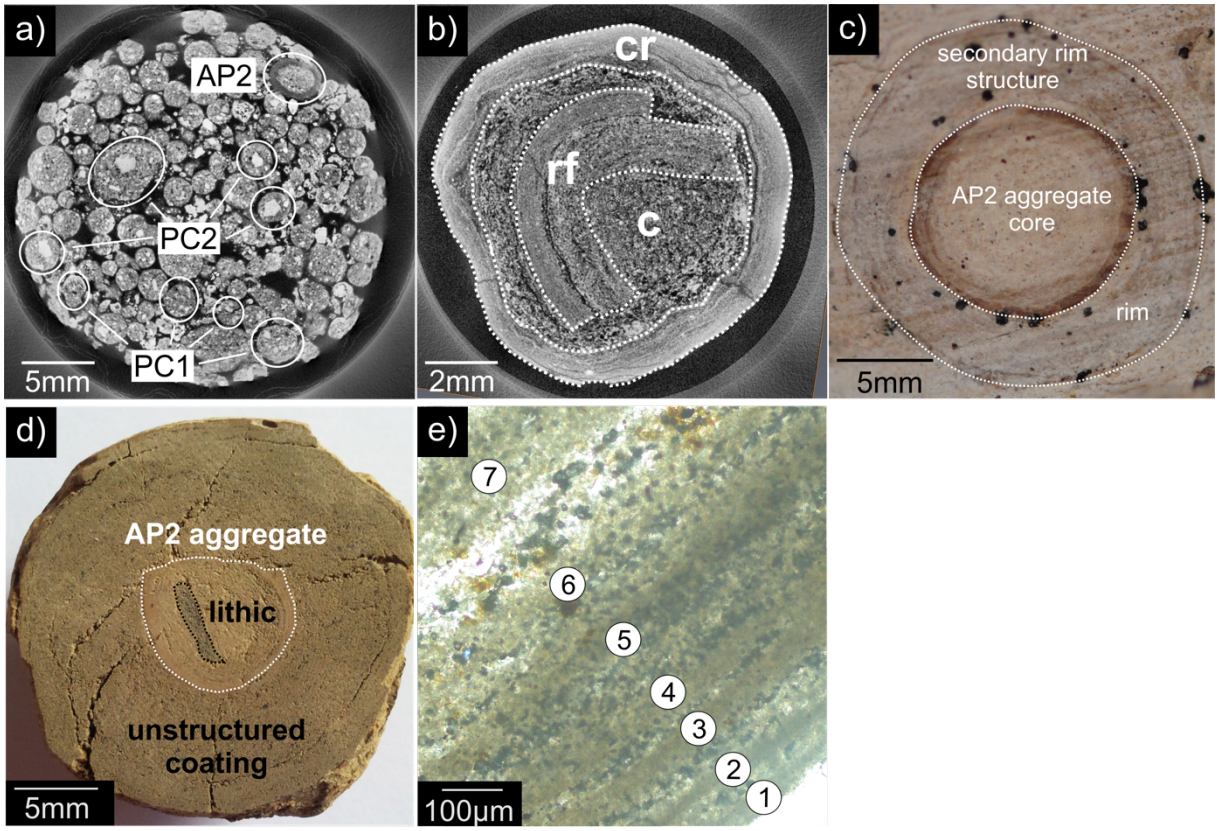

Figure V.2: Details of various samples at various resolutions. a) X-ray CT analysis of a 2.5 cm wide drill core from the Secche di Lazzaro succession on Stromboli. The drill core contains PC1, PC2 and AP2 type aggregates. Most aggregates represent the PC1 type. b) AP2 similar type aggregate from Empiglione, Italy, 10mm across. The x-ray image shows a broken rim fragment (rf) being recycled to act as a core (c) of a new accretionary pellet coated by a concentric rim structure (cr). c) sample from Caldera del Rey, Tenerife, showing a 'double' accretionary pellet: a small, inner accretionary pellet acts as a core for an even larger accretionary pellet. Concentric structures typical for APs are existent in both the inner and the outer rim structures. The whole structure is 20mm across. The dotted lines indicate the physical and optical separation of the inner accretionary lapilli from the outer rim. d) Accretionary pellet sample from Masaya Caldera, Nicaragua. The inner, spherical accretionary pellet (AP2) has a black lithic fragment acting as a core ("armored pellet"). Compared to the Caldera del Rey sample (Fig. 2c) there are no concentric rim features in the outer part of the sample existing. e) Close-up of the rim of an AP2 sample of Valle Lungherina, exhibiting the repetitive formation of rims with a grain size fining outwards.

Rarely, accretionary pellets show an accumulation of several thin (10s of µm), concentric rims around a central core, such as in the Valle Lungherina sample (VL) where up to seven distinct rims are present (Fig. V.2e).

To quantitatively compare the structure of volcanic aggregates, core and rim diameters of > 100 AP type aggregates were measured with a digital caliper (Fig. V.3). Core and rim diameters (see also Fig. V.2b for measurement procedures) average 6.0 ± 0.5 mm and 1.32 ± 0.1 mm, respectively, with a mean core to rim ratio for volcanic aggregate samples of 4.54 ± 0.13 (Fig. V3). For comparison, we plot data from Van Eaton and Wilson (2013) from the 25.4 ka Oruanui eruption of Taupo volcano, New Zealand. Some of these samples show very thick rims compared to their cores, but the overall core to rim ratio is smaller (average at 3.41) compared to our volcanic samples. This seems to indicate a slightly different aggregation pattern, allowing the rims to grow for a longer period or at very efficient rates.

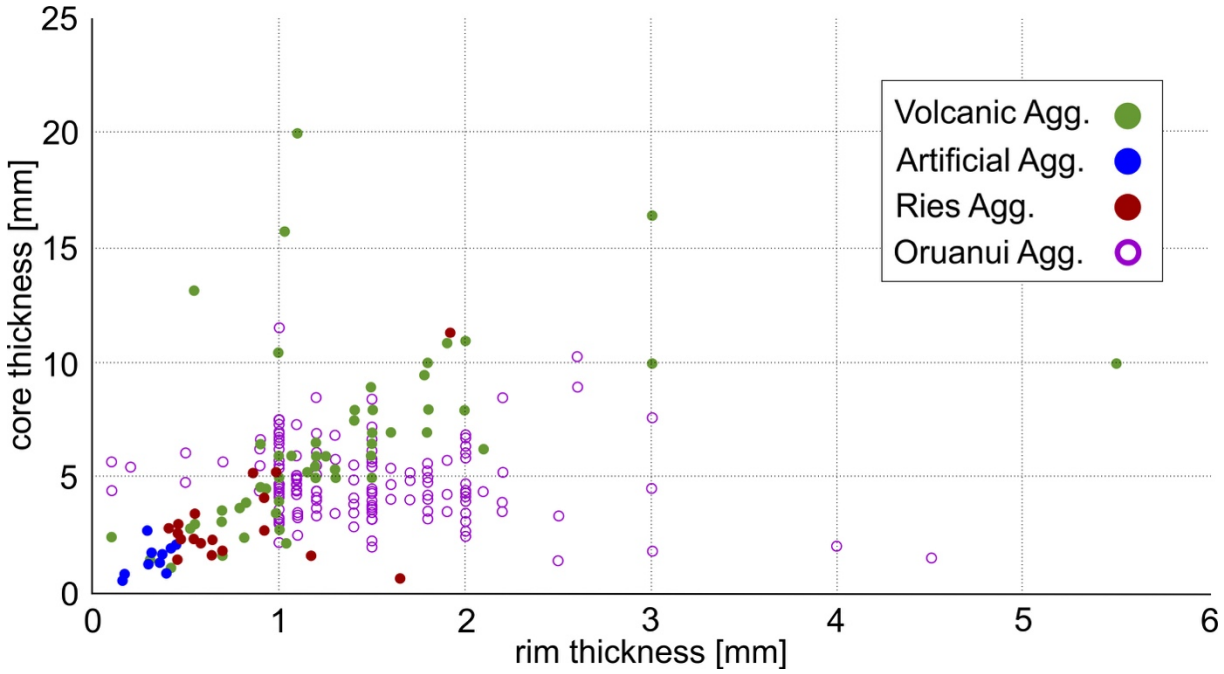

Figure V.3: Measured core vs. rim thicknesses for volcanic, artificial and Noerdlinger Ries samples. Additional data for comparison from Van Eaton and Wilson (2013) for aggregates from the 25.4 kya Oruanui eruption from Taupo volcano, New Zealand, have been added and show good agreement with our data. Some Ries and Oruanui samples show clearly increased rim thicknesses compared to the average data plot.

The structural characteristics show that aggregation is a complex process that may see several phases of aggregation and aggregate breakup (Mueller et al. 2017a). Aggregation may initiate around larger clasts (coated lapilli, Fig. V.2b, d) or through the growth of ash pellets (Fig. V.2a, c) with variable grain size and sorting. Certain processes may allow aggregates to become mechanically strong (by, for example, cementation through the precipitation of

secondary mineral phases and possibly also by freezing). Fragments of such hard aggregates can form sites for new aggregates (Fig. V.2b).

b) Meteorite Impact Aggregates

The 19 analyzed samples from drill cores from the Nördlinger Ries impact crater consist exclusively of AP1 and AP2 aggregates. Aggregates range in size from 2–10 mm and have spherical shapes. In contrast to the volcanic ash aggregates, some of the impact aggregates have very irregular, wavy rim structures (Fig. V.4a). The mean core and rim thicknesses are 3.2 ± 0.5 mm and 0.78 ± 0.1 mm, respectively, and their mean core to rim ratio of 4.1 ± 0.21) is generally comparable with volcanic samples. However, some aggregates have rim diameters that exceed the core diameters and show similarities with the Oruanui data (Fig. V.3, V.4b, c).

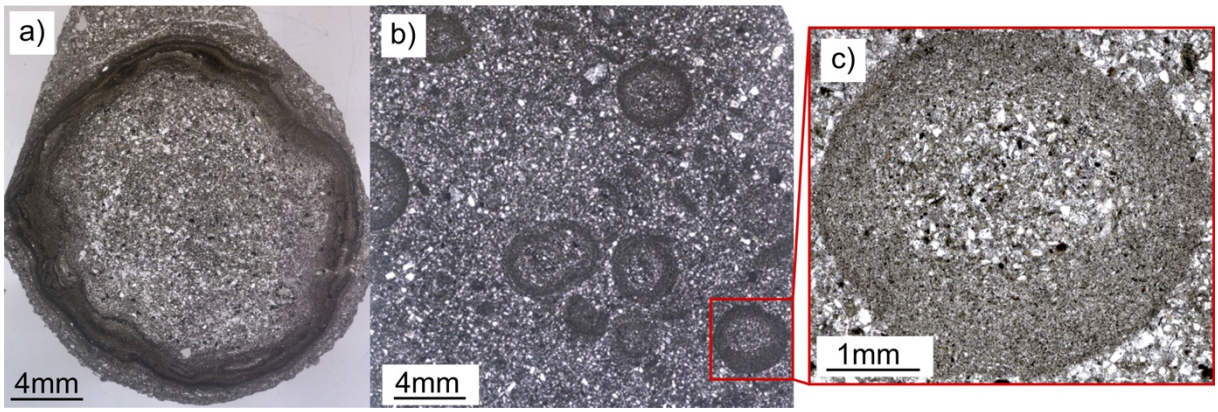

Figure V.4: a) Accretionary pellet sample from the Nördlingen 1973 drill hole (FBN 73) inside the Nördlinger Ries, Germany, from a depth of 296 m. Sample shows a clear separation into core (approx. 80% of the volume) and rim based on PSD. The overall shape of the pellet is spherical, but a wavy pattern of variably thick "growth rims" can be observed. b) shows a thin section also of the FBN 73 drill hole and a depth of 309.5 m. Matrix supported accretionary pellets are spherical in their shape and show rims with thicknesses equalizing the according core thickness (c).

Aggregates from the Sudbury impact deposits (Fig. V.5a) consist of individual accretionary lapilli that are up to 2 cm in diameter. In cross-section, the lapilli exhibit multiple concentric rims. The lapillus imaged in Fig. V.5b has a core of 4.5 mm diameter and an inner rim of 2.0 mm; the outer rim, present only around half of the lapillus, is 2.8 mm in diameter. The lapillus in Fig. V.5c has a core of 4.0 mm, an inner rim of 2.6 mm, and an outer rim of 2.0 mm.

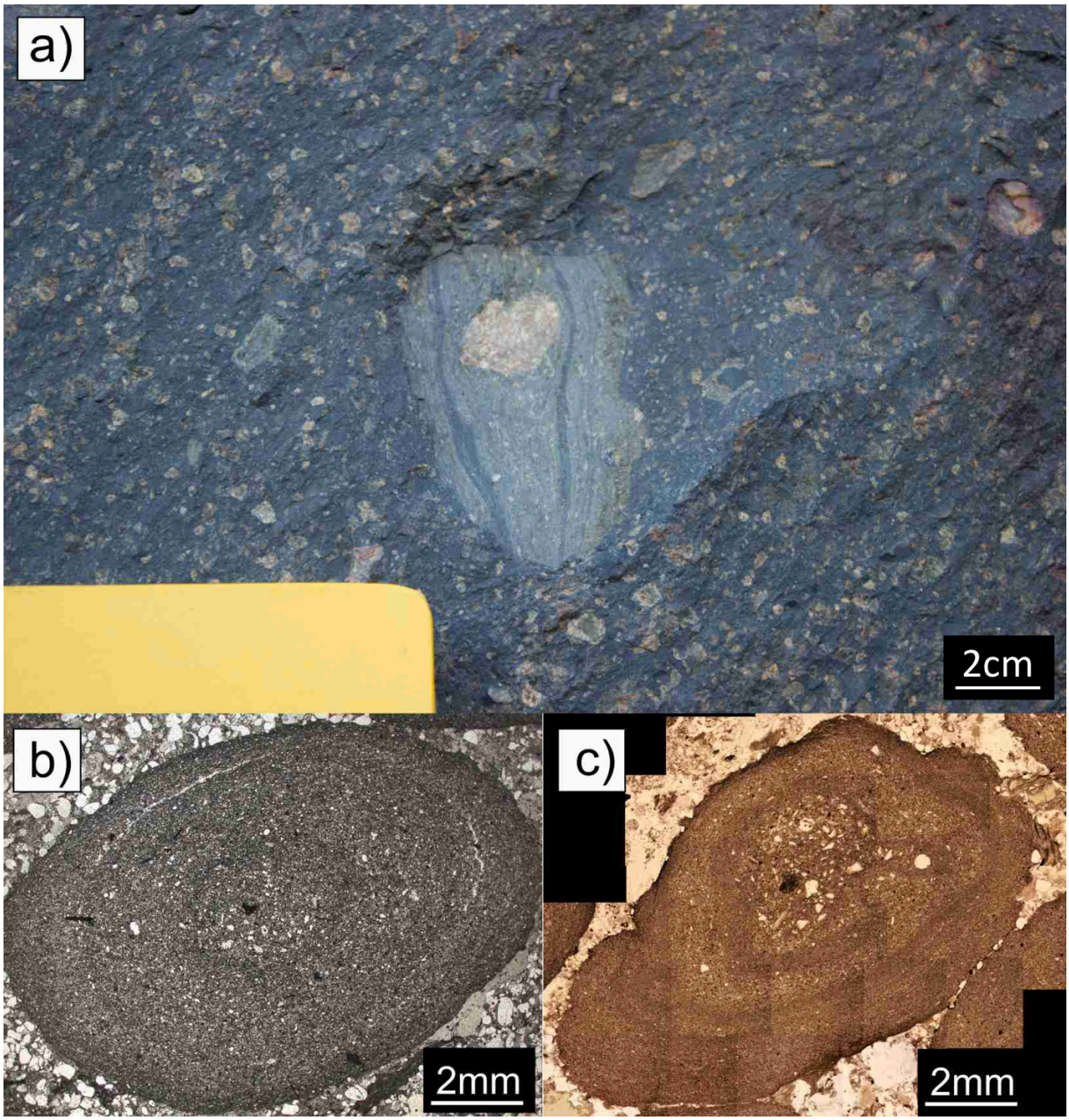

Figure V.5: Accretionary features from Sudbury impact structure, Canada. a) Lithic breccia (Onaping formation) containing accretionary lapilli in cross-bedded beds, intersected with fine-grained breccia. b) & c) Accretionary lapilli collected at Connors Creek site, some 450-500 km from the impact location. Lapilli consistently show coarse grained cores and finer grained rims, sometimes several concentric ones. The lapilli show different states of preservation, indicating variable degrees of shape alteration by mechanical erosion.

a) Artificial Aggregates

Structures of artificial aggregates are described briefly here; for a more detailed analysis see Mueller et al. (2016). With the ProCell Lab®, we were able to reproduce both PC and AP aggregates. Depending on the initial particle size distribution (PSD), the resulting

aggregates were either: a) non-spherical and structureless (PC1), b) spherical and structureless (AP1) or c) spherical and internally structured (AP2). PC1 aggregates were produced with highly confined starting PSDs (< 40 µm or 40–90 µm particles only), AP1 aggregates appeared under the use of broader starting PSDs (i.e. < 90 µm particles), and fully evolved AP2 aggregates were generated at starting PSDs of <300 µm particles. Artificial aggregates are generally smaller than volcanic aggregates and exhibit diameters ranging between several 100 µm and a few mm, and have modes between 1–2 mm (depending on experimental conditions). The largest artificial aggregate diameters (5 mm) were achieved through the use of high viscosity binders (37% HCl) that sometimes allowed two or three APs to connect with each other and form aggregate clusters with diameters up to 1 cm. Mean core and rim thicknesses are 1.40 ± 0.20 mm and 0.33 ± 0.03 mm, respectively. Despite their small size, artificial aggregates show a similar core to rim ratio (4.24 ± 0.28, see Fig. 3) to the volcanic ash aggregates.

V.4.2 Results: Textural Analysis

a) Volcanic ash aggregates

Grain size analysis by laser diffraction (Coulter® LS230) requires particles suspended in water. Samples from seven different locations (Valle Lungherina, Cave, Monte Razzano, Stracciacappa, Montserrat, Tungurahua, and Laacher See) could be disintegrated with minimal mechanical force. We determined the PSDs of up to 10 aggregates from each location (Fig. V.6). Samples show a typical particle size range of < 200 µm with their modes around 100 µm for Eifel, Stracciacappa, Monte Razzano, and Valle Lungherina, and 20–50 µm for Tungurahua, Montserrat and Cave. Maximum particle sizes in the volcanic aggregate samples were ~200 µm. X-ray CT and thin section analyses of samples that could not be disaggregated revealed much coarser-grained volcanic aggregates: for example, PC1 samples from Santo Antão contain clasts of up to several mm in diameter (Fig. V.7a). AP2 samples from Tenerife contain 500 µm diameter particles in their cores (Fig. V.7b).

We sampled the surrounding unconsolidated matrix for aggregates extracted from PDC deposits. PDC deposits were matrix-supported, and maximum grain sizes of the matrix exceeded the maximum clast size of aggregates significantly (up to ten times, e.g. Tenerife, Fig. V.7b). Aggregate rims were much finer in grain size than matrix material, e.g. Fig. V.7b). Matrix material of six of the seven previously named sample locations has been sieved at 250 µm (~ 50–80 wt% of total deposit materials < 255µm), which conforms to the maximum grain size generally observed in aggregates. All matrix materials except for Monte Razzano and Valle

Lungherina, have coarser grained modes than their respective aggregates; all six sample locations reveal an enrichment of fine material (<40–80 µm) in aggregate material compared to matrix material (Fig. V.6).

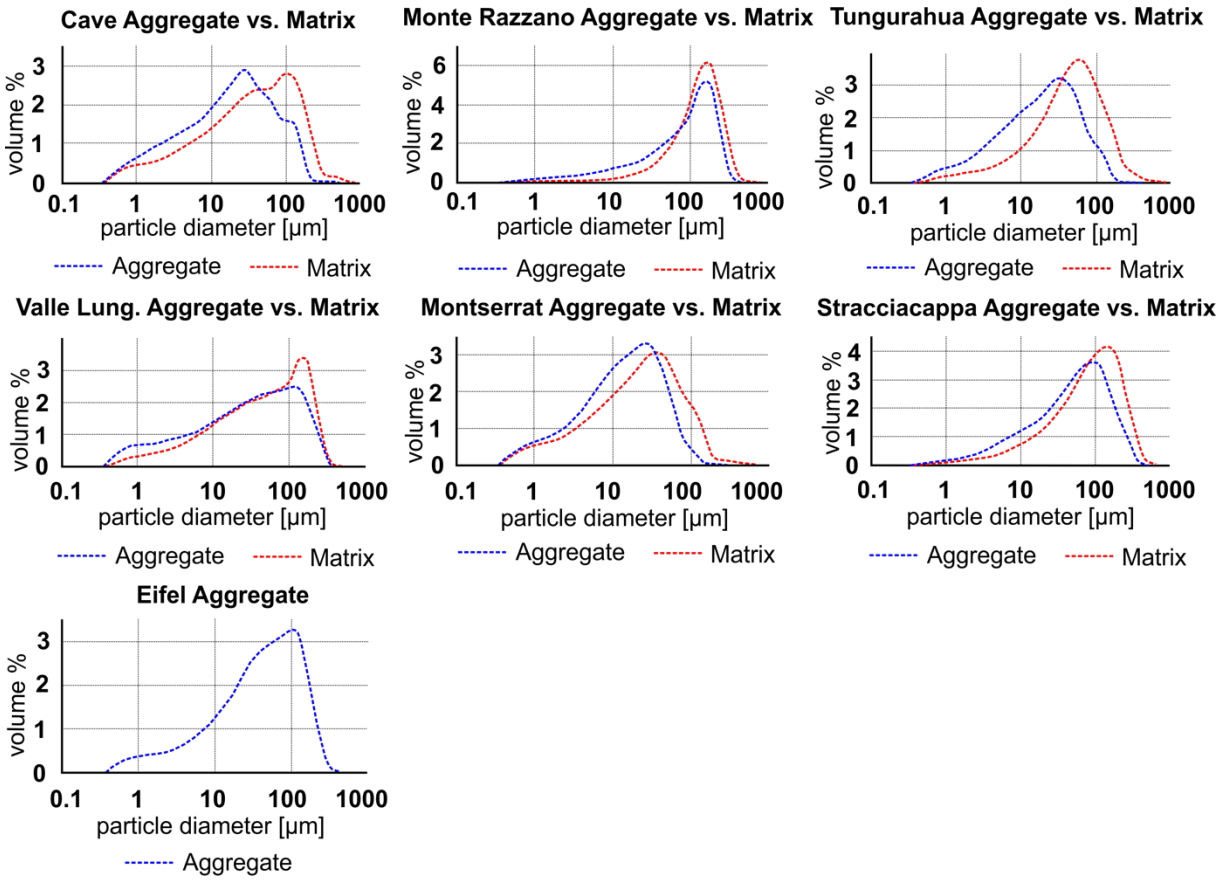

Figure V.6: Particle size distribution (PSD) of aggregates vs. the surrounding matrix. PSD of aggregates (core and rim together) is systematically finer grained (modes between 20 µm (e.g. Cave) and 120 µm (e.g. Razzano)) compared to the surrounding matrix. For comparison, PSD of matrix < 250 µm only is shown.

For five locations (Valle Lungherina, Stracciacappa, Monte Razzano, Cave, and Eifel) it was possible to separate the rims from the cores of AP2 samples and measure them by laser diffraction (Fig. V.8). All samples showed finer grained modes for their rim PSDs (40–100 µm) than for their core PSDs (110–140 µm): rims are enriched in fine material (< 60 µm) and cores are enriched in coarse material (> 60 µm).

b) Meteorite Impact Aggregates

It was not possible to analyze impact aggregates with the Coulter® LS230, because the aggregates are entirely lithified. Also, the spatial resolution of the x-ray CT was not sufficient to compute the PSD with Avizo, a software used to analyze CT data. Instead, ImageJ was used to estimate both the upper size range and average PSD of clasts building up the aggregates,

based on thin sections and x-ray CT data. Particle size distributions smaller than approximately 100 µm were impossible to determine due to strong alteration of aggregate samples. Figure V.9a shows an x-ray CT image of an AP2 type sample (found at a depth of 296 m) embedded in matrix. The sample is about 1.1 cm in diameter and has a PSD < 150 µm in its core and < 85 µm in its rim. The PSD mode is at about 100–130 µm for the core and 30–50 µm for the rim. Other analyzed aggregates, especially from the thin section shown in Figure V.9b, confirm these findings: the cores have a much coarser-grained peak in PSD than the rims.

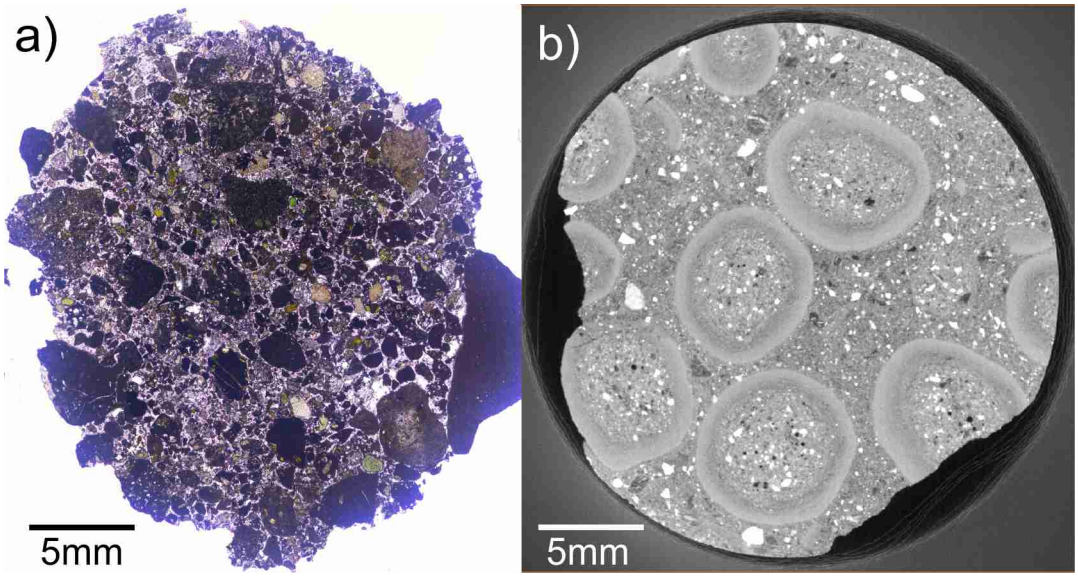

Figure V.7: Examples of aggregates containing abundant coarse clasts. a) Cape Verde particle cluster (PC) with primary particle sizes of up to several mm. b) Drill core from Caldera del Rey, Tenerife, analyzed with X-ray CT. AP2 type aggregates are embedded in matrix material. AP2 aggregates have coarse grained cores and fine grained rims, PSD of aggregates does not exceed maxima of 500 µm. Matrix material lacks fine grained ash as it is bound in the rims of the aggregates and PSD does not exceed maxima of 1.5 mm.

c) Artificial Aggregates

Halite-cemented artificial aggregate samples were disintegrated in water and their PSDs measured with the Coulter® LS230. We analyzed 30 Laacher See ash aggregates that were generated with a fluidized bed of a PSD <90 µm. These 30 measurements were averaged and compared to the mean PSD of the raw material (Fig. V.10). Aggregates and raw material share the same mode in their PSDs at 70 µm. However, the aggregates show a clear enrichment (approx. 10 vol %) of fine particles (< 50 µm) compared to the raw material. Artificial aggregation was not limited to materials < 90 µm. By increasing aggregation efficiency through the use of higher viscosity binders such as HCl (relative to H_2O), we were able to generate AP2 aggregates out of a starting sample batch containing clasts as large as 500 µm. Because of the involved forces, aggregation is a size-selective process and large particles will be enriched in the cores (Fig. V.11, Mueller et al. 2016).

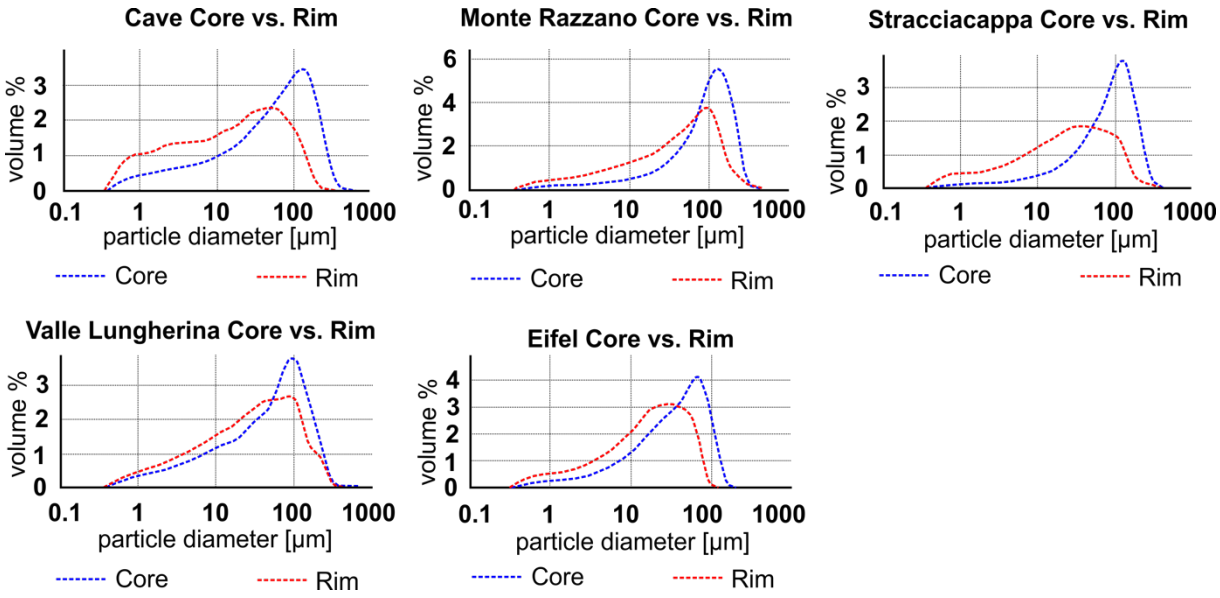

Figure V.8: Particle size distribution (PSD) within aggregates: PSD of cores and rims has been measured and compared to each other: all cores show a coarser grained mode in PSD and have less fine material (< 60 µm) than the rims.

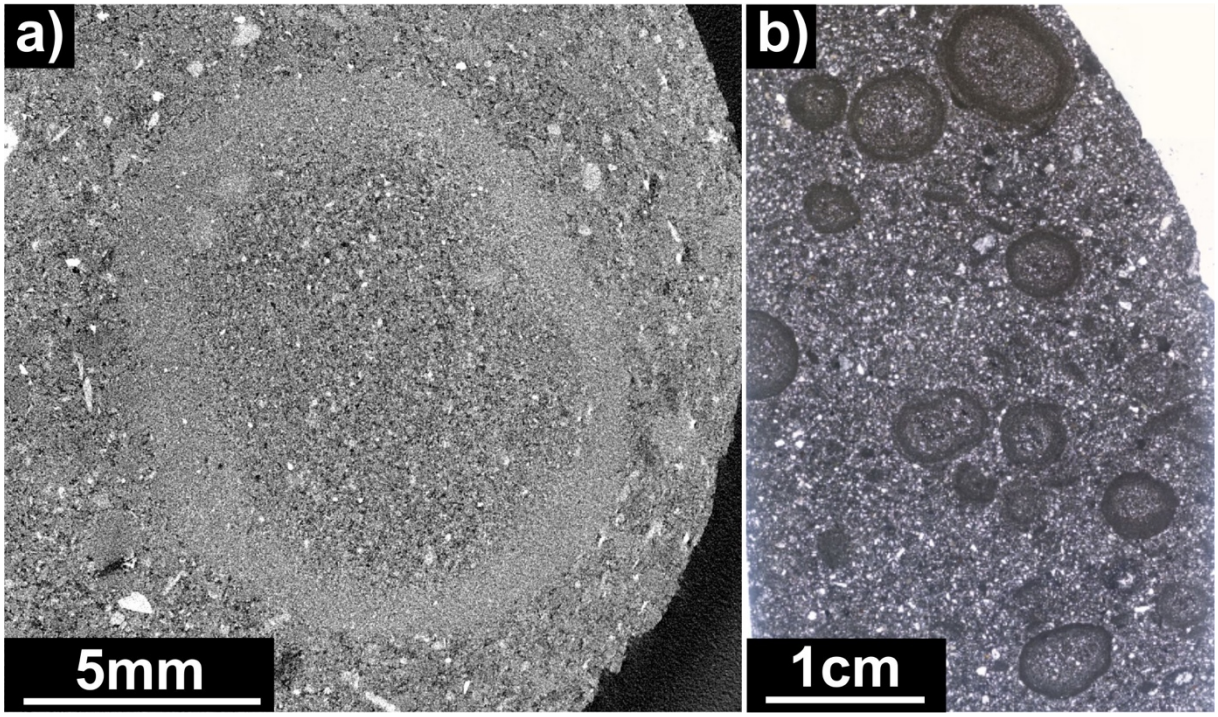

Figure V.9: a) X-ray CT image of an AP2 type sample from the FBN73 drill core inside the Nördlinger Ries, Germany, sampled at a depth of 296 m (see also Stöffler et al., 2013). The aggregate is about 1.1 cm in diameter and has an overall PSD < 150 µm with a clearly finer PSD of about < 85 µm in the rim. b) Accumulation of AP2 type aggregates, also from the FBN73 drill core but sampled at a depth of 313 m. Aggregates are between 0.5 and 1 cm in size and show clear coarse grained core and fine grained rim features.

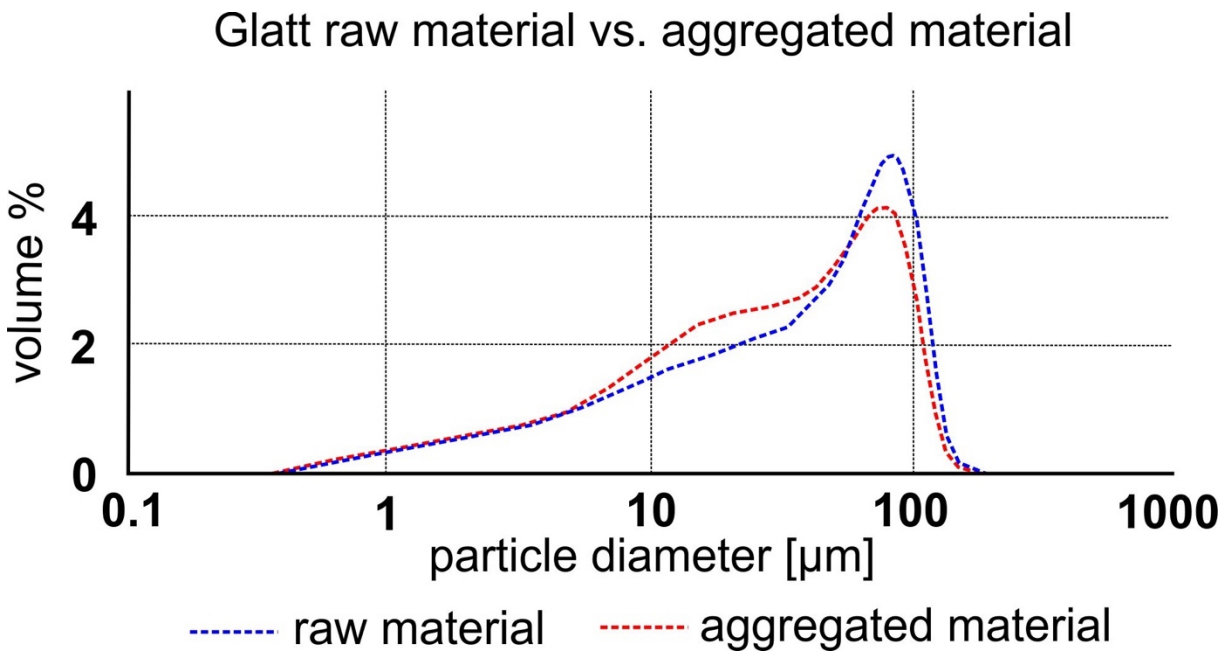

Figure V.10: PSD of artificial aggregates produced with starting materials of nominally <90 µm size. Enrichment of fines in aggregates, particularly between 5 and 60 µm, is visible. The aggregate dataset has been achieved by averaging more than 100 artificial aggregates.

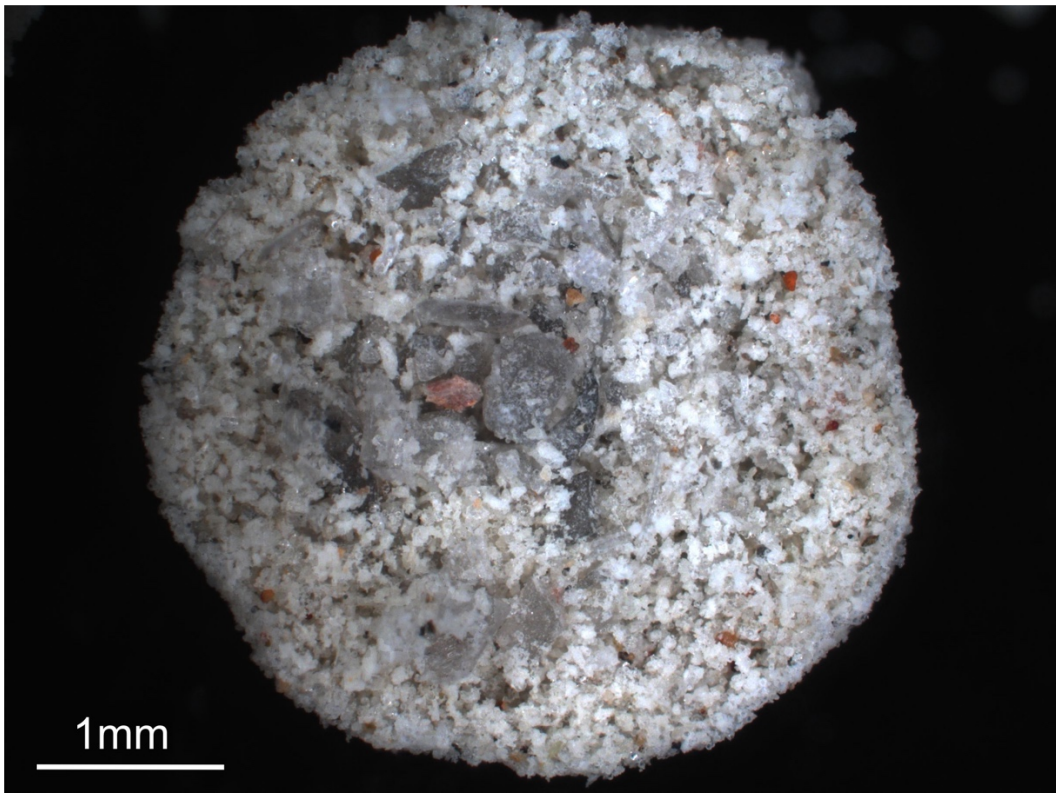

Figure 11: Artificial ash aggregate (AP2) produced of an initial PSD < 500 µm. Particles of several 100s of µm are centered in the core region of the aggregate, the rim is built out of finer material. The aggregates show a heterogeneous distribution of particle packing of residual inter-clast pore space.

V.5 Interpretation

V.5.1 Particle binding mechanisms

Large aggregates as described in this study are primarily generated through hydrostatic bonding forces and subsequent cementation. Several samples in this study derive from dry eruptions (e.g. Tungurahua, Montserrat). Accordingly, the presence of accretionary lapilli in general, in pyroclastic deposits should not be taken as a proxy for explosive eruptions involving external water at the fragmentation level (i.e. phreatomagmatic or Surtseyan). The geographic distribution of aggregate appearance in PDC deposits points to the strong influence of the ambient conditions. A free water phase (whether in the liquid or gaseous state) is omnipresent in volcanic eruption plumes, meteorite ejecta plumes or ash clouds overriding PDCs. This water has several possible origins: magmatic origin (H_2O is the most abundant volatile species dissolved in silicate melts, e.g. Mader 1998), external water from aquifers or surface water bodies (e.g. Edmonds and Herd 2005) or entrainment of ambient humidity from tropospheric air (e.g. Tomita 1985). When hot PDCs travel across water bodies significant volumes of steam can be added to the background humidity. In ash-rich environments, this may enable and/or enhance aggregation. Several of the investigated aggregates derive from deposits that show indications of such interactions as, for example, with a river (e.g. Tungurahua 2006), lake (e.g. Sabatini Volcanic District) or ocean (e.g. Soufrière Hills Volcano, Montserrat 2010). Tomita et al. (1983) observed wet aggregates falling from the H_2O-rich eruption plume of Sakurajima volcano, Japan and described high relative air humidity values of 85%.

Artificial aggregation experiments have shown that increasing the humidity in a particle-laden environment exponentially increases the aggregation rate (Mueller et al. 2016). Volcanic eruption plumes and impact ejecta curtains can entrain external humidity from the atmosphere or from, for example, the impactor target region (groundwater, lake, ocean, etc.) or the atmosphere. As particle aggregates bound by electrostatic forces have average diameters no larger than several tens of µm (James et al. 2002), we postulate that the generation mechanism of the cm-sized Nördlinger Ries aggregates involved hydrostatic bonding forces, coupled with subsequent cementation processes to stabilize them. Due to their age, and alteration, it is not possible to analyze potential chemical binders within impact aggregates.

V.5.2 Aggregate growth processes

The growth of aggregates is limited by physical forces: experiments have shown that aggregates will continue to grow for as long as the impact energies of colliding particles can be dissipated by the viscous forces of the liquid binding agent (Ennis et al. 1991). At a certain aggregate size, impact energies exceed the viscous dissipation forces of the liquid binder and

causes the impacting particles to rebound. This halts aggregate growth (Mueller et al. 2016). This may explain the observation that aggregate populations are relatively homogeneous in size (Fig. V.1). If critical aggregation parameters such as liquid binder viscosity and, as a consequence, liquid film thickness, PSD, humidity, or temperature do not change drastically, aggregates will stop growing once they have reached a certain size (Ennis et al. 1991; Mueller et al. 2016). Another important factor is the residence time within an environment conducive to aggregation. As long as growing aggregates are falling through an ash-contaminated atmosphere, or are kept in (quasi-) suspension in or above a PDC, aggregation will continue and allow thick rims to grow (e.g. Fig. V.2c), or allow aggregate size to vary as a function of distance from the volcano. The largest aggregates are sometimes found at some distance from the vent (see Wallace et al., 2013, and Van Eaton et al. 2015, for observations from deposits of the Redoubt event 5 in 2009, Alaska). Finally, large aggregates are, with their increased mass, subject to greater impact energies which makes them prone to shattering and disaggregation (e.g. Mueller et al. 2017a). This may explain the rare occurrence of exceptionally large aggregates with diameters up to several 100% larger than the surrounding mean of aggregate diameters, both in impact and volcanic sediments.

Whether one thick rim or multiple thin rims grow around an aggregate will depend strongly on the environmental conditions and the residence time within the atmosphere. If aggregation conditions change slowly (in favor of aggregation increasing, for example, humidity or binder viscosity), a single rim could keep growing for an extended period of time. Conversely, multiple rims, and significant variation in the size of the aggregated grains, must reflect drastic changes in aggregation conditions, probably primarily controlled by the relative velocity of an aggregate and the ambient ash cloud. This may result in a change in the PSD of aggregating particles and would manifest as a second rim structure. For example, one of the aggregates from the Caldera del Rey tuff ring (Figure V.2c) shows a distinct boundary between two lithologically distinct rims, indicating the strongly changed conditions for aggregation.

We speculate that impact-related aggregates may be suspended for longer time periods within atmospheric dust clouds than, for example, volcanic aggregates. This may be due to the potentially higher initial altitudes attained by impact ejecta curtains and this might contribute to the thicker rims on impact-generated aggregates.

V.5.3 Synthesis of aggregate structures and textures from various environments

Our study reveals that aggregation is not a uniform process. Repeated aggregation and subsequent disaggregation leads to the formation of a variety of aggregate types and sizes during volcanic eruptions. Our data shows that PC and AP samples can occur next to each other in the same stratigraphic unit, and that single aggregate types are not necessarily

confined to certain stratigraphic units (i.e. AP2 type samples were found both in fall and PDC deposits, see Table 1). Mueller et al. (2016) have shown that the generation of PC or AP type aggregates is strongly dependent on the PSD of the host particle cloud: very restricted initial PSDs (of just a few tens of µm diameter particles) produce PC type aggregates, whereas broad initial PSDs (of several tens to few hundreds of µm-diameter particles) tend to produce structured AP type aggregates. Samples of PC type aggregates analyzed in this study (e.g. particle clusters from Wehrer Kessel volcano, Eifel, Germany, Fig. V.12a), show very narrow PSDs compared to the Stromboli AP2 type aggregates which have PSDs that range 0–500 µm (Fig. V.12b). During volcanic eruptions two sedimentation possibilities for two co-existing aggregate types (PC and AP) can be hypothesized. 1) PC1 type aggregates may in some cases represent incomplete AP2 type aggregates, which were deposited before the fine grained rim could be (fully) established; or, 2), as aggregation experiments have shown that aggregates are produced within a few seconds (e.g. Van Eaton et al. 2012, Mueller et al., 2016), areas in the plume with a more confined PSD may exist, so that during a short time window, PC1 aggregates are generated and deposited.

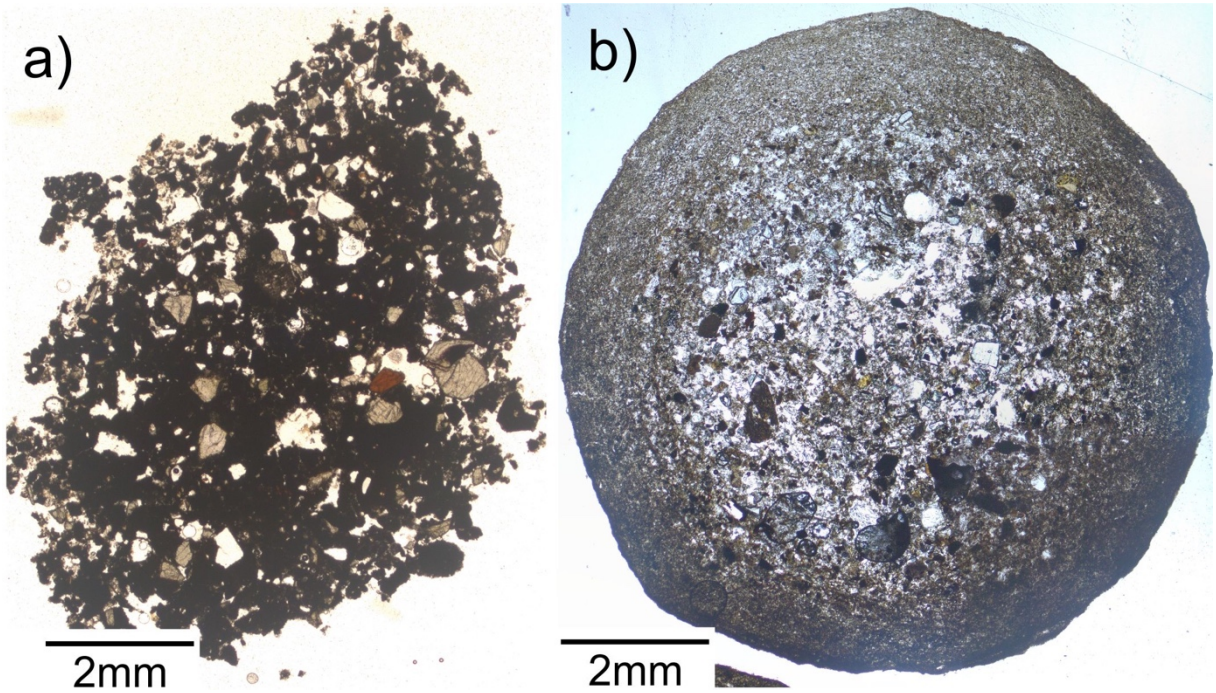

Figure V.12: a) Thin section of a structureless aggregate (PC1 type) from the Laacher See eruption, sampled at the location Wehrer Kessel Volcano. PSD is relatively confined and compared to previously described aggregates, very coarse. b) Thin section of an aggregate sampled at Stromboli (AP2 type, Secche di Lazzaro unit). A clear distinction in core and rim is possible based on PSD.

AP2 type aggregate formation is favored in environments with broad particle size distributions that promote selective particle aggregation processes. Whether or not a PC

becomes coated with one or more fine-grained rims depends on the variability in differential velocity or vector of existing aggregate and surrounding fines. Multiple rim growth (e.g. Fig. V.2e) may be favored when an aggregate is exposed to variable transport (from quasi-coupled during rise in an eruption plume to highly turbulent during fall) and ambient conditions (humidity, temperature, etc.), for example, during fallout from an ash plume and into a PDC.

The susceptibility of aggregates to erosion or destruction during transport or deposition may play a significant role in defining the stratigraphic levels in which aggregates are being found. There is a higher probability of aggregate preservation during the waning stages of PDCs (lower transport energy) and thus they may be preferentially found in the upper parts of PDC deposits. During peak intensities, aggregates that are being added from the turbulent ash cloud to more turbulent and more particle rich basal parts of PDCs, are prone to breakup or disintegrate completely (see also Brown et al. 2010, 2012). In several outcrops, the number of aggregates increases nonlinearly towards the top of individual beds (including deposits from Lago di Martigniano and Stracciacappa, Tungurahua, and Tenerife, Table 1), whereas simultaneously the number of broken aggregates and aggregate fragments is decreasing. Similar observations have been made by Brown et al. (2010) at Tenerife, where aggregate fragments were mainly found at lower, basal parts of PDCs. The preservation potential of aggregates decreases towards the basal parts of a moving PDC due to the greater particle concentrations and increased momentum and energy of the moving material which ultimately leads to break-up and destruction of aggregates. During the waning phase of a PDC pulse, chances of survival for aggregates increase since collisions with other clasts will become both less frequent and less intense. This is manifested by the frequent upward grading of aggregate frequency in individual stratigraphic layers. A similar pattern can be inferred for the Nördlinger Ries impact deposit, where aggregates are found exclusively in discrete intervals a few cm thick in the upper parts of the crater fill ejecta, and exclusively in matrix-supported zones. In the Ries FBN 73 drill core, penetrating a total length of 1140 m of sediments, aggregates were only found at a confined vertical range of 5 m within the top part of the ejecta fall back layer. Stöffler et al. (2013) proposed that the accretionary lapilli formed during fall from particles that had been ejected highest into the atmosphere, rich in solid dust and water vapor. Apart from the plume temperature, this model is largely similar to the volcanic scenario. It remains open if PC type aggregates have never been generated or if they have not survived transport and deposition. So far, they have not been described for the Ries or Sudbury impact sites.

Impact-generated aggregates tend to have much smaller core to rim ratios than volcanic aggregates. Only a few volcanic aggregates, (e.g. the double aggregate from Tenerife, Fig. V.2c) show rims with thicknesses equivalent to the respective radii of the cores. This was

only reproduced by artificial means by the use of high viscosity binders. Although aggregation in impact-generated dust clouds is analogous to aggregation in volcanic ash clouds, there clearly are differences in process that control the nature of the aggregates.

V.6 Discussion

Throughout this study, it becomes apparent that aggregates and especially accretionary pellets from volcanic, impact and artificial environments are nearly indistinguishable from each other; still, the respective environmental starting conditions may be drastically differing in their parameters:

a) An impact event only forms one single pulse, whereas a volcanic plume can be replenished by multiple explosions during one eruption.

b) The initial velocity of ejecta leaving an impact crater can be on the order of km s^{-1} (Johnson and Melosh 2012), while volcanic ash tends to have an initial velocity upon ejection from a volcano on the order of m s^{-1} (Wilson and Self 1980, Sahetapy-Engel et al. 2009, Taddeucci et al. 2012).

c) Different starting material: impact ejecta is comprised of whatever target material is hit; in case of the Ries impact event, this includes abundant carbonates with some cherts. In case of Sudbury, this included various sediments as well as the basement granites. By contrast, volcanic lapilli are formed from clasts that derive from a largely homogeneous starting composition.

d) Residence time: Because the depositional conditions of impact-generated aggregates are unknown, it is also unknown what the time of formation may have been. It is possible that impact-generated aggregates formed over periods of time that are longer than for volcanic aggregates.

Despite these clear starting differences, environmental conditions within the plume / ejecta curtain must change during later stages in order to generate such remarkably similar accretionary lapilli:

Artificial aggregation experiments have shown the preference of particles to aggregate in decelerated areas of the fluidized bed, rather than in the central, channeled and high velocity stream (e.g. Salman et al. 2006). Similarly, aggregation in volcanic plumes is described to be a process happening in the decelerated umbrella region or during fallout (e.g. Durant et al. 2009), rather than in the central gas thrust region of an eruptive column. Accordingly (and due to the high textural and structural similarity between volcanic and impact aggregates), we hypothesize aggregation during impact events to happen at later stages, e.g. during fallback

of material. This hypothesis is supported by the occurrence of Ries aggregates at the stratigraphic top of the deposit, which is interpreted as late fallback material (e.g. Graup 1981).

The influence of the different starting materials in the particle plume seems to be of subordinate importance. Volcanic field studies and experiments have shown that preservation of aggregates is critically depending on the availability of soluble salt compounds such as e.g. NaCl or $CaSO_4$ (Gilbert and Lane 1994; Mueller et al. 2017b). Volcanic eruptions offer two ways to precipitate salts on ash surfaces: 1) through precipitation of salt crystals (e.g. NaCl) out of salt rich brines (e.g. interaction of volcanic ejecta with sea water during phreatomagmatic eruptions), or, 2) though diffusion driven precipitation after the chemical interaction of acid solutions (e.g. HCl or H_2SO_4) with ash particles (e.g. Ayris et al. 2013, 2014). Whereas the latter mechanism may also apply for impact events, salts for binding aggregates here may further depend on the chemistry of the target material and hence significantly influence aggregation efficiency: carbonite rich cherts as in the Ries area may significantly boost the generation / presence of such salts like gypsum or calcium chloride on ejecta particles, which will in turn improve aggregate stability and their chance of preservation (Mueller et al. 2017b).

Volcanic aggregates are predominantly found in proximal to medial locations (up to a few 100 km from the source), whereas aggregates have been described in meteorite impact deposits distal (within 1,000s of km as for example, for Chicxulub, Yancey and Guillemette 2008), and medial (within 10s to 100 of km as, for example, at Stac Fada, Branney and Brown 2011) to the impact crater as well as within the impact crater itself (e.g. Sudbury, Grieve 2010). The data presented here shows that volcanic and impact-generated aggregates are similar structurally and texturally, with the only discernible difference being the generally thicker rims around meteorite impact aggregates. This indicates that irrespective of the physical dynamic differences involved in the generation of the different particle clouds, there were windows of opportunity when the ambient conditions were favourable for aggregation and for the preservation of accretionary lapilli. Coupled with an understanding of the underlying physical, chemical and mechanical aggregate formation processes derived from experiments, this provides an opportunity to better understand dust cloud processes during the deposition of impact ejecta.

V.7 Conclusion

Particle aggregation is a common process in particle-rich environments. Upon mechanical interaction, particles stick because of liquid binding or electrostatic forces followed by mineral precipitation. Aggregates from two impact sites and sixteen volcanoes have been compared to artificial aggregates generated under controlled and scaled lab

experiments. During the formation of the artificial aggregates, particle properties and boundary conditions were controlled to constrain aggregation efficiency variations. All three aggregation environments produce complex, internally structured aggregates; however, unstructured particle clusters were only found in the experimental and volcanic aggregate populations. If this is due to a lack of preservation during deposition or diagenesis of impact deposits is unclear. Primary particle size distributions are similar for aggregates of all three environments. Experimental and volcanic aggregates exhibit very thin concentric rims around relatively large aggregate cores, whilst meteorite impact-generated aggregates commonly show rims with thicknesses that exceed the diameter of the cores—a feature that is only very rarely observed for volcanic aggregates and not at all for artificial ones. In summary, it is remarkable that meteorite impact-generated and volcanic aggregates share many similarities, and in some cases may be indistinguishable without their stratigraphic and lithological context. To date, no major impact event has been witnessed by humans, therefore knowledge of the impact event and of particle deposition is based on interpretation of field data and on modeling. Explosive volcanic eruptions that produce aggregates have been observed and studied in greater detail and the understanding of the underlying processes for the formation of aggregates has improved significantly in the past decades through numerical, field and experimental studies (e.g. Costa et al. 2010, Van Eaton and Wilson 2013, Bagheri et al. 2016, Mueller et al, 2016). Based on the results of this study, we can infer that ambient conditions necessary for aggregation within dust clouds from meteorite impacts can be broadly similar to those within volcanic ash clouds and further can be reproduced in the laboratory.

V.8 Acknowledgements

This work is supported by the Marie Curie Initial Training Network 'VERTIGO', funded through the European Seventh Framework Program (FP7 2007-2013) under Grant Agreement number 607905. We thank Susann Siegert (Museum für Naturkunde Berlin, Germany) for providing thin sections from Ries drillcores, Corrado Cimarelli (LMU) for field work support in Italy, Armin Freundt and Steffen Eisele (GEOMAR) for providing Cape Verde and Nicaragua aggregates, Adam Stinton and Thomas Christopher (MVO) for Montserrat aggregates, Michael Jacob, Katja Oppermann, Ulrich Walter and Melanie Guttzeit for their help at Glatt Ingenieurtechnik GmbH and Mathieu Colombier and Kate Dobson (LMU) for Xray-CT analysis of our samples. The Laacher See ash used in this study was kindly offered by ROTEC GmbH & Co. KG (Mühlheim-Kärlich, Germany). D.B.D. acknowledges the support of European Research Council Advanced Grant 247076 "EVOKES" (Explosive volcanism in the Earth System). This manuscript benefitted greatly from the editorial handling by Richard Brown and the constructive reviews by Alexa Van Eaton and an anonymous reviewer.

Chapter VI

Concluding Remarks and Outlook

VI.1 Concluding Remarks

Outcomes obtained in this thesis focus on the lifecycle of volcanic ash aggregates. Volcanic ash aggregation following explosive volcanic eruptions is a mechanism which can serve to significantly alter ash plume dispersal; plume dispersal modeling, therefore, must rest on a thorough understanding of aggregation processes. Some key questions raised in the introduction were (1) which physical and chemical conditions support ash aggregation? and (2) are formed aggregates stable enough to deposit and be removed from the atmosphere, or do they break up during the settling process? In the case of the latter, the primary particles may have the potential to remain in the atmosphere. Experimental results have been interrogated in order to explain structural and textural properties of volcanic- and meteorite impact-related particle aggregates that have been sampled during a field campaign. This final chapter will recapture the most significant findings of this dissertation and frame them in relation to questions that were raised in the introduction.

VI.1.1 Experimental production of ash aggregates

In collaboration with *Glatt Ingenieurtechnik GmbH* in Weimar, Germany, it was possible to mimic natural wet aggregation processes in the lab, as they are expected to occur in dense, particle-laden environments such as volcanic eruption plumes. The *ProCell® Lab*, developed by *Glatt*, was used as a granulation device. The *ProCell® Lab* fluidizes granular material from a solid-like state to a fluid-like state and allows liquids to be sprayed through a nozzle into the fluidized bed. A lateral outlet of the system allows for the separation, drying and collection of aggregated material. Electrostatic aggregation within the *ProCell® Lab* can be excluded: grounding of fluidization devices is a crucial step taken to avoid particle charging, which can in turn lead to equipment-damaging dust explosions. The *ProCell® Lab* was used to aggregate natural phonolitic and rhyolitic ash or soda-lime glass beads (analogue material). H_2O, HCl and H_2SO_4 have been used as liquid binding agents and NaCl and $CaSO_4$ as cementing agents. The liquid and cementing agents used are chemical compounds commonly released—in one form or another—during volcanic eruptions. Aggregate sizes of several mm in diameter were re-produced, as well as both particle clusters (internally unstructured) and accretionary pellets (internally structured). Aggregation was successful both in the presence and absence of cementation agents such as NaCl. Preservation of aggregates was only successful in the presence of a solid binder with which to cement the aggregate after drying and with the abolition of liquid bonding forces. Cementing agents such as NaCl were either pre-doped on the ash and glass bead particles via spraying a water-salt solution, or precipitated through chemical reactions of the material with acid solutions (HCl, H_2SO_4). Production and preservation of aggregates with low NaCl concentrations (< 1,000 $mg.kg^{-1}$), typical for natural aggregates, was possible.

VI.1.2 Efficiency controls on ash aggregation

In order to model the influence of ash aggregation on plume dispersal as accurately as possible, it is important to know not only under which conditions particles aggregate, but also how fast and efficiently they aggregate, and the governing controls on their aggregation efficiency. Experiments have shown that in order to establish liquid bonding between fluidized particles, a minimum relative air humidity of about 10-15% is required. An exponential increase of aggregating particles per time with increasing air humidity can be observed. Although *ProCell® Lab* experiments had to stop at relative air humidities of about 50-60% or higher due to collapse of the fluidized bed, observations in nature during volcanic eruptions prove that particle aggregation also occurs at relative air humidities of up to 100 % (e.g. Tomita et al., 1985). A second major control on aggregation efficiency is the total grain size distribution: about one order of magnitude in aggregate mass production rate per time separates the fast aggregating fine ash particles (< 40 µm) from the slower aggregating coarse particles (40-90 µm). Similar trends are observed for analogue material experiments with glass beads. A third control on aggregation efficiency is exerted by the liquid binder viscosity: low viscosity binders (e.g. HCl) are more efficient at aggregating particles than high viscosity binders (e.g. H_2O). However, the true extent of the influence of binder viscosity is uncertain, as in this case low viscosity binders—such as HCl—also produced surficial salt precipitations, promoting aggregate preservation. Nevertheless, numerical models support the positive influence of binder viscosity on aggregation efficiency.

VI.1.3 A new perspective on internal structuring of accretionary pellets

Three different possibilities have so far been presented in the relevant literature to explain the internal stratification of volcanic accretionary pellets: 1) during growth, aggregates are re-entrained in plumes several times and traverse areas of different grain size populations, leading to grain size-dependent structuring; 2) unstructured particle clusters form within ash plumes or co-ignimbrite ash plumes and fall into laterally moving PDCs, which provide a turbulent and chaotic environment and fosters the aggregation of concentric rims around particle clusters; 3) after a change of binding mechanisms from hydrostatic to electrostatic, only very fine ash particles can be accreted and serve to build a fine-grained concentric rim. For the first time, this thesis suggests and experimentally demonstrates a fourth possibility for the generation of internally-structured accretionary pellets: based on a numerical model, aggregation is proposed to be a size-selective process, which is in turn responsible for internal structuring. The model divides wet aggregation into two stages: during stage one, all particles with a theoretical liquid layer around them collide successfully, such that particles stick to each other (up to a certain particle size threshold). Impact energies of the colliding particles can be dissipated by the viscous forces of the liquid layer allowing the particles to adhere to each

other. During stage two, as the aggregate core is growing, impact energies of particles large in size relative to the aggregate core create impact energies too high to be dissipated by the liquid layer and particles will rebound. Fine particles, however, generate lower impact energies and keep sticking to the aggregate core after impact. This size-selective process accretes a concentric rim of fine particles around a chaotic, unstructured core, just as is observed in natural accretionary lapilli. Timescales for experimental, mm-sized accretionary pellet production are on the order of seconds (< 10 s), which makes it a very plausible, additional alternative to previously suggested accretionary pellet generation mechanisms. The conclusion is drawn that a combined plume—PDC environment is not a necessary prerequisite for the generation of accretionary pellets, nor does the aggregate have to cycle several times through various plume regions. However, a broad enough particle size distribution (e.g. < 100 μm) is necessary to allow for size-selective growth of the aggregate.

VI.1.4 Ongoing physical and chemical processes on ash surfaces during aggregation

To date, it is only partially possible to monitor physical or chemical particle surface processes in situ during particle aggregation (e.g. via highspeed monitoring). Substantial post-experimental analysis of artificial and natural aggregates was performed—such as Scanning Electron Microscopy (SEM), optical microscopy, surface leaching, particle size distribution, surface area, and density measurements—in order to characterize samples more accurately and gain additional insights into microscopic aggregation processes. SEM analysis revealed a significant re-mobilization of surface salts during aggregation: whereas materials pre-doped with NaCl exhibited an even distribution of NaCl crystals on their surface, aggregated material showed concentrated NaCl assemblages in the form of solid salt bridges at the particle—particle contact points. A conceptual model is presented here that suggests re-mobilization of surface salts (e.g. NaCl) through dissolution of the liquid binder (e.g. H_2O). The salt-water brine is then pulled along the particle surface by capillary forces to particle-particle contact points. More voluminous salt bridges are observed between larger particles, as they provide a greater surface catchment area for soluble salts. Further, we observe the formation of substantial surface salts on cemented aggregates just by spraying diluted (2.3 %) HCl. Further, during the interaction of ash with HCl, the release of agents potentially hazardous to the environment (e.g. K, Al, Fe) is observed. The release rate of these elements is proportional to the concentration of HCl: at the highest experimental HCl concentrations (37 %), the highest salt generation was recorded. In addition, metal release from ash surfaces was observed. Concerning pre- and post-experimental particle size distribution of aggregates, an enrichment of fines (<40 μm) is observed in ash aggregates relative to the starting material; this enrichment of fines is not observed for glass bead aggregates. This difference may be

attributed to the relatively higher specific surface roughness of fine ash particles, which allows for mechanical interlocking, granting them extra stability compared to glass beads.

VI.1.5 Deposition or not? Stability controls on ash aggregates

One entire chapter of this dissertation is credited to the key question of aggregate stability. Currently, models such as *FPLUME 1.0* (Folch et al., 2016) assume that aggregated material is removed from the atmosphere. Indeed, disaggregation processes are neglected entirely due to the lack of quantitative datasets. Due to the aggregates' low binding forces, they are fragile and very prone to breakup. Impact experiments of artificial aggregates have shown failure at impact energies as low as 10^{-4}-10^{-6} J. This makes aggregates in plumes highly susceptible to disaggregation into primary particles upon collisions with larger fragments (mm-sized ash, lapilli or bombs). These disaggregated primary particles then have the potential to remain in the atmosphere and, contrary to the underlying assumptions of present numerical forecasting models, are not necessarily removed from the atmosphere and deposited on the ground. Importantly, the results presented in this thesis provide a quantitative foundation by which to implement disaggregation processes into numerical ash plume dispersal models: not only identifying the parameters which govern aggregate stability, but also assessing the relative influence exerted by the attendant operative mechanisms.

Several aggregate charges have been produced with the *ProCell® Lab* using volcanic ash materials (rough surface) and soda-lime glass bead materials (smooth surface). Different particle size distributions were imposed for either material (< 40 µm, 40-90 µm and < 90 µm for volcanic ash, < 50 µm, 40-70 µm and < 70 µm for soda-lime glass beads). Further, different NaCl binder concentrations, ranging between 1 $g.kg^{-1}$ and 20 $g.kg^{-1}$ were applied to cement aggregates. An experimental setup was designed in order to impact aggregates on a solid surface, measure the impact energy and record disaggregation processes. Three disaggregation types were observed: 1) surface chipping (< 10 wt.% of the parental aggregate broke off), 2) fragmentation (10-90 wt% material loss of parent aggregate) and 3) total disintegration (> 90 wt% material loss of parent aggregate). Stability of aggregates has been shown to be mainly controlled by particle size distribution of primary particles, salt binder concentration, and—to some extent—by primary particle morphology. Higher binder concentration allows the establishment of more voluminous solid salt bridges at particle-particle contact points, which in turn grants the aggregate greater stability. For the same reason (solid bridges with large volume), but due to a different mechanism, aggregates with large primary particle sizes exhibit greater stability relative to those with finer primary particle sizes: large particles offer a relatively higher surface area that can be scavenged by liquid droplets for soluble salt precipitations. Transported through the pull of capillary forces to particle-particle contact points, aggregates with large primary particle surfaces can deposit

relatively higher salt loads between particles. Finally, aggregates composed of volcanic ash particles showed slightly higher stability than comparable (same PSD and binder concentration) glass bead aggregates. The higher surface roughness of volcanic ash relative to the glass beads allows mechanical interlocking, which is inferred to be the main cause for increased stability of ash aggregates.

In conclusion, it is crucial to note that freshly generated aggregates, however much salt they might have as solid binder, are very fragile and prone to disaggregation. It is hence important for numerical forecast models to consider the possibility of aggregate breakup in the atmosphere, rather than assuming aggregated particles to be permanently removed from the atmosphere and not subject to further dispersal. A further detail is the paradigm of fine ash aggregation: studying the controls on ash aggregation efficiency has shown the particular preference of fine ash to aggregate – at the same time, we now note a preference of aggregates with fine primary particle sizes to disaggregate.

VI.1.6 Aggregation in the fields of volcanology, granulation industry and planetary science

Experimentally obtained results on particle aggregation are assessed in this final chapter to explain structures and textures of natural aggregates. In an extensive field campaign, volcanic aggregates were samples from more than 15 globally distributed eruption sites. Moreover, volcanic and artificial aggregates were compared with those generated during meteorite impact events, allowing inferences to be made with regards to their generation processes which have not yet been witnessed and recorded by humans. Impact aggregates were sampled from the Nördlinger Ries impact site in South Germany. Notably, impact aggregates can be found at several other impact sites on planet Earth (e.g. Chicxulub, Mexico, and Stac Fada, Scotland) and have additionally been described during lunar Apollo missions and recorded by the Opportunity Rover on Mars.

1) Textural properties

Artificial, volcanic, and impact aggregates all display a similar average range of primary particle size distribution (< 200 µm). For artificial and volcanic aggregates, it was further possible to compare PSD of the aggregates with the PSD of the parent particle mixture. Both artificial and natural accretionary pellets are enriched in fines compared to their parental mixture. This is credited to the size-selective aggregation process, which preferentially accumulates fine particles around a growing core. Fine particles exhibit lower impact energies and are hence easier to bind through hydrostatic bonding.

2) Structural properties

Volcanic aggregates are clearly divided in particle clusters (i.e. lacking an internal structure) and accretionary pellets (internally structured into a core and rim). In addition to the potential formation mechanisms responsible for internal stratification of aggregates already published, this thesis presents a new mechanism: size-selective particle aggregation. For the case of meteorite impact-related aggregates, exclusively internally-stratified accretionary pellets have been identified or described for the Ries site, as well as for any other studied terrestrial, lunar or planetary impact site. Further, whereas rims of volcanic and artificial accretionary pellets are generally spherical, those observed in impact-related aggregates are of an irregular, wavy character. Finally, the rim to core ratios, being similar within volcanic and artificial aggregates, differ significantly for impact-related aggregates that show rim radii approximately equivalent to their corresponding core radii. Volcanic accretionary pellets typically have rims with radii of a few percent of the according core radii.

3) Cementation of aggregates

Solid chemical binders cement aggregates after formation and increase their chances of preservation. Typical binders described for volcanic ash aggregates are NaCl or $CaSO_4$; both were successfully employed under laboratory conditions in order to cement artificial aggregates. Halites have further been described in impact-related aggregates, however it is not clear whether they present a primary cementation agent or a secondary mineralization process due to the age (millions to billions of years) of the aggregates. For aggregates found at the Apollo landing site on the Moon, wet formation through liquid bonding can be ruled out as—to our current knowledge—the Moon never had an atmosphere. Investigations into potential lunar binding mechanisms revealed formerly molten droplets to be responsible for particle sticking. A similar process, sintering, has been observed for volcanic ash aggregates, but again it is unclear whether this is a primary aggregation process or if it happened after deposition, e.g. through a hot, overriding PDC.

4) Size of aggregates

The size of volcanic aggregates can range from mm to cm in diameter, whereas artificial aggregates are typically in the range of mm and impact aggregates are generally larger than 1 cm in diameter. It can only be speculated, but one reason for this observed discrepancy might be the respective aggregation timescales. In volcanic environments, cm-sized aggregates (which are exclusively accretionary pellets) are found in large PDC deposits from major volcanic eruptions (e.g. Oruanui, New Zealand; Colli Albani, Italy). PDCs of large eruptions may travel 10s of km distant from the volcano, which allows the formation of large

aggregates. Following the proposed scheme of size-selective particle aggregation, aggregation should achieve a natural limit once it has reached a certain size. However, during far-ranging PDC transport, aggregates may be exposed to different aggregation environments (e.g. relative air humidity, binder viscosity, salt concentration etc.) which have the potential to re-start aggregation. This hypothesis is further supported by the fact that these large, well-travelled aggregates generally exhibit multiple rims, a result of their traversing different aggregation regimes. For the same reason, impact-related aggregates are generally cm-sized: ejecta curtains spread hundreds or more km from the impact site, giving aggregates time and the possibility to traverse several aggregation regimes during their formation. Like far-travelled, cm-sized volcanic aggregates, impact aggregates are also exclusively accretionary pellets and generally exhibit multiple rimming. It was not possible to mimic these aggregation processes in the laboratory, since experimentally-formed aggregates in the *ProCell Lab*® are generated within seconds; also, during a second re-entrainment into the fluidized bed, they disaggregate. Due to the experimental aggregates' short lifespan, it is not possible to experimentally expose them to differing aggregation regimes (e.g. by changing binder properties) and therefore mimicking multiple large sizes or multiple riming—as observed for impact aggregates or far-travelled volcanic aggregates—was not possible.

5) Stratigraphic positioning of aggregates

Impact aggregates such as, for example, those from the Ries Impact Event are found in the upper layers of their stratigraphic units, which are interpreted as late ejecta curtain fallback units. Evidence of aggregates beyond a stratigraphic depth of several m is missing. The same can be reported for volcanic aggregates deposited in PDC sediments, which are almost exclusively found in the uppermost layers. Basal PDC units usually completely lack aggregates or, rarely, contain fragments (parts of rims and cores, for example). Contrary to the general opinion of other studies, the lack of aggregates in deeper stratigraphic units is inferred in this thesis to be due to the destructive nature of PDCs, rather than relying on the assumption that aggregates are not built there at all. As outlined in a previous chapter, aggregation experiments have even shown a positive influence of a dense and particle-laden environment on aggregation efficiency, as it increases the probability of particle collisions. Moreover, experiments have shown aggregation can take place on the order of seconds. Accordingly, aggregate generation is actually anticipated to be enhanced in deep, basal parts of PDCs; however, this also goes hand-in-hand with more complete and immediate destruction of aggregates due to the highly-energetic environment.

VI.2 Outlook

The focus of this dissertation is on the lifecycle of volcanic ash aggregates. Experimental production of aggregates in fluidized beds under a controlled environment allowed for the exact characterization of parameters controlling aggregation efficiency. The primary controls on ash aggregation were found to be relative air humidity and particle size distribution as well as their surface morphology, liquid binder properties and the presence and concentration of solid cementation agents. These experimental parameters can easily be correlated to several Eruption Source Parameters (ESPs) which are a significant component of numerical ash plume forecast models:

- *Plume Height*: a larger plume height gives ash particles potentially more time to aggregate, which would in turn allow for greater aggregate sizes and potentially higher removal of ash from the atmosphere. Also, hydrometeor formation is enhanced at higher plume heights.

- *Mass fraction of fine ash*: a clear relationship between ash aggregation efficiency and particle size distribution was stated in this thesis. Further, a clear dependency of aggregate stability on fine ash content was found. Whereas the presence of fine ash enhances aggregate formation, it simultaneously supports disaggregation as the fine ash content of aggregates lowers their overall stability against collisions with other aggregates or fragments.

- *Eruption Category*: eruptions are divided into categories (large/ small, mafic/ silicic, submarine/ subaerial etc.). Several of these categories can have a clear implication on mass fraction of fine ash which is in turn a crucial (dis-) aggregation parameter. For example, silicic eruptions are generally more effective at producing large volumes of fine ash (e.g. Dartevelle et al., 2002); further, medium- to large-sized eruptions are generally shown to have a mass fraction of fine ash (< 60 µm) of 0.5 to more than 0.7 (Walker 1980, 1981). Finally, experiments have demonstrated the greater potential of silicic ash to produce soluble surface salts (Ayris et al., 2014), which is in turn a critical parameter influencing stability of aggregates and their chance of preservation, and hence their propensity for ultimate removal from the atmosphere.

- *Other parameters*: several minor, but nevertheless important, ESP parameters exist that are related to particle aggregation, including degassing (gas chemistry and mass flux rate), plume conditions (re-entrainment of ambient moisture or particles by turbulent eddies), and magmatic water mass fraction (moisture in plumes can as well be of magmatic origin).

The above-named ESPs are all clearly correlated to particle aggregation in volcanic eruption plumes. The task now remains to implement the results outlined and elaborated upon in this thesis into numerical ash plume forecast models. Ultimately, this will serve to improve aggregation probability modeling and will allow—for the first time ever—the inclusion of disaggregation processes, mechanisms which demonstrably exert a significant influence on the fine ash population balance in volcanic ash plumes.

VII References

Addison, W.D., Brumpton, G.R., Davis, D.W., Fralick, P.W., Kissin, S.A. (2010). Debrisites from the Sudbury impact event in Ontario, north of Lake Superior, and a new age constraint: are they base-surge or tsunami deposits. In: Gibson, R.L., Reimold, W.U., (eds.) Large Meteorite impacts and planetary evolution IV. GSA Special Paper 465, 245-268.

Adi, S., Adi, H., Chan, H.K., Finlay, W.H., Tong, Z., Yang, R., Yu, A. (2011). Agglomerate strength and dispersion of pharmaceutical powders. J. Aerosol Sci. 42, 285–294.

Alegret, L., Arenillas, I., Arz, J.A., Diaz, C., Grajales-Nishimura, J.M., Meléndez, A., Molina, E., Rojas, R., Soria, A.R. (2005). Cretaceous-Paleogene boundary deposits at Loma Capiro, central Cuba: Evidence for the Chicxulub impact, Geology 33, 721-724.

Alois, S., Merrison, J., Iversen, J.J., Sesterhenn, J. (2017). Contact electrification in aerosolized monodispersed silica microspheres quantified using laser based velocimetry. J. Aerosol Sci. 106, 1-10.

Anderson, R., Björnsson, S., Blanchard, D., Gathman, S., Hughes, J, Jonasson, S., Moore, C.B., Survilas H.J.,Vonnegut, B. (1965). Electricity in volcanic clouds. Science 148, 1179-1189.

Andrews, B.J., Manga, M. (2012). Experimental study of turbulence, sedimentation, and coignimbrite mass partitioning in dilute pyroclastic density currents. J. Volcanol. Geotherm. Res. 225-226, 30-44.

Antonyuk, S., Khanal, M., Tomas, J., Heinrich, S., Mörl, L. (2006). Impact breakage of spherical granules: Experimental study and DEM simulation. Chem. Eng. Process. Process Intensif. 45, 838–856.

Armienta, M.A., Martin-Del-Pozzo, A.L., Espinasa, R., Cruz, O., Ceniceros, N., Aguayo, A., Burton, M.A. (1998). Geochemistry of ash leachates during the 1994–1996 activity of Popocatepetl volcano. Appl. Geochem. 13, 841-850.

Artemieva, N.A., Wuennemann, K., Krien, F., Reimold, W.U., Stoeffler, D. (2013). Ries crater and suevite revisited – observations and modeling Part II: Modeling. Meteor. Planet. Sci. 48.4, 590-627.

Ayris, P.M., Delmelle, P. (2012). The immediate environmental effects of tephra emission. Bull. Volcanol., 74, 1905-1936.

Ayris, P.M., Lee, A., Wilson, K., Kueppers, U., Dingwell, D.B., Delmelle, P. (2013). SO2 sequestriation in large volcanic eruptions: high-temperature scavenging by tephra. Geochim. Cosmochim. Acta 110, 58-69.

Ayris, P.M., Delmelle, P., Maters, E.C., Cimarelli, C., Suzuki, Y.J., Dingwell, D.B. (2014). HCl uptake by volcanic ash in the high temperature eruption plume: mechanistic insights. Geochim. Cosmochim. Acta 144, 188-201.

Ayris, P.M., Delmelle, P., Pereira, B., Maters, E.C., Damby, D.E., Durant, A.J., Dingwell, D.B. (2015). Spatial analysis of Mount St. Helens tephra leachate compositions: implications for future sampling strategies. Bull. Volcanol. 77, 1-17.

Bagheri, G., Rossi, E., Biass, S., Bonadonna, C. (2016). Timing and nature of volcanic particle clusters based on field and numerical investigations. J. Volcanol. Geotherm. Res. 327, 520-530.

Bagnato, E., Aiuppa, A., Bertagnini, A., Bonadonna, C., Cioni, R., Pistolesi, M. Pedone, M. Hoskuldsson, A. (2013). Scavenging of sulphur, halogens and trace metals by volcanic ash: the 2010 Eyjafjallajökull eruption. Geochim. Cosmochim. Acta 103, 138-160.

Banks, M., Aulton, M.E. (1991) Fluidised-bed granulation: a chronology, Drug Dev. Ind. Pharm., 17, 1437-1463.

Bice, D.C. (1985). Quaternary volcanic stratigraphy of Mnagua, Nicaragua: correlation and source assignment for multiple overlapping Plinian deposits. Geol. Soc. Am. Bull. 96(4), 553-566.

Bika, D., Tardos, G.I., Panmai, S., Farber, L., Michaels, J. (2005). Strength and morphology of solid bridges in dry granules of pharmaceutical powders. Powder Technol. 150, 104–116.

Björnsson, S., Blanchard, D.C., Spencer, A.T. (1967). Charge generation due to contact of saline waters with Molten Lava. J. Geophys. Res. 72, 1311-1323.

Bonadonna, C., Calder, E.S., Choux, C., Jackson, P., Lejeune, A.M., Loughlin, S., Mayberry, G.C., Norton, G., Rose, W.I., Ryan, G., Sparks, R.S.J., Young, S.R. (2002). Tephra fallout from the eruption of Soufriere Hills Volcano, Montserrat, in: Druitt, T.H., and Kokelaar, B.P. (Eds.), The eruption of Soufriere Hills Volcano, Montserrat, from 1995-1999: Geol. Soc. London Mem. 21, 483-516.

Bonadonna, C., Genco, R., Gouhier, M., Pistolesi, M., Cioni, R., Alfano, F., Hoskuldsson, A., Ripepe, M. (2011). Tephra sedimentation during the 2010 Eyjafjallajökull eruption (Iceland) from deposit, radar and satellite observations. J. Geophys. Res., 116, B12202.

Bonadonna, C., Folch, A., Loughlin, S., Puempel, H. (2012). Future developments in modeling and monitoring of volcanic ash clouds: outcomes from the first IAVCEI-WMO workshop on ash dispersal forecast and civil aviation. Bull. Volcanol. 74, 1-10.

Branney M.J., Brown, R.J. (2011). Impactoclastic density current emplacement of terrestrial meteorite-impact ejecta and the formation of dust pellets and accretionary lapilli: Evidence from Stac Fada, Scotland. J. Geol. 119, 275-292.

Branney, M.J., Bonnichsen, B., Andrews, G.D.M., Ellis, B., Barry, T.L., McCurry, M. (2008). Snake River SR-type volcanism on the Yellowstone hotspot track: distinctive products of unusual high-temperature silicic super-eruptions. Bull. Volcanol., 79, 293-314.

Brazier, S., Davis, A.N., Sigurdsson, H., Sparks, R.S.J. (1982). Fall-out and deposition of volcanic ash during the 1979 explosive eruption of the Soufriere of St. Vincent. J. Volcanol. Geotherm. Res. 14, 335-359.

Brown, R.J., Branney, M.J., Maher, C., Dávila-Harris, P. (2010). Origin of accretionary lapilli within ground-hugging density currents: Evidence from pyroclastic couplets on Tenerife. Geol. S. Am. Bull. 122, 305-320.

Brown, R.J., Bonadonna, C., Durant, A.J. (2012). A review of volcanic ash aggregation. Phys. Chem. Earth 45-46, 65-78.

Burns, F.A., Bonadonna, C., Pioli, L., Cole, P.D., Stinton, A. (2017). Ash aggregation during the 11 February 2010 partial dome collapse of the Soufrière Hills Volcano, Montserrat. In review at J. Volcanol. Geotherm. Res.

Cannon, W.F., Schulz, K.J., Horton, J.W.Jr., Kring, D.A. (2010). The Sudbury impact layer in the Paleoproterozoic iron ranges of northern Michigan, USA. Geol. Soc. Am. Bull. 122, 50-75.

Casadevall, T.J. (1994). The 1989-1990 eruption of Redoubt Volcano, Alaska: impacts on aircraft operations. J. Volcanol. Geotherm. Res. 62, 301-316.

Chen, Y., Brantley, S.L. (1997). Temperature-and pH-dependence of albite dissolution rate at acid pH. Chem. Geol. 135, 275-290.

Cimarelli, C., Alatorre-Ibargüengoitia, M.A., Kueppers, U., Scheu, B., Dingwell, D.B. (2013) Experimental generation of volcanic lightening. Geology 42, 79-82.

Cole, P.D., Guest, J.E., Duncan, A.M., Pacheco, J.M. (2001). Capelinhos 1957-1958, Faial, Azores: deposits formed by an emergent surtseyan eruption. Bull. Volcanol. 63, 204-220.

Costa, A., Macedonio, G., Folch, A. (2006). A three-dimensional Eulerian model for transport and deposition of volcanic ashes. Earth Planet. Sci. Lett. 241, 634–647.

Costa, A., Folch, A., Macedonio, G. (2010). A model for wet aggregation of ash particles in volcanic plumes and clouds: 1. Theoretical formulation. J. Volcanol. Geotherm. Res. 115, B09201.

Costa, A., Suzuki, Y.J., Cerminara, M., Devenish, B.J., Esposti Ongaro, T., Herzog, M., Van Eaton, A.R., Denby, L.C., Bursik, M., de'Michieli Vitturi, M., Engwell, S., Neri, A., Barsotti, S., Folch, A., Macedonio, G., Girault, F., Carazzo, G., Tait, S., Kaminski, E., Mastin, L.G., Woodhouse, M.J., Phillips, J.C., Hogg, A.J., Degruyter, W., Bondadonna, C. (2016). Results of the eruption column model inter-comparison exercise. J. Volcanol. Geotherm. Res. 326, 2-25.

Cunningham, J.K., Beard, A.D. (2014). An unusual occurrence of mafic accretionary lapilli in deep-marine volcaniclastics on Eua, Tonga: Palaeoenvironment and Processes. J. Volcanol. Geotherm. Res. 274, 139-151.

D'Addabbo, M., Sulpizio, R., Guidi, M., Capitani, G., Mantecca, P., Zanchetta, G. (2015). Ash leachates from some recent eruptions of Mount Etna (Italy) and Popocatépetl (Mexico) volcanoes and their impact on amphibian living freshwater organisms. Biogeosci. 12, 7087-7106.

Dartevelle, S., Ernst, G.G.J., Stix, J., Bernard, A. (2002). Origin of the Mount Pinatubo climatic eruption cloud: implications for volcanic hazards and atmospheric impacts. Geology 30, 663-666.

De Hoog, J.C.M., Koetsier, G.W., Bronto, S., Sriwana, T., Van Bergen, M.J. (2001). Sulfur and chlorine degassing from primitive arc magmas: temporal changes during the 1982–1983 eruptions of Galunggung (West Java, Indonesia). J. Volcanol. Geotherm. Res. 108, 55-83.

Del Bello, E., Taddeucci, J., Scarlato, P., Giacalone, E., Cesaroni, C. (2015). Experimental investigation of the aggregation-disaggregation of colliding volcanic ash particles in turbulent, low-humidity suspensions. Geophys. Res. Lett. 42, 1068-1075.

Delmelle, P., Villiéras, F., Pelletier, M. (2005). Surface area, porosity and water adsorption properties of fine volcanic ash particles. Bull. Volcanol. 67, 160-169.

Delmelle, P., Lambert, M., Dufrêne, Y., Gerin, P., Óskarsson, N. (2007). Gas/aerosol–ash interaction in volcanic plumes: new insights from surface analyses of fine ash particles. Earth Planet. Sci. Lett. 259, 159-170.

De Rita D, Bertagnini A, Carboni G, Ciccacci S, Di Filippo M, Faccenna C, Fredi P, Funiciello R, Landi P, Sciacca P, Vannucci N, Zarlenga F (1994) Geological-petrological evolution of the Ceriti Mountains Area (Latium, central Italy). Mem Descr Carta Geol It 49:291-322.

Rita, D., Giordano, G., Rosa, C., Sheridan, M.F. (1995a). Volcanic risk at the Alban Hills volcano and numerical simulations. In: Trigila, R. (ed.), The Volcano of the Alban Hills. Tipografia SGS, Rome, 267-283.

De Rita, D., Faccenna, C., Funiciello, R., Rosa, C. (1995b). Stratigraphy. In: Trigila, R. (ed.), The Volcano of the Alban Hills. Tipografia SGS, Rome, 33-73.

De Rita D, Giordano G, Esposito A, Fabbri M, Rodani S (2002) Large volume phreatomagmatic PDC deposits from the Colli Albani Volcano Middle Pleistocene, Italy. J Volcanol Geotherm Res 118:77-98.

Dickinson, J.T., Jensen, L.C., Jahan-Latibari, A. (1984). Fracto-emission: The role of charge separation. J. Vac. Sci. Technol. A Vac. Surf. Films 2, 1112-1116.

Dingwell, D.B. (1996) Volcanic dilemma: Flow or blow? Science, 273, 1054-1055.

Dingwell, D.B., Lavallée, Y., Kueppers, U. (2012). Volcanic ash: an agent in Earth systems. Phys. Chem. Earth, Part A (45-46), 2-4.

Di Vito, M.A., Isaia, R., Orsi, G., Southon, J., di Vito, S., D'Antonio, M., Pappalardo, L., Piochi, M. (1999). Volcanism and deformation since 12,000 years at the Campi Flegrei caldera (Italy). J. Volcanol. Geotherm. Res. 91, 221-246.

Douillet G.A., Tsang-Hin-Sun E., Kueppers U., Letort J., Pacheco D.A., Goldstein F., Von Aulock F., Lavallée Y., Hanson J.B., Bustillos J., Robin C., Ramón P., Hall M., Dingwell D.B.,

(2013). Sedimentology and geomorphology of the deposits from the August 2006 pyroclastic density currents at Tungurahua volcano, Ecuador. Bull. Volcanol. 75, 765.

Durant, A.J., Rose, W.I., Sarna-Wojcicki, A.M., Carey, S., Volentik, A.C. (2009). Hydrometeor-enhanced tephra sedimentation from the 18 May 1980 Mount St. Helens (USA) volcanic cloud. J. Geophys. Res. 114, B03204.

Durant, A.J., Villarosa, G., Rose, W.I., Delmelle, P., Prata, A.J., Viramonte, J.G. (2012). Long-range volcanic ash transport and fallout during the 2008 eruption of Chaitén Volcano, Chile. Phys. Chem. Earth, Parts A/B/C, 45, 50-64.

Edmonds M, Herd RA (2005) Inland-directed base surge generated by the explosive interaction of pyroclastic flows and seawater at Soufriere Hills volcano, Montserrat. Geology *33*(4):245-248.

Ennis, B.J., Tardos, G., Pfeffer, R. (1991). A microlevel-based characterization of granulation phenomena. Powder Technol. 65, 257-272.

Fisher, R.V. (1961). Proposed classification for volcaniclastic sediments and rocks. Geol. Soc. Amer. Bull. 72, 1409-1414.

Foerstner, U. (1967). Petrographische Untersuchungen des Suevit aus den Bohrungen Deiningen und Wörnitzostheim im Ries von Nördlingen. Cont. Mineral. And Petrol. 15, 281-308.

Folch, A., Costa, A., Durant, A., Macedonio, G. (2010). A model for wet aggregation of ash particles in volcanic plumes and clouds: 2. Model application. J. Geophys. Res. 115, 1-16.

Folch, A., Costa, A., Macedonio, G. (2016). FPLUME-1.0: An integral volcanic plume model accounting for ash aggregation. Geol. Model Dev., 9, 431-450

Förster MW, Sirocko F (2016) The ELSA tephra stack: volcanic activity in the Eifel during the last 500,000 years. Glob Planet Change 142:100-107.

Fralick, P., Grotzinger, J., Edgar, L. (2012). Potential recognition of accretionary lapilli in distal impact deposits on Mars: a facies analog provided by the 1.85 Ga Sudbury impact deposit. Sediment. Geol. Mars. 102, 211-227.

French, B.M., Koeberl, C. (2010). The convincing identification of terrestrial meteorite impact structures: What works, what doesn't, and why. Earth Sci. Rev. 98, 123-170.

Frenkel, J. (1945), Viscous flow of crystalline bodies under the action of surface tension. J. Phys. 4, 385–391.

Freundt, A., Hartmann, A., Strauch, W., Kutterolf, S. (2010). Volcaniclastic stratigraphy of the Tiscapa maar crater walls (Managua, Nicaragua): implications for volcanic and seismic hazards and Holocene climate changes. Int. J. Earth Sci. 99, 1453-1470.

Gentner, W., Lippolt, H.J., Schaeffer, O.A. (1963). Argonbestimmungen an Kaliummineralien-XI Die Kalium-Argon-Alter der Gläser des Nördlinger Rieses und böhmisch-mährischen Tektite. Geochim. Cosmochim. Acta 27, 191-200.

Gilbert, J.S., Lane, S.J., Sparks, R.S.J., Koyaguchi, T. (1991). Charge measurements on particle fallout form a volcanic plume. Nature 349, 598-600.

Gilbert, J.S., Lane, S.J. (1994). The origin of accretionary lapilli. Bull. Volcanol., 56, 398-411.

Giordano, G., Porreca, M., Musacchio, P., Mattei, M. (2008). The Holocene Secche di Lazzaro phreatomagmatic succession (Stromboli, Italy): evidence of pyroclastic density current origin deduced by facies analysis and AMS flow directions. Bull. Volcanol. 70, 1221-1236.

Gislason, S.R., Hassenkam, T., Nedel, S., Bovet, N., Eiriksdottir, E.S., Alfredsson, H.A., Hem, C.P., Balogh, Z.I., Dideriksen, K., Oskarsson, N., Sigfusson, B., Larsen, G., Stipp, S.L.S. (2011). Characterization of Eyjafjallajökull volcanic ash particles and a protocol for rapid risk assessment. Proceed. Nat. Ac. Sci. 108, 7307-7312.

Graup, G. (1981). Terrestrial chondrules, glass spherules and accretionary lapilli from the suevite, Ries Crater, Germany. Earth Planet. Sci. Lett. 55, 407-418.

Grieve, R.A.F., Ames, D.A., Morgan, J.V., Artemieva, N. (2010). The evolution of Onaping formation in the Sudbury impact structure. Meteor. Planet. Sci. 45, 759-782.

Gudmundsson, M., Thordarson, T., Höskuldsson, A., Larsen, G., Björnsson, H., Prata, F., Oddsson, B., Magnüsson, E., Högnadóttir, T., Petersen, G., Hayward, C., Stevenson, J., Jónsdóttir, A. (2012). Ash generation and distribution form the April-May 2010 eruption of Eyjafjallajökull, Iceland. Nature Sci. Rep. 2, 1-12.

Hayakawa, Y. (1990). Mode of eruption and deposition of the Hachinohe phreatoplinian ash from the Towada Volcano, Japan. Geograph. Rep. Tokyo Met. Univ. 25, 167-182.

Hill, D.P., Dzurisin, D., Endo, E.T., Ellsworth, W.L., Galloway, D.L., Gerlach, T.M., Johnston, M.S., Langbein, J., McGee, K.A., Miller, C.D., Oppenheimer, D., Sorey, M.L. (2002). Response

plan for volcano hazards in the Long Valley Caldera and Mono Craters region, California. U. S. Geol. Surv. Bull. 2185, 65p.

Hinkley, T., Smith, K., Taggart, Jr.J., Brown, J., Wilson, S., Gent, C. (1987). Chemistry of ash and leachates from the May 18, 1980 eruption of Mount St. Helens, Washington. USGS, Washington DC, 73p.

Hoerz, F., Ostertag, R., Rainey, D.A. (1983). Bunte Breccia of the Ries: continuous deposits of large impact craters. Rev. Geophys. Space Phys. 21, 1667-1725.

Holm, P.M., Wilson, J.R., Christensen, B.P., Hansen, L., Hansen, S.L., Hein, K.M., Mortensen, A.K., Pedersen, R., Plesner, S., Runge, M.K. (2006). Sampling the Cape Verde mantle plume: evolution of melt compositions on Santo Antão, Cape Verde Islands. J. Petrol. 47, 145–189.

Horwell, C.J., Baxter, J. (2006) The respiratory health hazards of volcanic ash: a review for volcanic risk mitigation. Bull. Volcanol. 69, 1-24.

Hoshyaripour, G., Hort, M., Langmann, B. (2012). How does the hot core of a volcanic plume control the sulfur speciation in volcanic emission? Geochem. Geophys. Geosys. 13.7.

Hoshyaripour, G., Hort, M., Langmann, B. (2014). Ash iron mobilization in volcanic eruption plumes. Atmosph. Chem. Phys. Disc. 14, 32535-3258.

Huber, M., McDonald, I., Koeberl, C. (2014). Petrography and geochemistry of ejecta from the Sudbury impact event. Meteor. Planet. Sci. 49, 1749-1768.

Huber MS, Koeberl C (2017) Accretionary lapilli from the Sudbury impact event. Meteor Planet Sci 52(6):1257-1276.

Huertas, M.J., Arnbaud, N.O., Ancochea, E., Cantagrel, J.M., Fuster, J.M. (2002). $^{40}Ar/^{39}Ar$ stratigraphy of pyroclastic units from the Canadas volcanic edifice (Tenerife, Canary Islands) and their bearing on the structural evolution. J. Volcanol. Geotherm. Res. 115, 351-365.

Huettner, R., Schmidt-Kaler, H. (1999). Erläuterungen zur geologischen Karte des Rieses 1:50000. Geolog. Bavarica 104, 7-76.

Isaia, R., Vitale, S., Di Giuseppe, M.G., Iannuzzi, E., D'Assisi Tramparulo, F., Troiano, A. (2015). Stratigraphy, structure, and volcano-tectonic evolution of Solfatara maar-diatreme (Campi Flegrei, Italy). Geol. Soc. Am. Bull. 127, 1485-1504.

Isaia, R., Marianelli, P., Sbrana, A. (2009). Caldera unrest prior to intense volcanism in Campi Flegrei (Italy) at 4.0 ka B.P.: Implications for caldera dynamics and future eruptive scenarios. Geol. Res. Lett. 36, L21303.

Iveson, S.M., Litster, J.D., Ennis, B.J. (1998). Fundamental studies of granule consolidation part 2: quantifying the effects of particle and binder properties. Powder Technol. 99, 243-250.

Iveson, S.M., Wauters, P.A.L., Forrest, S., Litster, J.D., Meesters, G.M.H., Scarlett, B. (2001a). Growth Regime map for liquid-bound granules: further development and experimental validation. Powder Technol. 117, 83-97.

Iveson, S.M., Litster, J.D., Hapgood, K., Ennis, B.J. (2001b). Nucleation, growth and breakage phenomena in agitated wet granulation processes: a review. Powder Technol. 117, 3-39.

James, M.R. (1999). Electric charge within volcanic plumes on Earth and Io, Ph.D. thesis, Lancaster Univ., Lancaster, England.

James, M.R., Lane, S.J., Gilbert, J.S. (1998). Volcanic plume monitoring using atmospheric electric potential gradients, J. Geol. Soc. London, 155, 587-590.

James, M.R., Lane, S.J., Gilbert, J.S. (2000). Volcanic plume electrification: Experimental investigation of a fracture charging mechanism J. Geophys. Res., 105, 16,641-16,649.

James, M.R., Gilbert, J.S., Lane, S.J. (2002). Experimental investigation of volcanic particle aggregation in the absence of a liquid phase. J. Geophys. Res. 107(B9).

Jeremic, M.L. (1994). Rock Mechanics in Salt Mining. CRC Press, Student ed. Edition, 544 pp.

Johnson, B.C., Melosh, H.J. (2014). Formation of melt droplets, melt fragments, and accretionary impact lapilli during a hypervelocity impact. Icarus 228, 347-363.

Johnson, B.C., Melosh, H.J. (2012a). Formation of spherules in impact produced vapor plumes. Icarus 217, 416-430.

Johnson, B.C., Melosh, H.J. (2012b). Impact spherules as a record of an ancient heavy bombardment of Earth. Nature 485, 75-77.

Johnson, K.L., Kendall, K., Roberts, A.D. (1971). Surface Energy and the Contact of Elastic Solids. Proc. R. Soc. A Math. Phys. Eng. Sci. 324, 301–313.

Klapper, D., Kueppers, U., Castro, J.M., Pacheco, J.M.R., Dingwell, D.B. (2010). Impregnating unconsolidated pyroclastic sequences: A tool for detailed facies analysis. Geophys. Res. Abs. 12, EGU2010-11780.

Koeberl C (1992) Tektite origin by hypervelocity asteroidal or cometary impact: Target rocks, source craters, and mechanisms. Geol Soc Am Special Papers 293:133-152.

Kueppers, U., Auer, B, Cimarelli, C., Scolamacchia, T., Dingwell, D.B. (2011). Experimentally constraining the boundary conditions for volcanic ash aggregation. Geophys. Res. Abs. 13, EGU2011-11999.

Kueppers, U., Cimarelli, C., Hess, K.U., Taddeucci, J., Wadsworth, F.B., Dingwell, D.B. (2014). The thermal stability of Eyjafjallajökull ash versus turbine ingestion test sands. J. Appl. Volcanol. 3, 4.

Kueppers, U., Ayris, P.M., Bernard, B., Delmelle, P., Dobson, K.J., Douillet, D.A., Lavallée, Y., Mueller, S.B., Dingwell, D.B. (2016). Environmentally-mediated ash aggregate formation: example from Tungurahua volcano, Ecuador. Geophys. Res. Abs. 18, EGU2016-18290-1.

Lane, S.J., Gilbert, J.S. (1992). Electric potential gradient changes during explosive activity at Sakurajima volcano, Japan. Bull. Volcanol. 54, 590-594.

Lane, S.J., Gilbert, J.S., Hilton, M. (1993). The aerodynamic behaviour of volcanic aggregates, Bull. Volcanol. 55, 481-488.

Laurenzi, A., Bigazzi, G., Balestrieri, M.L., Bouska, V. (2003). $^{40}Ar/^{39}Ar$ laser probe dating of the Central European tektite-producing impact event. Meteor. Planet. Sci. 38, 887-893.

Lathem, T.L., Kumar, P., Nenes, A., Dufek, J., Sokolik, I.N., Trail, M. and Russell, A. (2011). Hygroscopic properties of volcanic ash. Geophys. Res. Lett. 38.11.

Le Roux, J.P. (2014). Fall velocity of multi-shaped clasts. J. Volcanol. Geotherm. Res. 289, 130-139.

Liu, Y., Cameron, I.T. (2001). A new wavelet-based method for the solution of the population balance equation. Chem. Eng. Sci. 56, 5283-5294.

Mader HM (1998) Conduit flow and fragmentation. In: Gilbert JS, Sparks RSJ (eds) The Physics of Explosive Volcanic Eruptions. Geol Soc London, Special Pubs 145:27-50.

Mastin, L.G., Guffanti, M., Servranckx, R., Webley, P., Barsotti, S., Dean, K., Durant, A., Ewert, J.W., Neri, A., Rose, W.I., Schneider, D., Siebert, L., Stunder, B., Swanson, G., Tupper, A., Volentik, A., Waythomas, C.F. (2009). A multidisciplinary effort to assign realistic source parameters to models of volcanic ash-cloud transport and dispersion during eruptions, J. Volcanol. Geotherm. Res. 186, 10-21.

Mastin, L.G., Van Eaton, A.R., Durant, A.J. (2016). Adjusting particle-size distributions to account for aggregation in tephra-deposit model forecasts. Atmos. Chem. Phys. 16, 9399–9420.

Maters, E.C., Delmelle, P., Bonneville, S. (2016). Atmospheric processing of volcanic glass: effects on iron solubility and redox speciation. Environ. Sci. Tech. 50, 5033-5040.

Mather, T.A., Harrison, R.G. (2006). Electrification of volcanic plumes. Surv. Geophys. 27, 387-432.

Matsusaka, S., Masuda, H. (2003). Electrostatics of particles. Adv. Powder Technol. 14, 143-166.

Matsusaka, S., Maruyama, H., Matsuyama, T., Ghadiri, M. (2010). Triboelectric charging of powders: A review. Chem. Eng. Sci. 65, 5781-5807.

McCarty, L.S., Whitesides, G.M. (2008). Electrostatic charging due to separation of ions at interfaces: contact electrification of ionic electrets. Angew. Chem. Int. Ed. 47, 2188-2207.

McGimsey, R.G., Neal, C.A., Riley, C.M. (2002). Areal distribution, thickness, mass, volume, and grain size of tephra-fall deposits from the 1992 eruptions of Crater Peak Vent, Mt. Spurr Volcano, Alaska. USGS Geol. Surv. Open File Rep. 01-370, 38pp.

McKay, D.S., Greenwood, W.R., Morrison, D.A. (1970). Morphology and related chemistry of small lunar particles from Tranquility Base. Science 167, 654.

Melnik, O., Barmin, A.A., Sparks, R.S.J. (2004). Dynamics of magma flow inside volcanic conduits with bubble overpressure buildup and gas loss through permeable magma. J. Volcanol. Geotherm. Res. 143, 53-68.

Melosh, H.J. (1989). Impact cratering: a geologic process. Oxford University Press, Oxford, 245p.

Mitarai, N., Nori, F. (2006). Wet granular materials. Adv. Phys. 5, 1-45.

Moore, J.G., Peck, D.L. (1962). Accretionary lapilli in volcanic rocks of the western continental United States. J. Geol. 70, 182-194.

Morgan, J.W., Janssens, M.-J., Hertogen, J., Gros, J., Takahashi, H. (1979). Ries impact crater, southern Germany: search for meteoritic material. Geochim. Cosmochim. Acta. 43, 803-815.

Mortimer, C.E., Mueller, U. (2007) Chemie, Georg Thieme Verlag, 9. Auflage, 800pp.

Mosebach, R. (1964). Das Noerdlinger Ries, vulkanischer Explosionskrater oder Einschlagstelle eines Großmeteoriten? Berichte der Oberhessischen Gesellschaft fuer Natur- und Heilkunde zu Gießen, Neue Folge, Naturwissenschaftliche Abteilung 33, 165-204.

Mueller, S.B., Lane, S.J., Kueppers, U. (2015). Lab-scale ash production by abrasion and collision experiments of porous volcanic samples. J. Volcanol. Geotherm. Res. 302, 163–172.

Mueller, S.B., Kueppers, U., Ayris, P.M., Jacob, M., Dingwell, D.B. (2016). Experimental volcanic ash aggregation: Internal structuring of accretionary lapilli and the role of liquid bonding. Earth Planet. Sci. Lett. 433, 232-240.

Mueller SB, Ayris PM, Wadsworth FB, Kueppers U, Casas AS, Delmelle P, Jacob M, Taddeucci J, Dingwell DB (2017a) Ash aggregation enhanced by deposition and redistribution of salt on volcanic ash surfaces in eruption plumes. Sci Rep 7:45762.

Mueller SB, Kueppers U, Ametsbichler J, Cimarelli C, Merrison J, Poret M, Wadsworth FB, Dingwell DB (2017b) Stability of volcanic ash aggregates and break-up processes. Sci Rep 7:7440.

Mullier, M.A., Seville, J.P.K., Adams, M.J. (1987). A fracture mechanics approach to the breakage of particle agglomerates. Chem. Eng. Sci. 42, 667–677.

Oelkers, E.H., Gislason, S.R. (2001). The mechanism, rates and consequences of basaltic glass dissolution: I. An experimental study of the dissolution rates of basaltic glass as a function of aqueous Al, Si and oxalic acid concentration at 25°C and pH = 3 and 11. Geochim. Cosmochim. Acta 65, 3671-3681.

Óskarsson, N. (1980). The interaction between volcanic gases and tephra: fluorine adhering to tephra of the 1970 Hekla eruption. J. Volcanol. Geotherm. Res. 8, 251-266.

Papale, P. (1999) Strain-induced magma fragmentation in explosive eruptions, Nature 397, 425-428.

Paradas-Herrero, A., Fernandez-Santin, S. (1984). Estudio vulcanologico y geoquimico del maar de la Caldera del Rey, Tenerife (Canarias). Estud. Geol. 40, 285-313.

Parra, R., Bernard, B., Narváez, D., Le Pennec, J.-L., Hasselle, N., Folch, A. (2016). Eruption Source Parameters for forecasting ash dispersion and deposition from Vulcanian eruptions at Tungurahua volcano: Insights from field data from the July 2013 eruption. J. Volcanol. Geotherm. Res. 309, 1-13.

Pinto, J.A., Warme, J.E. (2008). Alamo Event, Nevada: Crater stratigraphy and impact breccia realms. In: Evans, K.R., Horton, J.W.Jr., King, D.T.Jr., Morrow, J.R., (eds.) The sedimentary record of meteorite impacts, Geol. Soc. Am. Spec. Pap. 437, 99-137.

Pohl, J., Stöffler, D., Gall, H., Ernston, K. (1977). The Ries impact crater. In: Roddy, D.J., Pepin, R.O., Merrill, R.B. (eds.), Impact and Explosion Cratering. Pergamon Press, New York, 343-404.

Poret, M., Costa, A., Andronico, D., Scollo, S., Gouhier, M., Cristaldi, A. (2017). Integrating tephra dispersal models with field, airspace and airborne data: the case of 23rd February 2013 Etna paroxysm. J. Geophys. Res. 2016JB013910 in review.

Prata, A.J., Tupper, A. (2009). Aviation Hazards from volcanoes: the state of the science. Nat. Hazards 51, 239-244.

Randolph, A.D. (1988). Theory of particulate processes: analysis and techniques of continuous crystallization, second Ed. Academic Press, San Diego.

Reimer, T. O. (1983). Accretionary lapilli in volcanic ash falls: physical factors governing their formation. In: Coated Grains. Springer Berlin Heidelberg, 56-68.

Reyes-Dávila, G.A., Arámbula-Mendoza, R., Espinasa-Pereña, R., Pankhurst, M.J., Navarro-Ochoa, C., Savov, I., Vargas-Bracamontes, D.M., Cortés-Cortés, A., Gutiérrez-Martínez, C., Valdés-González, C., Domínguez-Reyes, T., González-Amezcua, M., Martínez-Fierros, A., Ramírez-Vázquez, C.A., Cárdenas-González, L., Castañeda-Bastida, E., Vázquez Espinoza de los Monteros, D.M., Nieto-Torres, A., Campion, R., Courtois, L., Lee, P.D. (2016). Volcán de Colima dome collapse of July, 2015 and associated pyroclastic density currents. J. Volcanol. Geotherm. Res. 320, 100–106.

Rocholl, A., Ovtcharova, M., Schaltegger, U., Wijbrans, J., Pohl, J., Harzhauser, M., Prieto, J., Ulbig, A., Boehme, M. (2011). A precise and accurate 'astronomical' age of the Ries impact crater, Germany: A cautious note on argon dating of impact material. Geophys. Res. Abs. 13, EGU2011-13322-7.

Rose, W.I. (1977). Scavenging of volcanic aerosol by ash: atmospheric and volcanologic implications. Geology 5, 621-624.

Rose, W.I., Durant, A.J. (2009). Fine ash content of explosive eruptions. J. Volcanol. Geotherm. Res. 186, 32-39.

Rosi, M. (1992). A model for the formation of vesiculated tuff by the coalescence of accretionary lapilli. Bull. Volcanol. 54, 429-434.

Ruggieri, F., Fernández-Turiel, J.L., Saavedra, J., Gimeno, D., Polanco, E., Naranjo, J.A. (2011). Environmental geochemistry of recent volcanic ashes from the Southern Andes. Environ. Chem. 8, 236-247.

Rumpf, H. (1975). Particle Technology. Chapman and Hall, London, 200pp.

Sahetapy-Engel ST, Harris A (2009) Thermal-image-derived dynamics of vertical ash plumes at Santiago volcano, Guatemala. Bull Volcanol 71/7):827-830.

Saleh, K., Guigon, P. (2006). Coating and encapsulation processes in powder technology, in: Salman, A.D., Hounslow, M.J., Seville, J.P.K. (eds). Handbook of Powder Technology – Granulation, eleventh Ed. Elsevier, Amsterdam.

Salman, A.D., Hounslow, M.J., Seville, J.P.K. (2006). Handbook of Powder Technology – Granulation, eleventh Ed. Elsevier, Amsterdam.

Sarna-Wojcicki, A.M., Shipley, S., Waitt, R.B.Jr., Dzurisin, D., Wood, S.H. (1981). Areal distribution, thickness, mass, volume, and grain size of air-fall ash from the six major eruptions of 1980. In: Lipman, P.w., Mullineaux, D.R., (Eds.), The 1980 eruptions of Mount St. Helens, Washington. U.S. Geol. Surv., Reston, VA, 577-600.

Schmidt, G., Pernicka, E. (1994). The determination of platinum group elements (PGE) in target rocks and fall-back material of the Nördlingen Ries impact crater, Germany. Geochim. Cosmochim. Acta. 22, 5083-5090.

Schmincke HU (2009) Vulkane der Eifel. 1st edn. Springer Spektrum, Berlin.

Schneider CA, Rasband WS, Eliceiri KW (2012) NIH Image to ImageJ: 25 years of image analysis. Nature meth 9(7):671-675.

Schumacher, R., Schmincke, H.-U. (1991). Internal structure and occurrence of accretionary lapilli - a case study at Laacher See Volcano. Bull. Volcanol. 53, 612–634.

Schumacher, R., Schmincke, H.-U. (1995). Models for the origin of accretionary lapilli. Bull. Volcanol. 56, 626-639.

Schwarz, W.H., Lippolt, H.J. (2002). Coeval argon-40/argon-39 ages of moldavites from the Bohemian and Lusatian strewn fields. Meteor. Planet. Sci. 37, 1757-1763.

Scolamacchia, T., Dingwell., D.B. (2014). Sulfur as a binding agent of aggregates in explosive eruptions. Bull. Volcanol. 76, 871-883.

Scollo, S., Prestifilippo, M., Spata, G., D'Agostino, M., Coltelli, M. (2009). Monitoring and forecasting Etna volcanic plumes. Nat. Hazards Earth Syst. 9, 1573-1585.

Self, S., Sparks, R.S.J. (1978). Characteristics of widespread pyroclastic deposits formed by the interaction of silicic magma and water. Bull. Volcanol. 41-3, 196-213.

Self S (1983) Large-scale phreatomagmatic silicic volcanism – a case-study from New Zealand. J. Volcanol. Geotherm Res 17:433-469.

Serri, G., Innocenti, F., Manetti, P., Ferrara, G. (1991). Il magmatismo neogenico-quaternario dell'area Tosco-laziale-Umbra: implicazioni sui modelli di evoluzione geodinamica dell'Appennino settentrionale. Stud. Geol. Camerti, Vol Spec. 1991/1.

Sheridan, M.F., and Wohletz, K.H. (1983) Origin of accretionary lapilli from the Pompeii and Avellino deposits of Vesuvius, in: Ron Gooley, ed., Microbeam Analysis, 1983, San Francisco Press, Inc.

Shinohara, H. (1994). Exsolution of immiscible vapor and liquid phases from a crystallizing silicate melt: implications for chlorine and metal transport. Geochim. Cosmochim. Acta 58, 5215-5221.

Sisson, T.W. (1995). Blast ashfall deposit of May, 18, 1980 at Mount St. Helens, Washington. J. Volcanol. Geotherm. Res. 66, 203-216.

Smith, D.B., Zielinski, R.A., Rose, W.I., Huebert, B.J. (1982). Water soluble material on aerosols collected within volcanic eruption clouds. J. Geophys. Res. 87, 4963–4972.

Smith, D.B., Zielinski, R.A., Taylor, H.E., Sawyer, M.B. (1982). Leaching characteristics of ash from the May 18, 1980, eruption of Mount St. Helens volcano, Washington. Bull. Volcanol. 46, 103-124.

Smith, P.G., Nienow, A.W. (1983) Particle growth mechanisms in fluidised bed granulation – I. the effect of process variables, Chem. Eng. Sci., 38, pp. 1223-1231.

Smith, V.C., Isaia, R., Pearce, N.J.G. (2011). Tephro-stratigraphy and glass compositions of post-15 kyr Campi Flegrei eruptions: Implications for eruption history and chronostratigraphic markers. Quaternary Sci. Rev. 30, 3638-3660.

Song, W., Lavallée, Y., Hess, K.U., Kueppers, U., Cimarelli, C., Dingwell, D.B. (2016). Volcanic ash melting under conditions relevant to ash turbine interactions. Nature Communications 7.

Sorem, R.K. (1982). Volcanic ash clusters: Tephra rafts and scavengers. J. Volcanol. Geotherm. Res. 13, 63-71.

Sottili, G., Palladino, D.M., Marra, F., Jicha, B., Karner, D.B., Renne, P. (2010). Geochronology of the most recent activity in the Sabatini Volcanic District, Roman Province, central Italy. J. Volcanol. Geotherm. Res. 196, 20-30.

Sparks, R.S.J. (1978) The dynamics of bubble deformation and growth in magmas: A review and analysis, J. Volcanol. Geophys. Res 3, 1-37.

Stinton, A.J., Cole, P.D., Stewart, R.C., Odbert, H.M., Smith, P. (2014). The 11 February 2010 partial dome collapse at Soufriere Hills Volcano, Montserrat. Geol. Soc. Lond. Mem. 39, 133-152.

Stoeffler, D., Artemieva, N.A., Wuennemann, K., Reimold, W.U., Jacob, J., Hansen, B.K., Summerson, I.A.T. (2013). Ries crater and suevite revisited-observations and modeling Part I: observations. Meteor. Planet. Scie. 48, 515-589.

Stoeffler, D., Artemieva, N.A., Pierazzo, E. (2002). Modeling the Ries-Steinheim impact event and the formation of the moldavite strewn field. Meteor. Planet. Sci. 37, 1893-1907.

Suzuki, Y.J., Koyaguchi, T., Ogawa, M., Hachisu, I. (2005). A numerical study of turbulent mixing in eruption clouds using a three-dimensional fluid dynamics model. J. Geophys. Res: Solid Earth 110, B8.

Taddeucci, J., Scarlato, P., Montanaro, C., Cimarelli, C., Del Bello, E., Freda, C., Andronico, D., Gudmudsson, M.T., Dingwell, D.B. (2011). Aggregation-dominated ash settling from the Eyjafjallajökull volcanic cloud illuminated by field and laboratory high-speed imaging. Geology 39, 891-894.

Taddeucci J, Scarlato P, Capponi A, Del Bello E, Cimarelli C, Palladino PM, Kueppers U (2012) High-speed imaging of Strombolian explosions: the ejection velocity of pyroclasts. Geophys Res Lett 39:L02301.

Taylor, P.S., Stoiber, R.E. (1973). Soluble material on ash from active Central American volcanoes. Geol. Soc. Am. Bull. 84, 805-835.

Telling, J., Dufek, J. (2012). An experimental evaluation of ash aggregation in explosive volcanic eruptions. J. Volcanol. Geotherm. Res. 209, 1-8.

Telling, J., Dufek, J., Shaikh, A., (2013). Ash aggregation in explosive volcanic eruptions, Geophys. Res. Let., 40, 2355-2360.

Textor, C., Graf, H.F., Herzog, M., Oberhuber, J.M. (2003). Injection of gases into the stratosphere by explosive volcanic eruptions. J. Geophys. Res.: Atmosph. 108, D19.

Textor, C., Graf, H.F., Herzog, M., Oberhuber, J.M., Rose, W.I., Ernst, G.G.J. (2006a). Volcanic particle aggregation in explosive eruption columns. Part I: parameterization of the microphysics of hydrometeors and ash. J. Volcanol. Geotherm. Res. 150, 359-377.

Textor, C., Graf, H.F., Herzog, M., Oberhuber, J.M., Rose, W.I., Ernst, G.G.J. (2006b). volcanic particle aggregation in explosive eruption columns. Part II: numerical experiments. J. Volcanol. Geotherm. Res. 150, 378-394.

Thornton, C., Liu, L. (2004). How do agglomerates break? Powder Technol. 143–144, 110–116.

Tomita, K., Kanai, T., Kobayashi, T., Oba, N. (1985). Accretionary lapilli formed by the eruption of Sakurajima Volcano. J. Jpn. Ass. Min. Pet. Econom. Geol. 80, 49-54.

Tournigand, P.Y., Taddeucci, J., Scarlato, P., Gaudin, D., Del Bello, E. (2015). Field-based study of volcanic ash via visible and thermal high-speed imaging of explosive eruptions. Geophys. Res. Abs., 17, EGU2015-12553.

Trusdell, F.A., Moore, R.B., Sako, M., Randall, A.W., Koyanagi, S.K., Chong, R., Camacho, J.T. (2005). The 2003 eruption of Anatahan Volcano, Commonwealth of the Northern Mariana Islands: Chronology, volcanology, and deformation. J. Volcanol. Geotherm. Res. 146, 184-207.

Turton, R., Tardos, G.I., Ennis, B.J. (1999). Fluidized Bed Coating and Granulation, Fluidization, Solids Handling and Processing, Chapter 7, Noyes Publications, Westwood, NJ, 331-334.

Uhlemann, H., Mörl, L. (2000). Wirbelschichtsprühgranulation, Springer-Verlag, Berlin, ISBN 3-540-66985-X.

Van Eaton, A.R., Muirhead, J.D., Wilson, C.J.N., Cimarelli, C. (2012). Growth of volcanic ash aggregates in the presence of liquid water and ice: an experimental approach. Bull. Volcanol., 74, 1963-1984.

Van Eaton, A.R., Wilson, C.J.N. (2013). The nature, origins and distribution of ash aggregates in a large-scale wet eruption deposit: Oruanui, New Zealand. J. Volcanol. Geotherm. Res. 250, 129-154.

Van Eaton, A. R., Mastin, L. G., Herzog, M., Schwaiger, H. F., Schneider, D. J., Wallace, K. L, Clarke, A. B. (2015). Hail formation triggers rapid ash aggregation in volcanic plumes. Nat. Commun. 6, 7860.

Veitch, G., Woods, A.W. (2001). Particle aggregation in volcanic eruption columns. J. Geophys. Res. 106, B11, 26,425-26,441.

Von Engelhardt, W., Graup, G. (1984). Suevite of the Ries crater, Germany: source rocks and implications for cratering mechanics. Geol. Rundsch. 73, 447-481.

Waitt R.B., Dzurisin D. (1981). Proximal air-fall deposits from the May 18 eruption- stratigraphy and field sedimentology. In: Lipman P (ed) The 1980 eruptions of Mount St. Helens, Washington. USGS, Washington DC, USA, 601-616.

Walker, G.P.L. (1980). The Taupo pumice: product of the most powerful known (ultraplinian) eruption? J. Volcanol. Geotherm. Res. 8, 69-94.

Walker, G.P.L. (1981). Plinian eruptions and their deposits. Bull. Volcanol. 44, 223-240.

Walker, G.P.L., Hayashi, J.N., Self, S. (1995). Travel of pyroclastic flows as transient waves: implications for the energy line concept and particle-concentration assessment. J. Volcanol. Geophys. Res. 66, 265-282.

Wallace, K.L., Schaefer, J.R., Coombs, M.L. (2013). Character, mass, distribution, and origin of tephra-fall deposits from the 2009 eruption of Redoubt Volcano, Alaska – Highlighting the significance of particle aggregation. J. Volcanol. Geotherm. Res. 259, 145-169.

Wardman, J.B., Wilson, T.M. and Bodger, P.S. (2013). Volcanic Ash Contamination: Limitations of the Standard ESDD Method for Classifying Pollution Severity. IEEE Transactions on Dielectrics and Electrical Insulation 20(2): 414-420.

Watanabe, K., Ono, K., Sakaguchi, K., Takada, A., Hoshizumi, H. (1999). Co-ignimbrite ash-fall deposits of the 1991 eruptions of Fugen-dake, Unzen Volcano, Japan, J. Volcanol. Geotherm. Res. 89, 95-112.

Watano, S., Fukushima, T., Miyanami, K. (1996). Heat transfer and granule growth rate in fluidized bed granulation. Chem. Pharm. Bull. 40, 269-271.

Watt, S.F.L., Pyle, D.M., Mather, T.A., Martin, R.S., Matthews, N.E. (2009). Fallout and distribution of volcanic ash over Argentina following the May 2008 explosive eruption of Chaiten, Chile. J. Geophys. Res. Solid Earth 114, 1–11.

Wilson L, Self S (1980) Volcanic eruption clouds: density, temperature, and particle content estimates from cloud motion. J Volcanol Geotherm Res 85:2567-2572.

Wilson, T., Stewart, C., Cole, J., Johnston, D. Cronin, S. (2010). Vulnerability of agricultural water supplies to volcanic ash fall. Environmental Earth Science 61(4), 675-688.

Wilson, T., Cole, J., Cronin, S., Stewart, C. Johnston, D. (2011). Impacts on agriculture following the 1991 eruption of Vulcan Hudson, Patagonia: lessons for recovery. Nat. Hazards 57(2), 185-212.

Wilson, T.M., Stewart, C., Sword-Daniels, V., Leonard, G.S., Johnston, D.M., Cole, J.W., Wardman, J., Wilson, G. and Barnard, S.T. (2012). Volcanic ash impacts on critical infrastructure. Phys. Chem. Earth, Parts A/B/C 45-46, 5-23.

Witham, C.S., Oppenheimer, C., Horwell, C.J., (2004). Volcanic ash leachates: a review and recommendations for sampling methods. J. Volcanol. Geotherm. Res. 141.3, 299-326.

Wolff-Boenisch, D., Gislason, S.R., Oelkers, E.H., Putnis, C.V. (2004). The dissolution rates of natural glasses as a function of their composition at pH 4 and 10.6, and temperatures from 25 to 74°C. Geochim. Cosmochim. Acta 68, 4843-4858.

Wörner, G., Schmincke, H.-U., 1984. Mineralogical and chemical zonation of the Laacher See Tephra Sequence (East Eifel, W. Germany). J. Petrol. 25, 805-835.

Wuennemann, K., Morgan, J.V., Joedicke, H. (2005). Is Ries crater typical for its size. An analysis based on old and new geophysical data and numerical modeling. In: Kenkmann, T., Hoerz, F., Deutsch, A., (eds.). Large meteorite impacts III. G. Soc. Am. Spec. Pap. 384, 67-83.

Yancey, T.E., Guillemette, R.N. (2008). Carbonate accretionary lapilli in distal deposits of the Chicxulub impact event. Geol. Soc. Am. Bull. 120, 1105-1118.

Zheng, K., Du, C., Li, J., Qiu, B., Fu, L., Dong, J., (2015). Numerical simulation of the impact-breakage behavior of non-spherical agglomerates. Powder Technol. 286, 582–591.

Eidesstattliche Versicherung

Ich versichere hiermit an Eides statt, dass die Dissertation von mir selbstständig und ohne Beihilfe angefertigt worden ist.

Honolulu, 26.03.2018
(Ort, Datum)

Sebastian Mueller
(Unterschrift des Doktoranden / der Doktorandin)

Erklärung

Hiermit erkläre ich, dass die Dissertation, ganz oder in Teilen, noch keiner anderen Promotionskommission vorgelegt worden ist.

Honolulu, 26.03.2018
(Ort, Datum)

Sebastian Mueller
(Unterschrift des Doktoranden / der Doktorandin)

Erklärung

Hiermit erkläre ich, dass ich mich anderweitig einer Doktorprüfung ohne Erfolg **nicht** unterzogen habe.

Honolulu, 26.03.2018
(Ort, Datum)

Sebastian Mueller
(Unterschrift des Doktoranden / der Doktorandin)